NTNU
Norwegian University of
Science and Technology

Investigation of CFD Simulations of Flow in the Upper Airways

Elin Aasgrav

MASTER THESIS

for

Student Elin Aasgrav

Spring 2017

Investigation of CFD simulations of flow in the upper airways
Undersøkelse av CFD simuleringer av strømning i de øvre luftveiene

Background and objective

Snoring is caused by the soft parts of the upper airways collapsing and preventing the air from flowing freely. In some cases snoring is so severe that medical attention is required. The most severe, obstructive sleep apnea syndrome (OSAS), affects 2-4 % of the population. A variety of treatment options exists, but today there are no available methods for predicting the outcome of the treatment. This project will be part of a larger project: *Modeling of obstructive sleep apnea by fluid-structure interaction in the upper airways*, which is a collaboration project between NTNU, SINTEF and St.Olavs Hospital and funded by the Research Council of Norway. The primary objective is to demonstrate the potential of a new patient-specific clinical tool based on mathematical models in predicting the response to OSAS treatment.

The objectives of the master project are: First, to perform CFD simulations of flow in patient-specific models of the upper airways. Second, to compare the CFD results with available experimental data. Third, to investigate the influence of the airways geometry and of inlet, outlet and wall boundary conditions and to check the grid sensitivity of the CFD results.

The following tasks are to be considered:

1 Perform CFD simulations of flow in patient-specific models of the upper airways before and after nasal surgery.
2 Compare the CFD results with available experimental data.
3 Sensitivity study:
  a) Airways geometry.
  b) Inlet and outlet boundary conditions.
  c) Wall boundary conditions.
  d) Grid.

-- ” --

Within 14 days of receiving the written text on the master thesis, the candidate shall submit a research plan for his project to the department.

When the thesis is evaluated, emphasis is put on processing of the results, and that they are presented in tabular and/or graphic form in a clear manner, and that they are analyzed carefully.

The thesis should be formulated as a research report with summary both in English and Norwegian, conclusion, literature references, table of contents etc. During the preparation of the text, the candidate should make an effort to produce a well-structured and easily readable report. In order to ease the evaluation of the thesis, it is important that the cross-references are correct. In the making of the report, strong emphasis should be placed on both a thorough discussion of the results and an orderly presentation.

The candidate is requested to initiate and keep close contact with his/her academic supervisor(s) throughout the working period. The candidate must follow the rules and regulations of NTNU as well as passive directions given by the Department of Energy and Process Engineering.

Risk assessment of the candidate's work shall be carried out according to the department's procedures. The risk assessment must be documented and included as part of the final report. Events related to the candidate's work adversely affecting the health, safety or security, must be documented and included as part of the final report. If the documentation on risk assessment represents a large number of pages, the full version is to be submitted electronically to the supervisor and an excerpt is included in the report.

Pursuant to "Regulations concerning the supplementary provisions to the technology study program/Master of Science" at NTNU §20, the Department reserves the permission to utilize all the results and data for teaching and research purposes as well as in future publications.

The final report is to be submitted digitally in DAIM. An executive summary of the thesis including title, student's name, supervisor's name, year, department name, and NTNU's logo and name, shall be submitted to the department as a separate pdf file. Based on an agreement with the supervisor, the final report and other material and documents may be given to the supervisor in digital format.

☐ Work to be done in lab (Water power lab, Fluids engineering lab, Thermal engineering lab)
☐ Field work

Department of Energy and Process Engineering, 15. January 2017

_____
Bernhard Müller
Academic Supervisor

Are J. Simonsen
Research Advisor

Sverre G. Johnsen
Research Advisor

Summary

This Master's thesis extends previous work conducted in the collaboration project called *Modelling of obstructive sleep apnea by fluid-structure interaction in the upper airways*. The main objective of the current work was to investigate the importance of including turbulence in CFD models of the human upper airways, and how model parameters (e.g. boundary conditions and grid size) affected simulation results. Computational Fluid Dynamics (CFD) was employed to do investigations of an obstructive sleep-apnea syndrome (OSAS) patient who underwent nasal surgery. The realizable k-ε turbulence model was utilized in the investigations. A set of boundary conditions is chosen as the base case for pre- and post-operative CFD simulations: at the inlet, i.e. both nostrils, a gauge pressure of 0 Pa, a turbulent intensity of 5% and a turbulent viscosity ratio of 10 is set, while a uniform velocity corresponding to a volumetric flow rate of 250 ml/s is prescribed at the outlet.

Simulations were performed on both the pre- and post-operative models of the airway geometries. The post-operative results showed an accelerated flow in the front part of the nasal cavity compared to the pre-operative results. As expected, the higher velocity led to a higher pressure drop, inherently meaning a higher resistance in the flow. These results are contradictory to the rhinomanometry data used for validation, since the rhinomanometry data show a lower pressure drop after surgery. To understand what is causing this discrepancy, a sensitivity study of the pre-operative geometry was performed.

A narrower, pre-operative airway geometry model, i.e. reduced cross-sectional areas, was made to assess the effect of uncertainty in the interpretation of the CT images used to make the 3D-geometries. The smaller cross-sections resulted in higher values for the pressure drop, turbulence kinetic energy and velocity modulus. Although the pressure drop in the narrower geometry was about twice the value found in the base-case geometry, it was still lower than what was expected from the rhinomanometry data.

The effect of outlet boundary condition type was investigated by changing it from a uniform velocity to a gauge pressure of -36 Pa, a value which was determined by the pre-operative base-case calculations. The results were unaffected by the change, indicating that it is insignificant whether the outlet condition is a uniform pressure or a uniform velocity condition. The effect of type of inlet boundary condition was assessed by changing it to a velocity inlet instead of a gauge pressure. Again, the results were identical, leading to the conclusion that it is insignificant whether the inlet condition is a pressure or a velocity boundary condition.

The wall boundary condition was examined by adding a roughness height of 0.2 mm along the wall. The pressure drop in the flow was only minorly impacted, as was expected due to the low Reynolds numbers in the flow. The preliminary conclusion was that wall roughness cannot explain the observed discrepancy between CFD models and measurements.

The grid sensitivity was studied by comparing pre-operative results from three different meshes; the base-case mesh with 1.4 million cells and two finer meshes with 6.8 million cells and 10.1 million cells. The results were virtually the same for the coarsest and the finest mesh, while the results from the 6.8M grid deviated a little from the other two, which is believed to stem from poor grid quality in the 6.8M mesh. From this it is concluded that the coarsest mesh consisting of 1.4M cells is sufficiently fine.

Sammendrag

Denne masteroppgaven viderefører tidligere arbeid gjort i samarbeidsprosjektet *Modelling of obstructive sleep apnea by fluid-structure interaction in the upper airways*, eller *Modellering av obstruktiv søvnapné gjennom fluid-struktur-interaksjon i de øvre luftveiene*. Hovedmålet i denne oppgaven var å undersøke viktigheten av å inkludere turbulens i CFD-modellene av de øvre luftveiene i mennesket, og hvordan modellparametre (f.eks. grensebetingelser og gridstørrelse) påvirket simuleringsresultatene. Numerisk fluiddynamikk (CFD) ble benyttet for å utføre strømningsundersøkelser på en pasient med obstruktiv søvnapné som gjennomgikk en neseoperasjon. Basert på tidligere funn ble turbulensmodellen realizable k-ε benyttet i undersøkelsene. Et sett av grensebetingelser ble valgt som basis: ved innløpet, i.e. begge neseborene, ble et overtrykk på 0 Pa, turbulent intensitet på 5% og turbulent viskositetsratio på 10 valgt, mens ved utløpet ble en uniform hastighet tilsvarende en volumstrøm på 250 ml/s valgt.

Simuleringer ble gjort på både de pre- og post-operative modellene av luftveiene. De post-operative resultatene viste en akselerert strømning i front av nesekaviteten sammenlignet med de pre-operative resultatene. Som forventet resulterte høyere hastighet i et høyere trykktap, noe som i praksis betyr høyere motstand i strømningen. Disse resultatene er motstridende til målinger gjort med rhinomanometri før og etter operasjonen, ettersom disse viser et lavere trykktap etter operasjon. For å forstå årsaken til dette ble det gjennomført en sensitivitetsstudie av den pre-operative geometrien.

En trangere, pre-operativ luftveisgeometri-modell, i.e. reduserte tverrsnittsarealer, ble lagd for å ta høyde for usikkerheter i tolkningen av CT-bildene som ble brukt til å lage 3D-geometriene. De trangere tverrsnittene ga høyere verdier for trykktap, turbulent kinetisk energi og hastighetmodulene. Trykktapet i den smalere geometrien ble omtrent doblet sammenlignet med basissituasjonen, men var fremdeles mindre enn hva som var forventet ut ifra rhinomanometri-dataene.

Effekten av type utløpsgrensebetingelse ble undersøkt ved å endre den fra en uniform hastighet til et undertrykk på 36 Pa, en verdi som ble bestemt av de pre-operative basisresultatene. Endringen ga ingen forskjeller i resultatene og det konkluderes derfor at det er ubetydelig om det er trykk eller hastighet som er utløpsgrensebetingelsen. Innløpsgrensebetingelsen ble også undersøkt ved å endre den fra uniformt trykk til hastighet. Resultatene var identiske, hvilket gir

konklusjonen at det er ubetydelig om det er trykk eller hastighet som er innløpsgrensebetingelse.

Vegg-grensebetingelsen ble undersøkt ved å implementere en ruhetshøyde på 0,2 mm langs veggen. Trykkfallet i strømningen ble kun minimalt påvirket, noe som var forventet på grunn av de lave Reynoldstallene i strømningen. Den foreløpige konklusjonen er at veggruhet ikke kan forklare den observerte forskjellen mellom CFD-modeller og målte data.

Sensitiviteten til cellestørrelse i gridet ble studert ved å sammenligne resultatene fra tre ulike grid; et basisgrid med 1,4 millioner celler og to finere grid med henholdsvis 6,8 millioner celler og 10,1 millioner celler. Resultatene var praktisk talt like for det groveste og fineste gridet, mens resultatet fra det mellomste gridet avvek litt fra de to andre, noe som mistenkes å være på grunn av dårlig gridkvalitet. Basert på dette antas det at det groveste gridet med 1,4 millioner celler er fint nok.

Preface

This thesis is a part of a larger collaboration project between NTNU, SINTEF and St. Olavs Hospital, funded by the Research Council of Norway. The project is called *Modelling of obstructive sleep apnea by fluid-structure interaction in the upper airways*. The objective of the project is to "demonstrate the potential of a new patient-specific clinical tool based on mathematical models in predicting the response to OSAS treatment" [25]. The collaboration project is subdivided into four work packages (WP). WP1 is Clinical Research, WP2 is Soft Tissue Modelling, WP3 is Mathematical Modelling of Fluid-Structure Interaction and WP4 is Computation Fluid Dynamics (CFD) Modelling for Prediction of Success of OSAS Surgery. This Master's thesis is a part of WP4.

There exist several treatment options for patients with OSAS, including surgery, but there is currently no way to know if this surgery will be successful. In some incidents, the result after surgery has actually been worse than before surgery. There is a demand for better diagnoses and more targeted treatment with better predictions for the outcome, to improve the chances of a positive result from the treatment. By using computational fluid dynamics to study the flow patterns in the upper airways, we are able to understand the flow mechanisms in the airway better. The hope is that this computational tool can assist medical personnel in deciding which treatment should be implemented and give better predictions, with the ultimate goal of a better outcome for the patient.

This thesis consists of results from CFD simulations of flow in patient-specific models of the upper airways before and after surgery. The CFD results for the pre-operative geometry are then compared with available experimental data. Lastly, an investigation of the influence of the airways geometry and of inlet, outlet and wall boundary conditions, as well as the grid sensitivity of the CFD results is performed.

Table of contents

List of figures

List of tables

Nomenclature

The following list of symbols explains the denotations used in this report. The indexes i, j and k refer to components of vector quantities. Dimensions are also listed below.

A area $[\text{m}^2]$

A_0 empirical constant in the realizable k-ε turbulence model

$C_\mu, C_{\varepsilon 1}, C_{\varepsilon 2}$ empirical constants in the k-ε turbulence model, C_μ can be a variable

C_1 variable in the realizable k-ε turbulence model

D_h hydraulic diameter $[\text{m}]$

δ_{ij} Kronecker delta, non-dimensional

ε dissipation rate $[\text{J/kgs} = \text{m}^2/\text{s}^3]$

η time scale ratio of the turbulence, used in the realizable k-ε turbulence model

k turbulent kinetic energy $[\text{m}^2/\text{s}^2]$

μ dynamic viscosity $[\text{kg/ms}]$

μ_t turbulent viscosity $[\text{kg/ms}]$

Ma Mach number, non-dimensional

v kinematic viscosity $[\text{m}^2/\text{s}]$

v_t kinematic eddy viscosity $[\text{m}^2/\text{s}]$

O perimeter, from Norwegian "omkrets" $[\text{m}]$

ρ density $[\text{kg/m}^3]$

ρ_w density at the wall $[\text{kg/m}^3]$

p pressure $[\text{Pa}]$

P mean pressure $[\text{Pa}]$

p' pressure fluctuation $[\text{Pa}]$

Δp pressure drop $[\text{Pa}]$

q volumetric flow rate $[\text{m}^3/\text{s}]$

R resistance, $\Delta p/q$ $[\text{kg/(m}^4\text{s})]$

Re Reynolds number, non-dimensional

S_{ij} mean strain rate tensor $[1/\text{s}]$

σ_k turbulent kinetic energy Prandtl number, non-dimensional

σ_ε turbulent dissipation rate Prandtl number, non-dimensional

τ_w wall shear stress $[\text{kg/ms}^2]$

τ_{ij} Reynolds stress components $[\text{kg/ms}^2]$

TI turbulent intensity, non-dimensional

u velocity $[\text{m/s}]$

U mean velocity [m/s]

u' velocity fluctuation [m/s]

u_* friction velocity [m/s]

$\boldsymbol{U}$ velocity vector [m/s]

VR eddy viscosity ratio, non-dimensional

Ω_{ij} mean rate of rotation tensor [1/s]

Abbreviations

Abbreviations are being used throughout this report. They are all explained in the report, but below is a summary of all the abbreviations used.

AHI	Apnea-Hypopnea Index
CFD	Computational Fluid Dynamics
CPAP	Continuous Positive Airway Pressure
CPU	Central Processing Unit
CT	Computed Tomography
DNS	Direct Numerical Simulation
LES	Large Eddy Simulation
LRN	Low-Reynolds Number
MR(I)	Magnetic Resonance (Imaging)
OSAS	Obstructive Sleep Apnea Syndrome
PAP	Positive Airway Pressure
RANS	Reynolds-Averaged Navier-Stokes
RNG	Renormalization Group
SA	Spalart-Allmaras
SGS	Subgrid-scale
SST	Shear Stress Transport
TKE	Turbulence Kinetic Energy
UPPP	Uvulopalatopharyngoplasty

1 Introduction

This Master's thesis is a part of a larger collaboration project between NTNU, SINTEF and St. Olavs Hospital, called "Modelling of obstructive sleep apnea by fluid-structure interaction in the upper airways" [25]. The overall aim of the collaboration project is to establish CFD as a useful clinical tool in assessment and alleviation of OSAS. The airway geometry that is used has been extracted from a patient's CT scans, in the project work by Maria R. Jordal [11]. The geometry retrieval was planned to be from both CT and MRI scans, but the CT images had better quality, and hence became the sole foundation for the airway geometry models.

The main objective of the work is to investigate the importance of including turbulence in CFD models of the human upper airways, and how model parameters (e.g. boundary conditions and grid size) affect simulation results. The choice of turbulence model was investigated in the specialization project by Aasgrav [1] and by Aasgrav et al. [2] (see Appendix A), while this thesis reports from the sensitivity of the realizable k-ε model to selected model parameters. The tasks of this Master thesis are to perform CFD simulations of flow in patient-specific models of the upper airways before and after surgery and compare the results with available experimental data. The influence of the airways geometry, inlet, outlet and wall boundary conditions, and grid size is investigated in order to determine the effect these model parameters have on the final result, and to possibly explain some of the observed discrepancies between the numerical and experimental results.

In a previous study by Maria R. Jordal [12], laminar flow simulations were carried out. The main purpose of those simulations was to compare pre- and post-operative results to determine if the flow pattern after surgery could explain the measured improvement in the Apnea-Hypopnea Index (AHI) of the patient. AHI is an index indicating the severeness of OSAS. The conclusion was that the reduction in AHI was not easy to explain from the CFD results, and several uncertainties, problems and questions arose. Mouth-breathing and the nasal cycle are likely to have an effect in reality, while these factors are not taken into account in the CFD simulations. The flow is also most likely not entirely laminar, which is the reason turbulent flow is investigated in this work.

To have a broader understanding of the purpose of the collaboration project, some theoretical background will be presented in this first chapter. Chapter 1.1 is a presentation of the anatomy of the upper airways. Obstructive Sleep Apnea Syndrome, or OSAS for short, is discussed in chapter 1.2, with focus on the anatomical mechanics, predisposing factors, symptoms, health

impacts, and available treatments. Chapter 1.3 presents turbulence models that have been used in CFD simulations in the upper airways in previous studies.

Further on in this project, in chapter 2, the governing RANS equations are given and the k-ε turbulence model is explained. Chapter 3 goes through the simulation setup, by presenting the geometry retrieval, grid generation and base-case definition. In chapter 4, the CFD results using turbulence modeling for pre- and post-operative geometries are presented and discussed, while a comparison with experimental data is performed in chapter 5. Chapter 6 presents the sensitivity study setup of the airways geometry and of inlet, outlet and wall boundary conditions, as well as grid sensitivity, and in chapter 7, these results are discussed. The thesis is summarized in the conclusion in chapter 8, and in chapter 9, questions are raised that should be investigated in further work.

Chapters 1 and 2 are for the most part directly taken from previously unpublished project work [1] by the same author as this Master thesis.

1.1 Anatomy of the upper airways
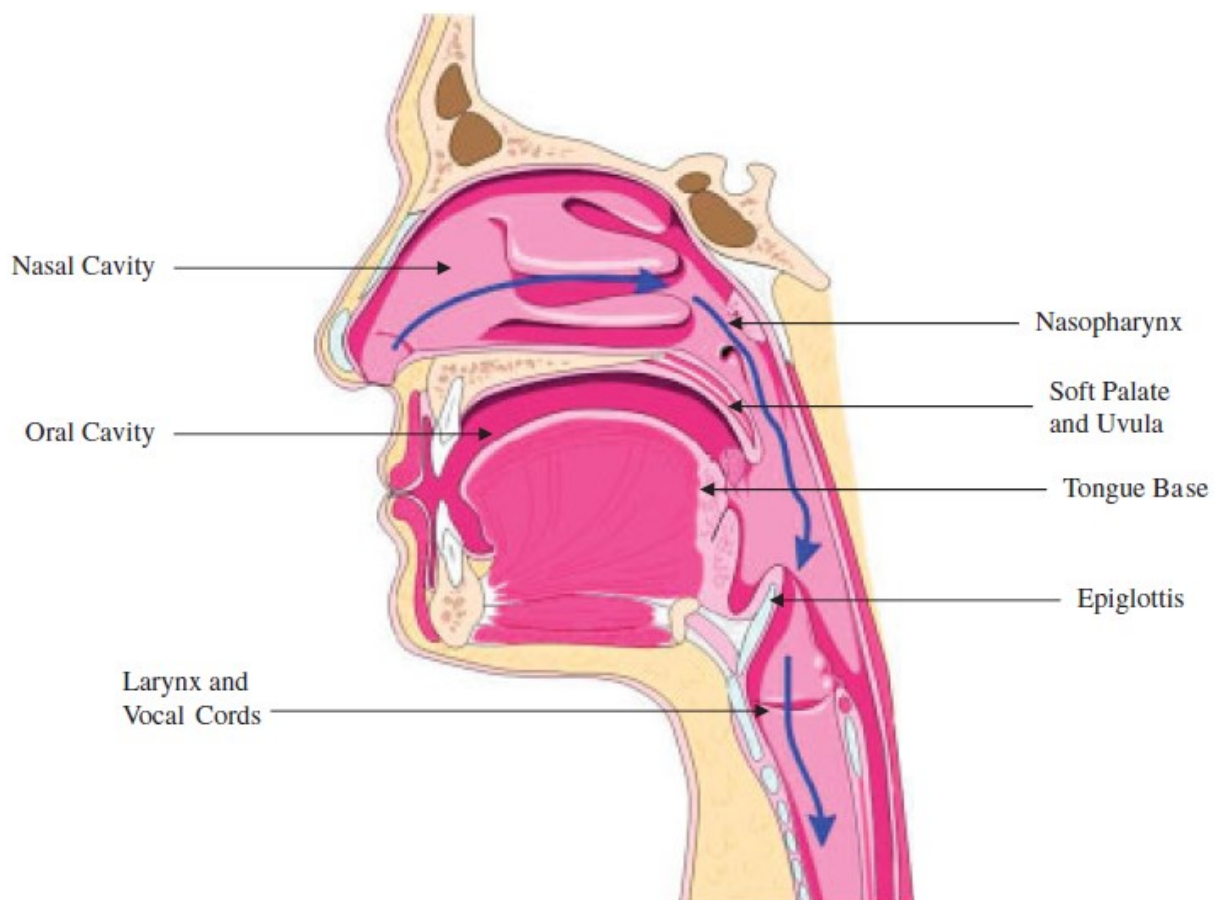
Figure 1.1: Anatomy of the human upper airways [23]

The human respiratory system can be divided into two parts; the lower airways, which is located in the chest cavity, and the upper airways above the chest cavity [23]. In OSAS, the interesting part is the upper airways, since this is where the obstruction occurs. The inflow of air begins in the nostrils and flows through the nasal cavities. The two cavities meet at the posterior choanae and open into the nasopharynx. The lower part of the nasopharynx is called the velopharynx and lies behind the soft palate and the uvula, which is very flexible and thus a location at high risk of causing snoring and sleep apnea and hypopnea. Between the soft palate and the tongue base is the oropharynx, and the tongue base is an area where obstruction during sleep is most likely to happen, due to gravity, when lying on the back. The laryngopharynx is the area between the tongue base and the larynx. In the laryngopharynx, there is a valve called the epiglottis which is the valve that separates the trachea, where the air flows, and the esophagus, which is the food tube. This is only activated when food comes down the pharynx. Thus, for breathing and OSAS, this is not considered, although it is a physical flap that interrupts the airstream and narrows the airway. Its effect will present itself in the simulations later in this report.

The upper and lower respiratory systems have their specific tasks. The nose's function is to warm, humidify and filter the air inhaled, while the lungs perform an air exchange where oxygen is exchanged for carbon dioxide [36]. The gas exchange happens at every inhalation and exhalation. The respiratory system is also in charge of sound production in the larynx, smell, and control of the body's pH level which takes place in the lungs.

1.2 Obstructive Sleep Apnea Syndrome

Snoring is a common phenomenon and is caused by soft tissue in the upper airways partly collapsing and obstructing the airways. The severeness of the obstruction determines if medical treatment is required. The most severe form is called obstructive sleep apnea syndrome (OSAS) and affects about 2% of women and about 4% of men [18], especially those over the age of 40. OSAS is a sleep disorder and causes a lot of discomfort and fatigue in the people suffering from it. A tool to diagnose it is an overnight sleep study and from that, the patient's Apnea Hypopnea Index (AHI) is determined. In addition to the AHI, the oxygen desaturation level is monitored, and these two combined can support a diagnosis. The AHI is divided into four categories; AHI<5 is mild to no OSAS, AHI 5-15 is mild OSAS, AHI 15-30 is moderate OSAS, and AHI>30 is considered severe OSAS [29].

1.2.1 Anatomical mechanics of obstructive sleep apnea
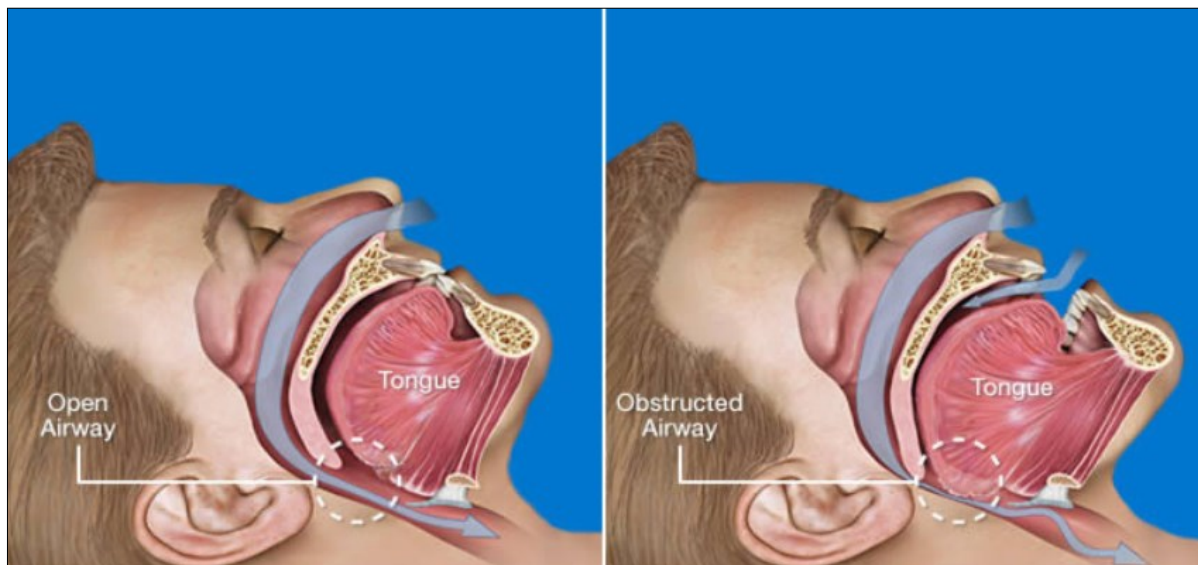
Figure 1.2: Non-obstructed (left) and obstructed (right) airway [29]

During sleep, when a person is lying on the back, gravity and the fact that the muscles are relaxed can cause the tongue base or soft palate to collapse [8]. This region is called the oropharynx and is naturally narrow even before a collapse. As seen in Figure 1.2, the airway can become partially obstructed or fully blocked. Even with little or no airflow, the person still tries to breathe. The breathing pauses can last for more than 10 seconds per episode and sometimes over a minute, and these cessations may occur several times during sleep [29]. When this happens, the brain alerts the body, resulting in increased breathing efforts, gasping, and awakenings. Typically, people with OSAS snore loudly, prior to a silent period with airway blocking, and then choking or gasping sounds as the airway opens up again. This stop in airflow prevents the gas exchange further down in the respiratory system to function optimally and this will result in reduced concentration of oxygen in the blood, hypoxemia, and a higher concentration of carbon-dioxide, hypercapnia.

1.2.2 Predisposition

There are a number of factors making certain people more predisposed for having OSAS. The main factor is obesity, especially in the upper body. Men are more predisposed than women, and family history also plays a role. Other factors are craniofacial abnormalities, enlarged pharyngeal soft tissue or lymphoid tissue, nasal obstruction, and endocrine abnormalities [6].

1.2.3 Symptoms and health impacts

Some signals can raise attention to a possible sufferer of OSAS. As mentioned, obese people are more predisposed to OSAS, and combined with snoring, this could be a sign. Other symptoms are systemic and pulmonary hypertension (high blood pressure) [6]. Sleep fragmentation is very common as OSAS patients wake up several times during the night due to disrupted breathing, and this leads to excessive daytime sleepiness, and difficulties to concentrate. This can result in an impaired quality of life, where work and everyday tasks become difficult, erectile dysfunctions are not uncommon, and people with OSAS have a higher risk of motor vehicle accidents [29]. Insomnia could also be an effect. In addition to this, some experience gastroesophageal reflux, nocturnal angina, and sleep-related cardiac dysrhythmias. OSAS patients also have an increased risk of stroke and heart disease and higher blood pressure, as well as lower glucose tolerance and higher insulin resistance [6].

1.2.4 Available treatment options

Several OSAS treatment options exist today, and they can roughly be divided into three categories: surgery, dental appliance, or non-invasive treatment with Positive Airway Pressure (PAP) ventilation.

PAP therapy is the most widely used treatment option and it is highly effective. The downside is that it is uncomfortable for the patients and noisy when used. It is still very popular and has been the standard for treatment for over 30 years, due to its non-invasive nature and good results from use. PAP machines consist of a mask or nasal pillows that deliver pressurized air through the airway, forcing the obstructed airway to open up to make sure the oxygen level in the blood is adequate [29]. Several PAP varieties exist, with CPAP (Continuous Positive Airway Pressure) being the most popular.

Dental appliance therapy is a good option if the patient has mild to moderate OSAS. There are many designs possible, but most of them are variations of mouthgards worn to keep the lower jaw postured forward, to prevent collapse in the airway. These are more handy and convenient, for instance when travelling, and are not as prominent as the PAP machines. The disadvantages are that they can be uncomfortable and they are not as effective as PAP devices [29].

The third option is surgery, which is the most invasive and risky treatment. The most common one is uvulopalatopharyngoplasty (UPPP), where tissue in the throat is surgically removed, thus widening the airway [29]. Unfortunately, the success rate of this surgery is relatively small and it is also a quite uncomfortable procedure, making it not a very desired option. Other options

include nasal surgery to straighten a deviated septum (septoplasty), orthognathic surgery on the jaw, genioplasty (reduction of the tongue) and tracheostomy, which is putting a tube directly into the neck. It is very difficult to predict the success of the surgeries, and unfortunately, the surgeries have little success, and sometimes they can even make OSAS worse. The exception is tracheostomy, which bypasses the obstruction and thus is very successful, but it is very visible and impacts everyday life by for instance that the patient cannot speak or swim. In addition, surgery is expensive, risky, uncomfortable for the patient, and post-operative complications can occur. The advantages are that when surgery is successful, it is a permanent solution to the problem, and the patient does not need to carry a PAP machine or oral appliance everywhere they go. If the diagnosis is made or suspected earlier in life, a way to treat the apnea is by removing the tonsils and/or adenoids, a surgery proven effective in children.

1.3 Turbulence models used in CFD simulations of the upper airways

Using CFD simulations in the upper airways to evaluate OSAS is relatively cheap compared to performing an actual surgery. It is a good tool to predict success and can rule out surgeries that would not be successful, a desired result for both doctor and patient. In the past, simplified models of the airways have been used, but these models have limitations. They do not reflect certain properties in the real airway, like asymmetry and varying cross-sectional area. Thus, it makes more sense to use realistic geometries to be able to take into consideration all features affecting the flow. The realistic geometries are made from MR (Magnetic Resonance) or CT (Computed Tomography) scans of OSAS patients [21].

Different turbulence models have been used for performing these CFD simulations, the most common ones being different RANS (Reynolds-Averaged Navier-Stokes) turbulence models and LES (Large Eddy Simulation). The details of the equations, advantages, and disadvantages of these turbulence models will be presented in chapter 2. This chapter will focus more on the results and success of CFD simulations conducted in previous studies.

Luo et al. [19] present an investigation of the LES method and compare it with the k-ε model, which is a type of RANS modeling, and laminar flow, in a simplified airway model. It is expected that the flow is transitional or turbulent, since the Reynolds number can be as high as 9300 during heavy breathing. The conclusion is that the LES model is most consistent with experimental results, compared to the other two. Since it is a simplified geometry, one cannot completely trust this conclusion as important features, like narrowing of the airway at several locations and thus recirculation and velocity acceleration and deceleration, are not taken into

consideration. One can agree that the laminar model is not realistic in this situation, as the flow has turbulent features because of the high Reynolds number, and this was also evident from the results.

Mihaescua et al. [21] also conclude that LES is a better option compared to k-ε and k-ω modeling, with k-ω being slightly better than k-ε. The RANS models are not able to capture flow separation effects well, which is very important in a realistic airway. Direct Numerical Simulation (DNS) is being brought up as a possible better approach, but the situation is so complex that it is argued that the needed resources are too large for the available computers, when considering data storage and speed. The article is from 2008 and computer capacity has improved over the years, but a newer article by Stylianou, Sznitman and Kassinos [35] confirms that DNS is still too demanding computationally for practical use. LES has become more affordable in the later years, but it is still more computationally demanding than RANS models. Thus, the simplified models are preferred for simulations, to reduce computational cost. In the paper by Mihaescua et al. [21], it is only the standard k-ε and standard k-ω models that have been used. If one were to find good agreement between computational results using an improved version of a RANS model and experimental results, it could be a good alternative because a RANS model generally requires less CPU time and storage.

Riazuddin et al. [28] conducted a study of inspiratory and expiratory flow in the nasal cavity using a k-ω SST turbulence model. It is considered a good model for low Reynolds number flows and for capturing effects near the wall, which is the reason why this model was chosen in the study. The model used was validated with experimental results from other studies. The results of the simulations were compared to numerical simulations from previous studies and showed good correlation. Also, the CFD results provided more detailed flow patterns than experimental findings were able to. The conclusion was that the k-ω SST model gave accurate and reliable results for the flow involving adverse pressure gradients.

Some studies have also been conducted where a one-equation model has been used, for instance by Nithiarasu, Liu and Massarotti [24], who used the Spalart-Allmaras (SA) model, a generally cost effective model compared to other models. In this paper, the authors stated that their experience showed that the SA model is simple and suitable for calculations of complex flow. They concluded that the results agreed qualitatively with other published data. An unstructured mesh was used, facilitating fast mesh generation, but the number of points needed in the domain increased, making the overall cost higher.

The paper by Mylavarapu et al. [22] challenges the statement in the previous paragraph, saying that the SA model performs poorly compared to other turbulence models. In the study, they have performed experiments on an anatomically accurate model of the upper airways constructed from MR images, and conducted CFD simulations for several turbulence models. The results were then compared to find the turbulence model that gave the best agreement with experiments. It was concluded that the standard k-ω model agreed the best with experimental results, with LES and the k-ω SST model following close behind. The SA model performed the worst in predicting pressure, but it is argued that the one-equation model not necessarily is bad, it just needs better predictions of model coefficients to perform better in the complex geometry.

Several articles focus on solving problems with particle deposition and aerosol delivery, but to do so, they must also conduct flow simulations to understand particle transportation. Ma and Lutchen [20] use a realizable k-ε model when simulating flow and aerosol delivery, and compare their results with experimental data. The simulation results agree well with data and expected results. A standard k-ε model is used by Stapleton et al. [34], but the conclusion here is that the results of the CFD simulation do not correspond very well with experimental data. It is discussed that a reason for this could be that particle deposition is very sensitive to pressure drop and recirculation, highlighting the need for accuracy in the simulation to obtain good results. One can also point out that the realizable k-ε model performs better if the flow has a strong pressure gradient, flow separation and recirculation [20], which is the case for the upper airway, than the standard k-ε model and also the RNG (Renormalization Group) k-ε model. Note that special treatment for near-wall regions is necessary to get a good result for flow near the wall. In simulation software, this can for instance be enhanced wall treatment, where a two-layer approach is implemented and combined with enhanced wall functions [5]. Longest and Vinchurkar [17] also consider aerosol deposition, but use the k-ω turbulence model. The standard k-ω model presents good agreement with empirical results, but implementing a low-Reynolds number (LRN) k-ω model improves this result even further. However, accurate inlet conditions are required for good results.

The studies all agree that CFD analysis of the human upper airways is a great tool for giving a realistic representation of flow related problems. Choosing a specific turbulence model can be difficult, because it depends, among other things, on the geometry and Reynolds number. Knowing if you have fully turbulent or transitional flow is important for choosing an accurate model. Literature suggests that standard turbulence models are not always accurate enough, but improved models that take into consideration turbulence effects such as recirculation and

separation, can provide results that agree well with empirical data. When deciding on a model, one also has to consider cost, because some models are very accurate, but also very costly. For instance, LRN k-ω needs a very fine mesh to provide accurate results, which also means more data storage and more computational work.

In the previous work by Aasgrav [1] and Aasgrav et al. [2] (see Appendix A), an investigation of the effect of choice of turbulence model was performed. Laminar results were compared to results from four different turbulence models, namely the standard k-ε and k-ω models as well as the realizable k-ε model and the k-ω SST model. The results from the turbulence models were not so different from the laminar result, because of the low maximum Reynolds number of about 2000 for the chosen volumetric flow rate of 250 ml/s. For larger flow rates and Reynolds numbers, the flow may have more turbulent features, such that a turbulence model is expected to handle a wider range of flow conditions than a laminar model. The results for the four different turbulence models were similar, leading to the conclusion that, for this particular flow rate, the choice of turbulence model is insignificant to the results. However, this must be investigated further (e.g. at higher Reynolds numbers) before a general conclusion on turbulence models' significance to CFD model results can be stated. A major challenge in this regard is the lack of available clinical measurement data.

2 Mathematical models

There exists a variety of mathematical models that try to predict flow. In this chapter, some of them will be presented and compared. The governing equations will be presented, explained, and discussed. In chapter 2.1, the focus will be on the governing equations for laminar flow, while chapter 2.2 will discuss turbulent flow and the k-ε turbulence model. Lastly in this chapter, in 2.3, the boundary conditions for the flow will be discussed.

Because we are dealing with slow flows of about 1 m/s, i.e. Mach number of about 0.003, the Mach number is well below 0.3. This yields density variations well below 10%, implying that we can consider the flow to be incompressible.

2.1 Governing equations

The Navier-Stokes equations describe fluid flow and thus are the foundation of modeling of flow. They represent the momentum equation, but are in CFD accompanied by the equation for conservation of mass, also called the continuity equation [27]. For incompressible flow, the continuity equation is

$$\nabla \cdot \boldsymbol{U} = 0, \qquad\qquad (2\text{-}1)$$

and the momentum equation is

$$\frac{D\boldsymbol{U}}{Dt} = -\frac{1}{\rho}\nabla p + \nu\nabla^2\boldsymbol{U}, \qquad\qquad (2\text{-}2)$$

where $\boldsymbol{U}$ denotes the velocity vector consisting of components in three directions. ρ is the density, p is the pressure and ν is the constant kinematic viscosity. $\frac{D\boldsymbol{U}}{Dt}$ is the material derivative of the velocity:

$$\frac{D\boldsymbol{U}}{Dt} = \frac{\partial \boldsymbol{U}}{\partial t} + (\boldsymbol{U} \cdot \boldsymbol{\nabla})\boldsymbol{U} \qquad\qquad (2\text{-}3)$$

2.2   Turbulent flow

Several turbulence models have been presented and developed over the years. The most utilized ones are based on the Reynolds-averaged Navier-Stokes (RANS) equations. The Reynolds stress models are generally divided into categories based on how many equations need to be solved; zero equations, one equation, two equations or more. Today, the two-equation models are the most used and the most verified RANS types. Therefore, two-equation RANS models will be presented in this chapter, alongside brief introductions of two other models which previous studies have shown provide good results.

Direct Numerical Simulation (DNS) is solving the Navier-Stokes equations numerically without a turbulence model. DNS solves for all spatial and temporal scales, from the smallest, dissipative scales to the largest scales. It is one of the newest approaches, as it requires much computer power and was not feasible until the 1970s, when computers became faster [27]. Still, it is very costly, with the cost increasing rapidly with Reynolds number, $\sim Re^{9/4}$. Thus, it can only be applied to low Reynolds number flow. Even with high accuracy and a simple approach, the high cost makes the method impractical in reality.

Large Eddy Simulation (LES) is a turbulence model where the large-scale turbulent eddies containing anisotropic energy are represented explicitly, while the smaller-scale, more isotropic turbulent motions are represented by simple models. Compared with DNS, this approach makes the computational cost significantly lower. Still, the cost is higher than RANS, a turbulence model which will be presented in the next section, and the cost is often too high for LES to be practical in larger simulations. The concept of LES is that the flow field $U(x, t)$ is divided into a filtered component $\overline{U}(x, t)$ and a residual component $u'(x, t)$, large and small-scale flow features respectively [27]. The residual component is also called a subgrid-scale component. The Navier-Stokes equations give equations for the evolution of the filtered velocity field, where the momentum equation contains the subgrid-scale (SGS) stress tensor coming from the residual motions, which are unresolved turbulent motions in the sub-grid scale [26]. The SGS stress tensor is usually solved by an eddy-viscosity model. The filtered equations are solved numerically for $\overline{U}(x, t)$ to give an approximation for the development of the large-scale motions of turbulent flow, given an initial velocity field. The LES model lies between DNS and RANS, both when it comes to accuracy and computational cost. It works well with more complex flows, where unsteady, separated or vortical flow features occur [21], and large Reynolds number flows. LES is desired because of its good agreement with experimental results [19], but one still has to consider cost when deciding if LES should be employed.

The basis for the RANS approach is the momentum equation (2-2). In turbulent flows, the properties become random in time and space, making them difficult to model. Thus, we need to split the properties into simpler forms, making the calculations easier [27]. They become

$$u_i = U_i + u_i', \quad p = P + p',$$
(2-4)

where the velocity and pressure are the sums of mean and fluctuating parts, respectively. They satisfy

$$\overline{u_i} = U_i, \quad \overline{u_i'} = 0$$
(2-5)

$$\overline{p} = P, \quad \overline{p'} = 0$$
(2-6)

where the bar denotes the time average. Combining equations (2-2) and (2-4), and taking the time average yields the Reynolds-averaged Navier-Stokes (RANS) equations

$$\frac{\partial U_i}{\partial x_i} = 0$$
(2-7)

$$\rho \frac{\partial U_i}{\partial t} + \rho \frac{\partial}{\partial x_j}\left(U_i U_j\right) = -\frac{\partial P}{\partial x_i} + \frac{\partial}{\partial x_j}\left(2\mu S_{ij} - \rho \overline{u_i' u_j'}\right),$$
(2-8)

where S_{ij} is the mean strain-rate tensor:

$$S_{ij} = \frac{1}{2}\left(\frac{\partial U_i}{\partial x_j} + \frac{\partial U_j}{\partial x_i}\right).$$
(2-9)

By combining these three equations, (2.7)-(2.9), and assuming ν is constant, a new expression arises;

$$\frac{\partial U_i}{\partial t} + U_j \frac{\partial U_i}{\partial x_j} = -\frac{1}{\rho}\frac{\partial P}{\partial x_i} + \nu \frac{\partial^2 U_i}{\partial x_j \partial x_j} - \frac{\partial \overline{u_i' u_j'}}{\partial x_j}.$$
(2-10)

Now, 6 new quantities $\overline{u_i' u_j'}$ have been introduced, but no additional equations have accompanied them, so the system is not closed. This means we must find more equations to solve for all the unknowns, i.e. the turbulent stress. For this, we introduce the RANS turbulence models [27]. They are, by far, the most used models over the years. This is why we have chosen to study these models further, and a specific RANS model approach and its equations are presented in the following subchapters.

The Boussinesq approximation is a turbulent viscosity hypothesis, stating the relationship between Reynolds stress and the mean rate of strain [27]. This hypothesis introduces enough equations so that the system of equations is closed. The Boussinesq approximation is

$$-\overline{u_i' u_j'} = 2v_T S_{ij} - \frac{2}{3} k \delta_{ij} ,$$

(2-11)

where v_T is the eddy viscosity, k is the turbulence kinetic energy, and δ_{ij} is the Kronecker delta.

2.2.1 k-ε models

The k-ε models are two-equation models based on transport equations for the turbulent kinetic energy k and the dissipation rate ε [15]. For the standard k-ε model, assumptions of fully turbulent flow are made, and thus, this standard model is only valid for fully turbulent flows. In our problem, it is difficult to know if the flow is fully turbulent or only partially turbulent. The standard k-ε model needs to make implementations for wall treatment, depending on the Reynolds number. For low Re, a finer mesh near the wall is needed, while for high Re, wall functions must be implemented near the wall [4]. This turbulence model does not give good predictions for flows with high streamline curvature and strained flows [30], but the standard k-ε model is included because it serves as a basis for an improved turbulence model utilized in this thesis. The equations for but the standard k-ε model are as follows:

- Kinetic eddy viscosity:

$$v_T = \frac{C_\mu k^2}{\varepsilon}$$

(2-12)

- Turbulence kinetic energy:

$$\frac{\partial k}{\partial t} + U_j \frac{\partial k}{\partial x_j} = \frac{\tau_{ij}}{\rho} \frac{\partial U_i}{\partial x_j} - \varepsilon + \frac{\partial}{\partial x_j} \left[(v + \frac{v_T}{\sigma_k}) \frac{\partial k}{\partial x_j} \right]$$

(2-13)

- Dissipation rate:

$$\frac{\partial \varepsilon}{\partial t} + U_j \frac{\partial \varepsilon}{\partial x_j} = C_{\varepsilon 1} \frac{\varepsilon}{k} \frac{\tau_{ij}}{\rho} \frac{\partial U_i}{\partial x_j} - C_{\varepsilon 2} \frac{\varepsilon^2}{k} + \frac{\partial}{\partial x_j} \left[(v + \frac{v_T}{\sigma_\varepsilon}) \frac{\partial \varepsilon}{\partial x_j} \right]$$

(2-14)

- Closure coefficients and relations:

$$C_{\varepsilon 1} = 1.44, \ \ C_{\varepsilon 2} = 1.92, \ \ C_\mu = 0.09, \ \ \sigma_k = 1.0, \ \ \sigma_\varepsilon = 1.3$$

(2-15)

14

$$\tau_{ij} = -\rho \overline{u'_i u'_j} \qquad (2\text{-}16)$$

The k-ε model has been revised, and improved versions of the standard model have been presented. The RNG k-ε model is similar to the standard one, but in the equation for the dissipation rate, an additional term is included to cover the interaction between turbulence dissipation and mean shear [15]. It also covers swirl effects. The RNG k-ε model has better predictions than the standard one for flows with high streamline curvature, separation, high strain rate, transitional flows, and wall heat and mass transfer. However, it does not predict the spreading of a round jet well. The realizable k-ε model is another version of the k-ε model, and since this is the chosen turbulence model for our problem [1], it is discussed in more detail in the subchapter below.

2.2.1.1   Realizable k-ε model

The term realizable means that the model satisfies some mathematical constraints in the Reynolds stresses that the standard and RNG k-ε turbulence models do not. When the strain in the flow becomes very large, the normal stress becomes negative, i.e. non-realizable. The realizable k-ε model accounts for this and makes sure the normal stress is always positive, i.e. realizable [32]. The realizable k-ε turbulence model has the same improved predictions for boundary layers with high pressure gradients or separation, recirculation, and high streamline curvature as the RNG k-ε model. In addition, the realizable k-ε model has more accurate predictions for the spreading rate of both planar and round jets. In our problem, with the upper airway system, many of these effects are highly present, making it a suitable model. Compared to the equations for the standard k-ε model, the realizable model has an improved equation for ε, and in addition, C_μ is a variable and not a constant [15].

The equation for the dissipation rate ε is similar to the one for the standard k-ε model, but has an additional term, which is the last term in the dissipation rate equation below:

$$\frac{\partial \varepsilon}{\partial t} + U_j \frac{\partial \varepsilon}{\partial x_j} = C_{\varepsilon 1} \frac{\varepsilon}{k} \frac{\tau_{ij}}{\rho} \frac{\partial U_i}{\partial x_j} - C_{\varepsilon 2} \frac{\varepsilon^2}{k} + \frac{\partial}{\partial x_j}\left[\left(\nu + \frac{\nu_T}{\sigma_\varepsilon}\right) \frac{\partial \varepsilon}{\partial x_j}\right] + C_1 S \varepsilon \quad (2\text{-}17)$$

$$C_1 = \max\left[0.43, \frac{\eta}{\eta + 5}\right], \ \eta = S\frac{k}{\varepsilon}, \ S = \sqrt{2S_{ij}S_{ij}} \qquad (2\text{-}18)$$

Opposed to $C_\mu = 0.09$, cf. equation (2-15) in the standard k-ε model, the parameter C_μ in the realizable k-ε model used in the kinetic eddy viscosity equation (2-12) is computed from [32]:

15

$$C_\mu = \frac{1}{A_0 + A_S \dfrac{U^* k}{\varepsilon}} \qquad (2\text{-}19)$$

$$U^* = \sqrt{S_{ij} S_{ji} + \Omega_{ij} \Omega_{ji}} \qquad (2\text{-}20)$$

$$A_0 = 4.04, \quad A_S = \sqrt{6} \cos\phi, \quad \phi = \frac{1}{3} \cos^{-1}(\sqrt{6} W) \qquad (2\text{-}21)$$

$$W = \frac{S_{ij} S_{jk} S_{ki}}{\tilde{s}^3}, \quad \tilde{s} = \sqrt{S_{ij} S_{ij}} \qquad (2\text{-}22)$$

where Ω_{ij} is the mean rate of rotation;

$$\Omega_{ij} = \frac{1}{2}\left(\frac{\partial U_i}{\partial x_j} - \frac{\partial U_j}{\partial x_i}\right), \qquad (2\text{-}23)$$

and S_{ij} is the mean strain-rate tensor found in equation (2-9).

2.3 Boundary conditions

Setting boundary conditions for flow in the human respiratory system is challenging. For many problems, the inlet condition is a given velocity and the outlet condition is a given pressure. In our problem, this proves impractical. In our geometry, the outlet condition has to be determined at the end of the larynx. Since the position for the inspirational flow outlet is inside the body, it is difficult to set a precise value for the pressure at the outlet. What we do know is that in order for the internal organs to function properly and the amount of oxygen flowing out to the organs being correct, a certain volumetric flow has to circulate in the system. Therefore, the outlet condition is set as the flow rate of slow breathing, as suggested by Kleinstreuer and Zhang [16], namely 250 ml/s. Setting an inlet condition can be challenging as well, since there are two inlets, namely the left and right nostril, and inflow velocity is most likely different for the two nostrils due to area and resistance differences. Having the total gauge pressure as an inlet condition will ensure identical pressure drop over the two cavities, even if there are different resistances, by regulating the flow rate. This comes from the Hagen-Poiseuille equation [14], $\Delta p = R * q$, where Δp is the pressure drop, R is the resistance, and q is the volumetric flow rate. We choose to set the inlet condition as a total gauge pressure equal to 0 Pa, since there is atmospheric pressure around the nostrils. The boundary condition on the wall is usually set as a no slip condition, i.e. velocity is zero at the wall, but in our problem, this might not be the

case, since there are both hair and mucus present in the nose, causing disruptions in the flow. However, studying the effect of slip is beyond the scope of this report, so we assume no-slip at the wall. The wall is also assumed to be smooth, i.e. to have zero roughness height.

The basis for the turbulence models' boundary conditions is the law of the wall [33]. It describes the velocity profile in the turbulent boundary layer in the log region, assuming constant shear stress through the layer. It results in the profile depicted in Figure 2.1.
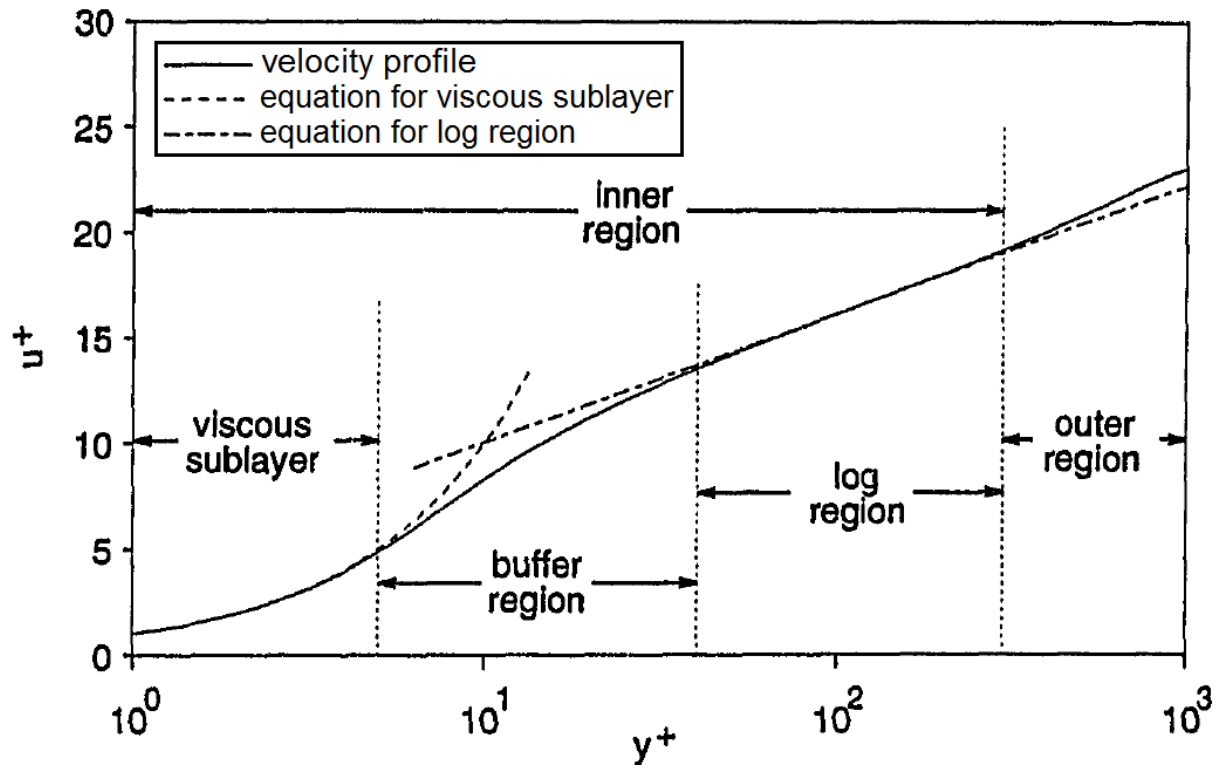
Figure 2.1: Velocity profile in the turbulence boundary layer; law of the wall [33]

In the logarithmic layer, the equation describing the velocity profile is

$$u^+ = \frac{1}{\kappa}\ln(y^+) + B \,,$$

where κ is the von Karman constant and B is another constant. Their values have been determined empirically to κ in the range 0.40-0.41 and B in the range 4.9-5.5. u^+ is a non-dimensional velocity and y^+ is a non-dimensional length, whose definitions are

$$u^+ = \frac{u}{u_*} \,,\; y^+ = \frac{u_* y}{\nu} \,,$$

and u_* is the friction velocity;

17

$$u_* = \sqrt{\frac{\tau_w}{\rho_w}} \, .$$

τ_w is the wall shear stress and ρ_w is the density at the wall. In the viscous sublayer, all turbulent fluctuations are damped out and the equation describing the streamwise velocity profile is

$$u^+ = y^+ \, .$$

3 Simulation setup

This section is mainly taken from the author's specialization project [1].

3.1 Geometry retrieval

When specifying a patient specific geometry, one must retrieve the geometry from medical images. This is a process that has been described in detail in the specialization project by Jordal [11], the master's thesis by the same author [12] and by Jordal et al [13]. The geometry retrieval from CT scans was done by segmentation, performed in the free software ITK-SNAP [9]. The medical images were provided by the radiologic department at St Olav University Hospital. The patient is patient number 12 in the study, a 67-year-old man who showed great improvement in AHI, from 22.8 before surgery to 5.7 after the nasal surgery, and he was no longer diagnosed with OSAS. The geometries used in this project are from both the pre-operational and post-operational images, established by Jordal [12]. The resulting 3D geometries from the pre- and post-operative images are shown in Figure 3.1 and Figure 3.2.

*Figure 3.1: Retrieved 3D-geometry from before (left)
and after (right) surgery, seen from the front*

19
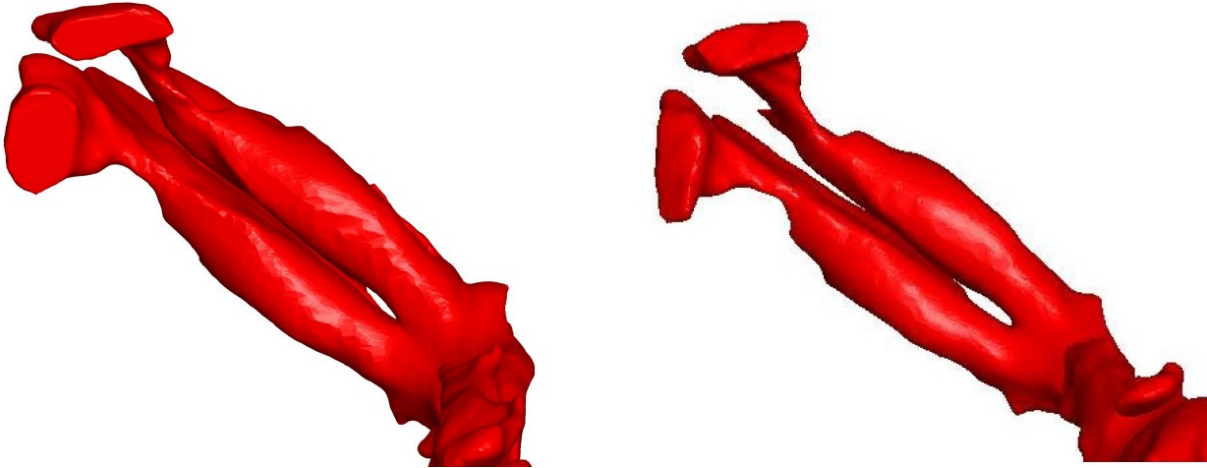
Figure 3.2: Retrieved 3D-geometry of the nasal cavity from before (left) and after (right) surgery, seen from below

The surgery performed on the patient was a septoplasty, which is straightening of a deviated septum. The septum is the cartilage wall separating the two nasal cavities. This means that the only difference between the pre- and post-operative geometry should be in the nasal cavity. From Figure 3.1 we see that this is not the case, probably due to different positioning of the patient when performing the CT scans. Therefore, the post-operative geometry was created by cutting the post-op. geometry in the nasopharynx and joining it to the lower parts of the pre-operative geometry [12]. This is done to eliminate the difference in the lower parts of the geometry, which would have given irrelevant effects on our results. The geometry differences could be due to e.g. the nasal cycle, where the air flow through the nasal cavities is asymmetrical due to one of the nasal passages being dominant [12], different level of airway infection or human error. Further work is required to investigate and eliminate these sources of error.

To get an even distribution of the outflow, and thus better results, the choice in the thesis by Jordal [12] was to cut off the geometries in the trachea and extend it using ANSYS DesignModeler [3]. The cut-off angle was slightly different for the pre- and post-operative geometries because the cut-off planes were decided by their normals defined as pointing in the flow direction and since the geometries are different in the nasal cavities, the flow becomes somewhat different in the trachea as well. This leads to different directions for the extensions and also slightly different outlet areas. It is assumed, and later observed, that the geometry in this area have negligible impact on the flow patterns from the nasal cavity down to the beginning of the larynx, which is the crucial area in this project. The final geometries of the pre- and post-operative models are depicted in Figure 3.3.
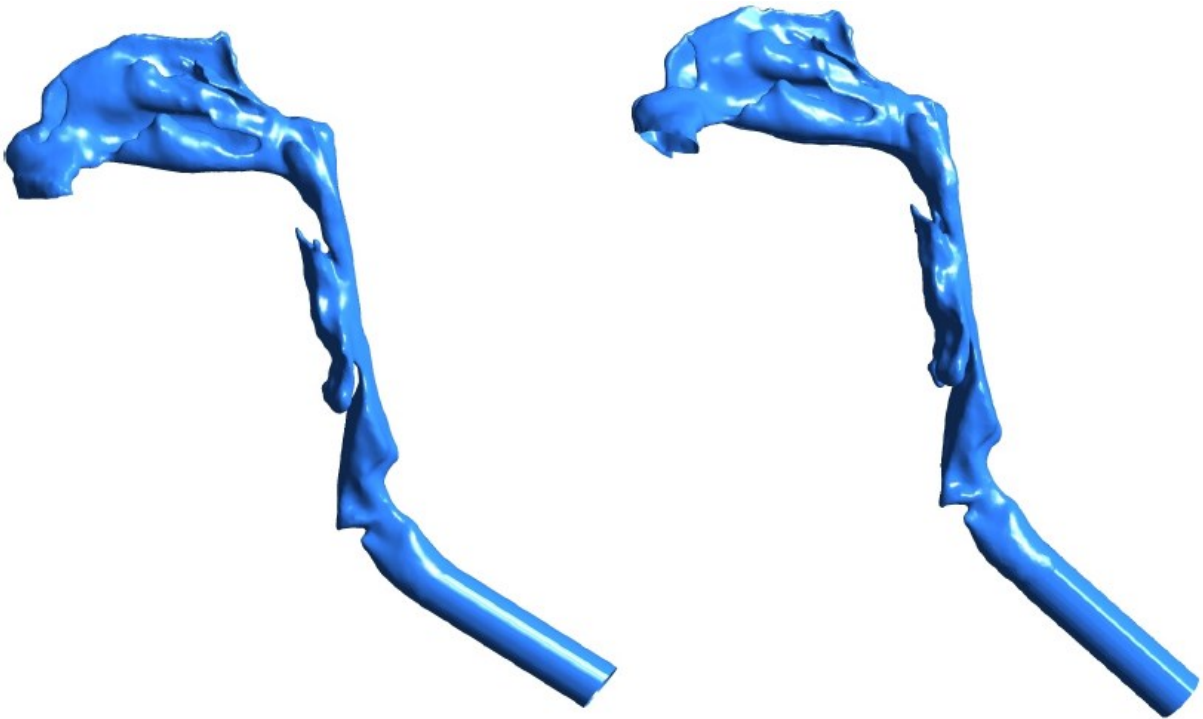
Figure 3.3: Final pre- and post-operative models used in simulations, seen from the left [12]

3.2 Grid generation

In computational fluid dynamics (CFD), mathematical equations describe the evolution of fluid flow. These equations are solved over a domain. To enable numerical solution of governing equations (see Ch. 2), the computational domain is discretized into smaller control volumes. In general, the smaller the control volumes are, the more accurate the numerical solution is since gradients and fluid structures in the flow are better resolved. The equations are then solved for each grid cell. It is therefore essential to have a grid that captures the important features of the flow, without introducing dominating numerical errors, to obtain a good result. The number of operations and where each flow variable is solved is defined by the size of the cells and grid structure, and thus how many grid cells there are. It is important to have small enough grid cells so that the solution is accurate, but at the same time, the computational time increases with the resolution, forcing an upper limit on the number of cells that is applicable. Many types and classifications of grids exist (e.g. structured or unstructured), and the best suited type depends on the geometry, velocity, flow patterns and set of governing equations. Structured grids in 3D are made up of hexahedrons, while unstructured grids may consist of an irregular pattern made up of prisms, tetrahedrons and/or other polyhedra. For complex geometries, such as the upper airways, an unstructured mesh is best for capturing the irregularities in the geometry [12].

To assess grid quality with respect to numerical error and convergence, different mesh metrics are calculated by the meshing software, e.g.:

- Aspect ratio (ratio between base and height, measures the stretching of the cell); usually between 0 and 20, can also be higher, best to be close to 1
- Skewness (how skewed a cell is, measures the difference between the shape of the cell and the shape of an equilateral cell of equivalent volume); between 0 and 1, with 0 being the best
- Orthogonal quality; ranging from 0 to 1, with 1 being the best

It should be noted that a coarse grid of high quality may give an incorrect result, as the grid quality is a measure of how easy the simulation converges. Although a grid satisfying the above criteria is considered to be of good quality in a numerical context, resolution of important features of the flow demands a grid sensitivity study. The most common method is to run the same simulation setup on several meshes with different resolution. When refining the mesh cease to impact the results, grid independence has been achieved.

In our problem, a complex geometry needed to be meshed. This was done in ANSYS Meshing, version 16.2 [3]. The meshing was performed by co-supervisor Sverre Gullikstad Johnsen at SINTEF Materials and Chemistry [10]. In the pursue of resolving the fine and important scales close to the wall, an inflation layer consisting of 5 layers was enforced at the wall, to resolve velocity gradients at the wall better. The inflation layer had a growth rate of 1.2 and a transition ratio of 0.272. The option "Relevance Center" was set to coarse to have a coarser grid away from the wall, but by implementing a size limitation instead, this option is overruled. The size limitation was that the element size was not to exceed 1 mm. The option "Size Function" in ANSYS Meshing was set to "Proximity and Curvature", where proximity captures the effects of narrow gaps and thin sections, such as in the nasal cavity, and curvature captures sharp changes in flow direction, like we have in the nasopharynx. The rest of the variables were set as the default suggested by ANSYS Meshing. These steps were repeated for both the pre- and post-operative geometries. This resulted in a mesh with about 1.4 million grid cells for the pre-operative geometry, where the majority of the mesh consists of tetrahedrons, except the inflation layer which consists of prisms with triangular bases and a low height. The mesh metrics for this mesh showed that the majority of the cells were of good quality, with only a small portion being poor. Poor mesh quality can for instance come from the inflation layer, as the cells in this layer are very flat compared to their width. Since most of the cells were of good quality, the mesh was defined as the base case mesh implemented for simulations and

investigations. Close-up pictures of the pre-operative mesh can be seen below, in Figure 3.4, Figure 3.5 and Figure 3.6. The meshing of the post-operative geometry was performed in the same way as the pre-operative mesh with the same size limitation. This produced a post-operative mesh of about 1.3 million cells grid cells. The mesh quality showed the same features as the pre-operative mesh and was kept for the post-operative simulations.
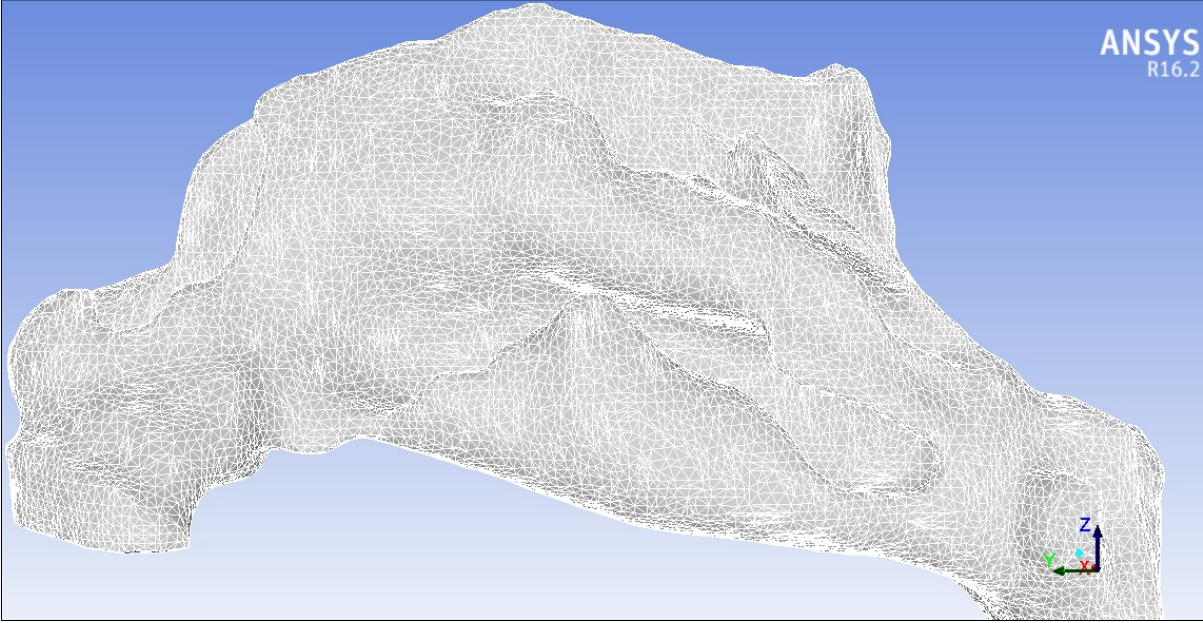
Figure 3.4: Close-up picture of mesh at the wall of the nasal cavity, pre-operative geometry
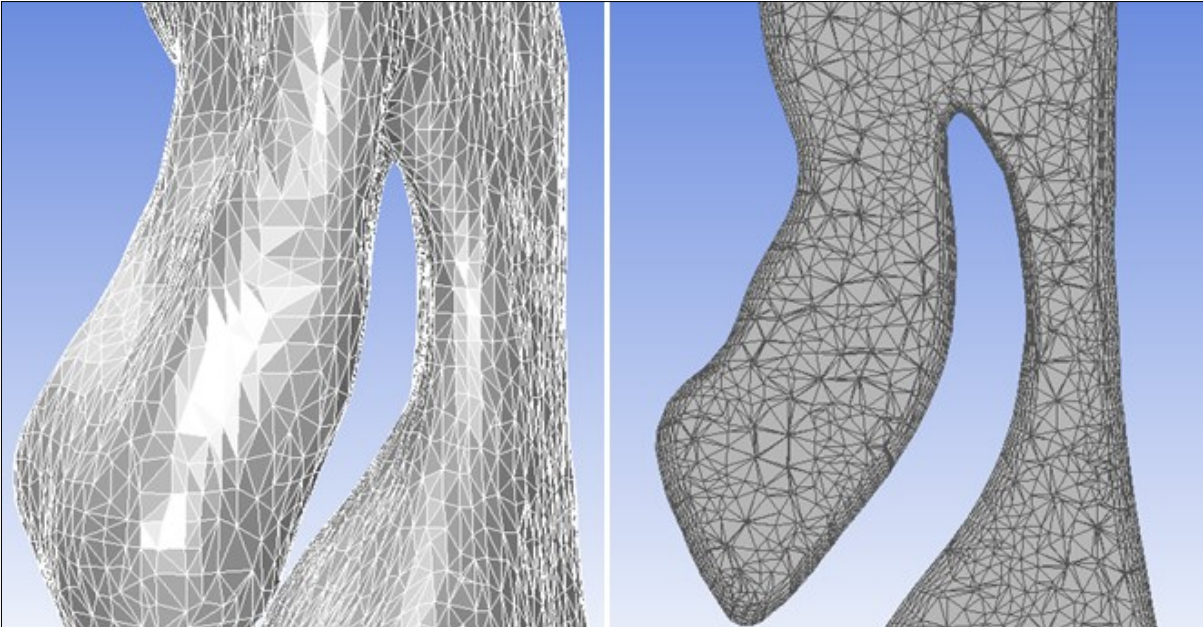
Figure 3.5: Mesh at the epiglottis for the pre-op. geometry; at the wall and in a cut-through plane
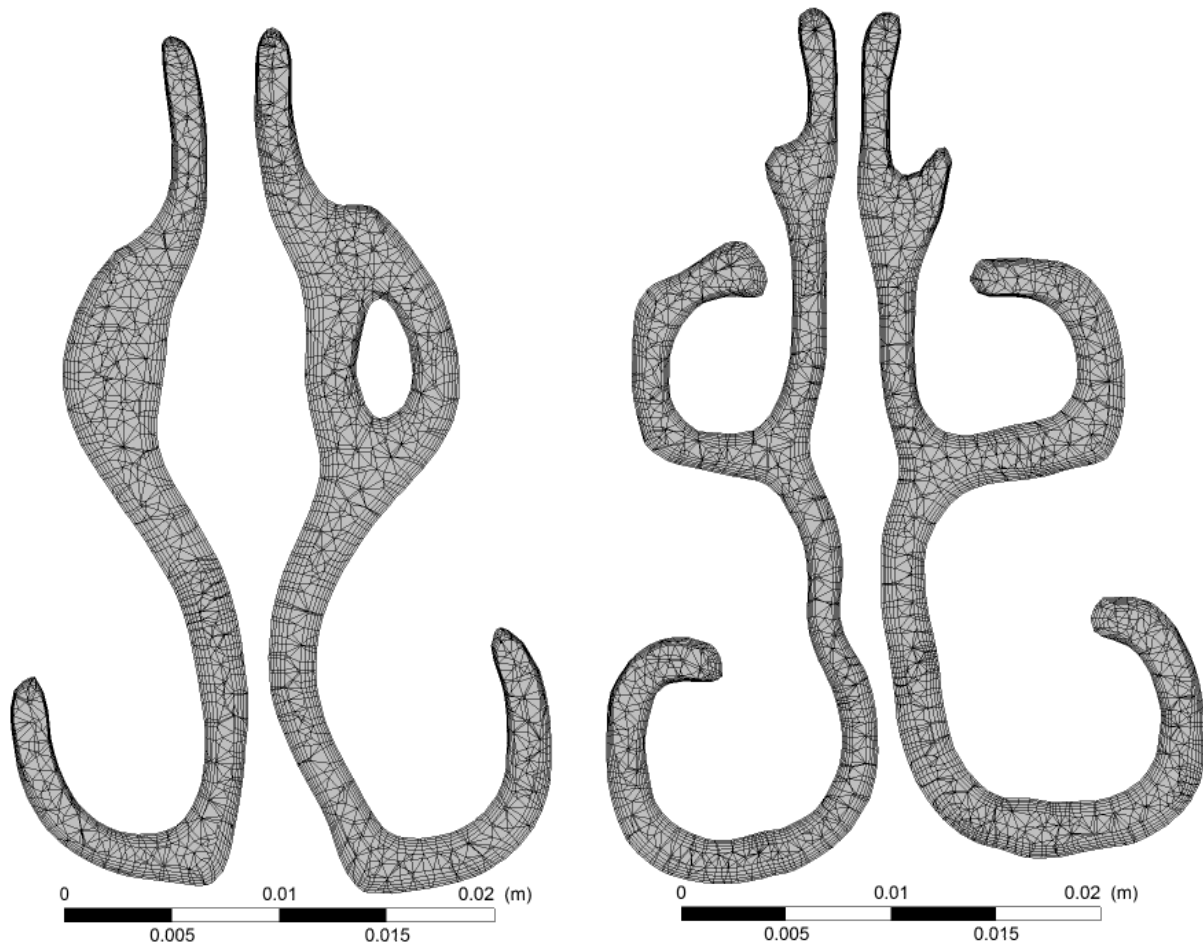
Figure 3.6: Mesh at two cut-through planes in the nasal cavity for the pre-operative geometry

3.3 Base case

Base cases were established for both the pre- and post-operative simulations. The base case meshes are, as described in the previous subchapter, consisting of 1.4 million grid cells for the pre-operative geometry and of 1.3 million grid cells for the post-operative geometry.

The boundary conditions are stated for the base case, and are the same for both pre- and post-operative simulations. The outlet condition is a velocity, set as a negative inlet velocity, corresponding to a volumetric flow rate of 250 ml/s. The outlet velocity magnitudes are slightly different for the pre- and post-operative geometries, since the outlet areas had a small deviation from each other due to different cut angles when extending the trachea (cf. Ch. 3.1). The inlet condition for both situations is a total gauge pressure of 0 Pa. Turbulence intensity (TI) and turbulent viscosity ratio (VR) at the inlet was set to 5% and 10 respectively, and the wall boundary conditions were defined as no slip and smooth wall, i.e. zero roughness height.

The flow is assumed to be in steady state. The turbulence model used for all calculations is the realizable k-ε turbulence model [2]. The enhanced wall treatment option [3] was invoked to allow for low Reynolds number corrections close to the wall.

The software suggests default reference values, under-relaxation factors, and turbulence model constants. They have all been kept as suggested. The values for the under-relaxation factors and turbulence model constants for the base case are listed in Table 3.1 [1].

Table 3.1: Values for variables in flow simulation [1]

	Variable	**Value**
Under-relaxation factors	Density	1
	Body forces	1
	Turbulent kinetic energy	0.8
	Turbulent dissipation rate	0.8
	Turbulent viscosity	1
Model constants	C2-epsilon	1.9
	TKE Prandtl number	1.0
	TDR Prandtl number	1.2

The model constants are constants in the k-ε turbulence model. C2-epsilon ($C_{\varepsilon2}$) is a constant presented in (2-14), the equation for dissipation rate. TKE Prandtl Number is the turbulent kinetic energy Prandtl number, which is labeled σ_k in (2-13). TDR Prandtl Number is the turbulent dissipation rate Prandtl number, which is labeled σ_ε in (2-14). In (2-15), the constants have different values than what was suggested by ANSYS Fluent, but the default in the software was kept for the simulations. The solvers utilized are also kept as the default, except the pressure-velocity decoupling. Experience shows that a coupled solver is faster than the SIMPLE solver, so a coupled solver was chosen for the pressure-velocity decoupling [1]. For the spatial discretization, second order solvers are generally more accurate, but also have a higher cost, while first order solvers might be less accurate, but have a lower cost. One must consider cost versus accuracy when determining whether to use first or second order solvers. The solvers chosen for spatial discretization in the base case are listed in Table 3.2.

Table 3.2: Solvers used for spatial discretization in flow simulation [1]

Equation	Solver
Gradient	Least squares cell based
Pressure	Second order
Momentum	Second order upwind
Turbulent kinetic energy	First order upwind
Turbulent dissipation rate	First order upwind

4 Pre- and post-operative results

Ten cut-through planes are defined for both the pre- and post-operative geometries, as well as the inlet and outlet planes. Their locations and numbering are presented in the figures below.
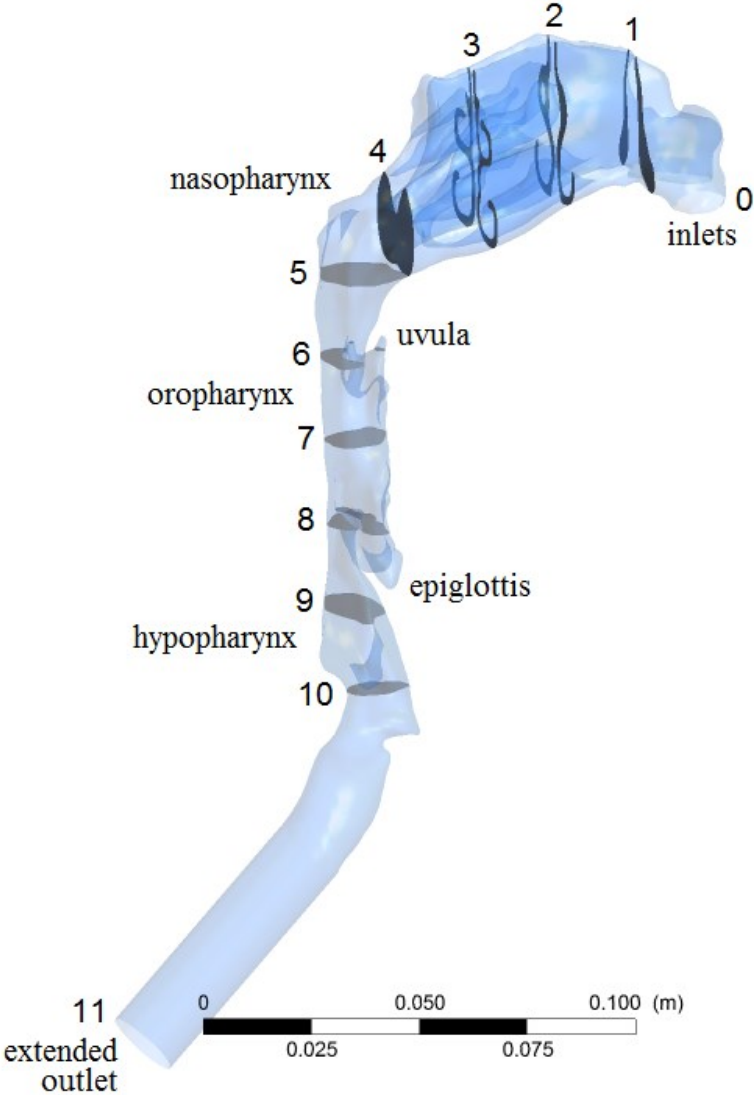
Figure 4.1: Location and numbering of cross-sections in pre-operative geometry
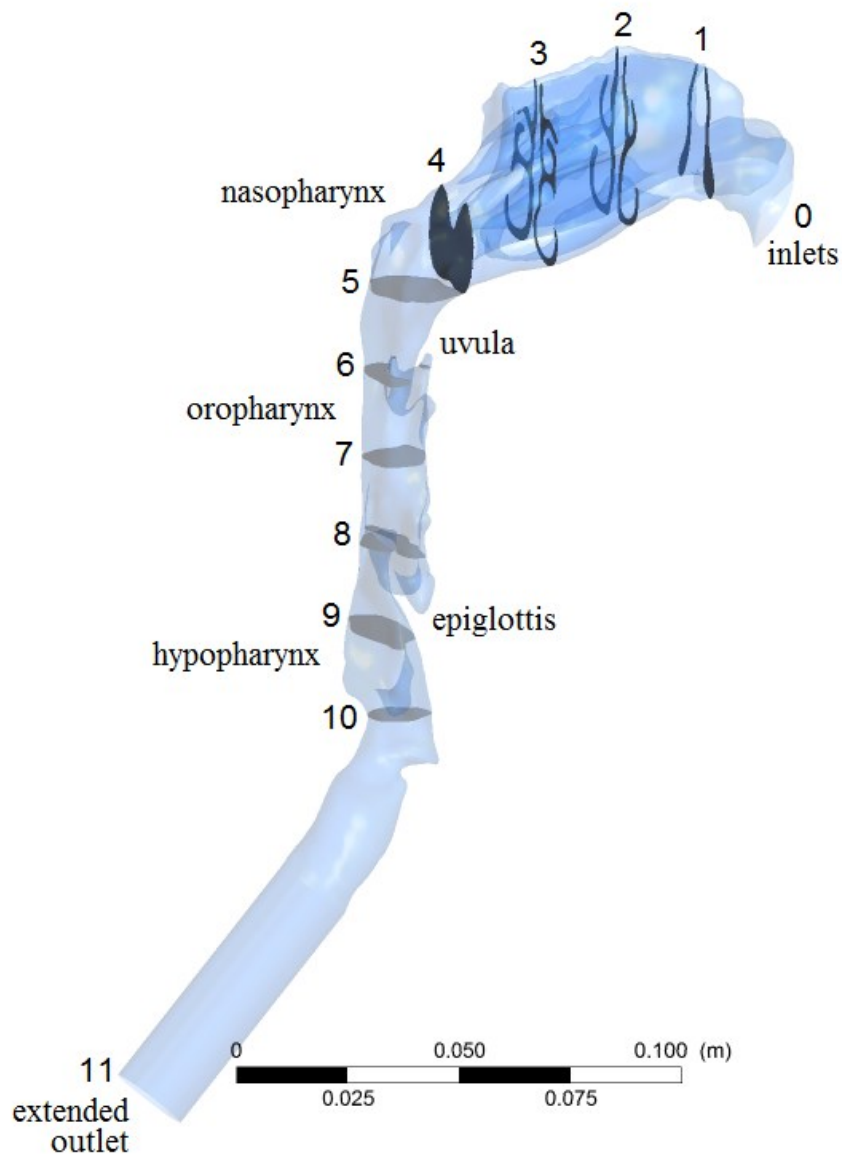
Figure 4.2: Location and numbering of cross-sections in post-operative geometry

Various results were extracted at the cut-planes using the ANSYS post-processing software, CFD Post [3]. Area-averaged pressure and velocity were directly calculated in the software, while the Reynolds numbers were calculated manually from values extracted in the software. The values found for these three variables are presented in the graphs on the next pages.
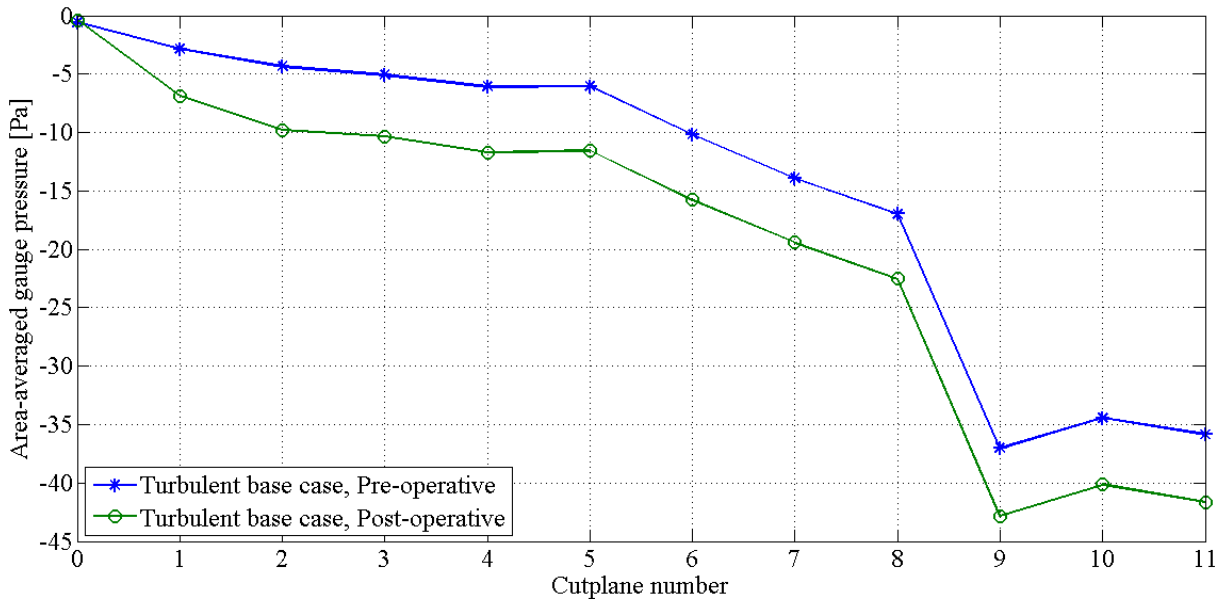
Figure 4.3: Area-averaged gauge pressure plotted at cross-sections marked in Figure 4.1 and Figure 4.2 for turbulent flow in the base case
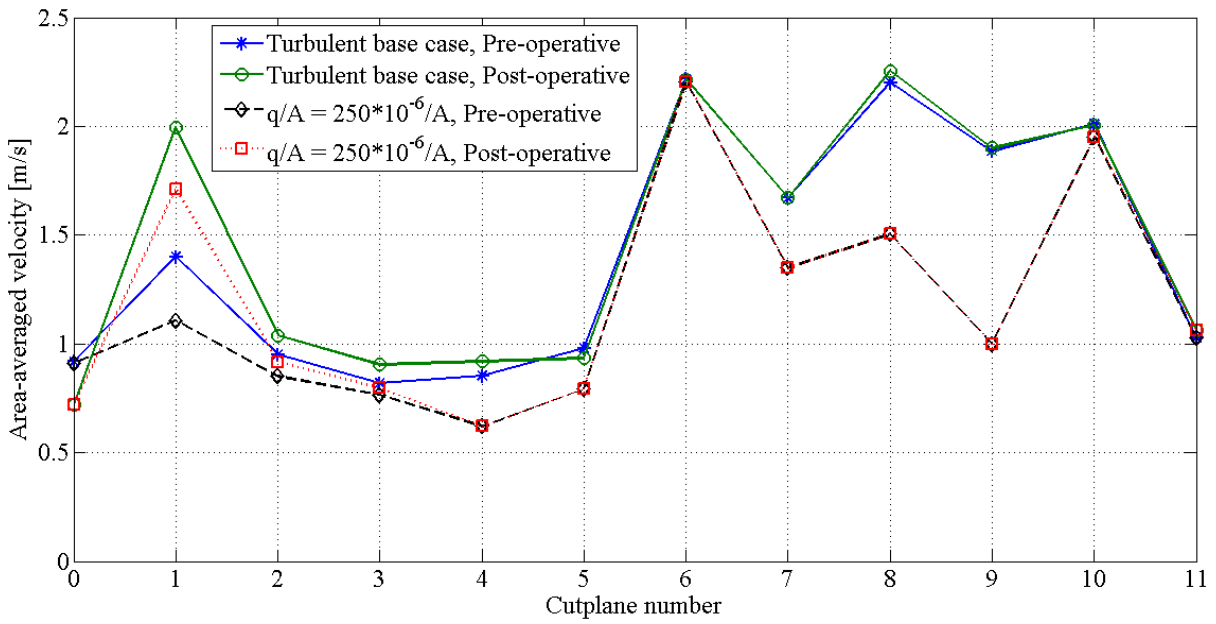
Figure 4.4: Area-averaged velocity plotted at cross-sections marked in Figure 4.1 and Figure 4.2 for turbulent flow in the base case, as well as plots with theoretical values for q/A [m³/s / m²] for pre- and post-operative geometries
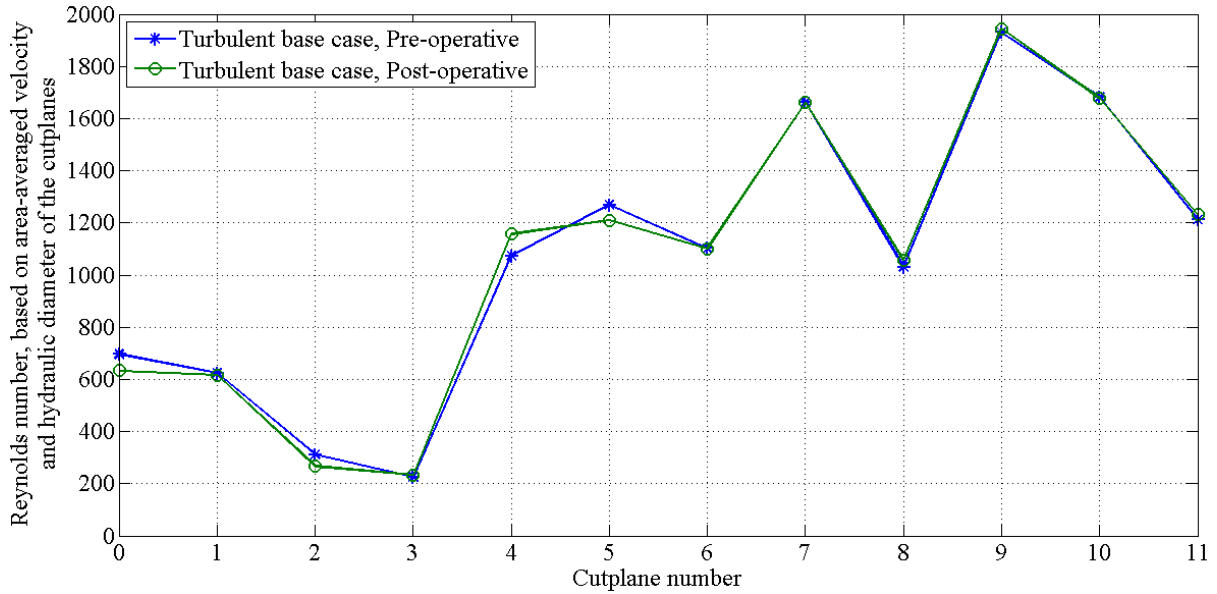
Figure 4.5: Reynolds number for the base case at different cut-planes defined in Figure 4.1 and Figure 4.2 based on area-averaged velocity and hydraulic diameter of the cut-plane

As mentioned in Ch. 3.1, the patient lies in different positions in the CT images from before and after surgery. In the post-operative CT scans, the patient's head was tilted back more, while the neck was straighter in the pre-operative CT scans. This leads to a difference in the inlets, as can be seen in Figure 4.1 and Figure 4.2, and it is unknown what effect this will have on the flow. Due to a slight repositioning (3 mm) of the post-operative nasal cavity during the merging of the upper post-operative and lower pre-operative geometries (see Ch. 3.1), the cut-planes are not positioned identically in the pre- and post-operative nasal cavities since the defined cut-planes have a constant position in the coordinate system. It can be seen that e.g. the shape of the cross-sections deviates somewhat. The outlet planes numbered 11 are also a little different in area, because the cut angle at the trachea was somewhat different and the extension then had different angles (cf. Ch. 3.1).

For the area-averaged pressure depicted in Figure 4.3, the largest difference between the pre- and post-operative results is from the inlets to cut-plane no. 1. This is where the operation has changed the geometry the most, by straightening the septum, and we see that it is the post-operative case that demonstrates the largest pressure drop. From cut-plane no. 2 and down, the two area-averaged pressure curves follow similar paths. For both geometries, there are two locations that have a prominent pressure drop. A smaller pressure drop is seen from cut-plane no. 5 to 6, near the uvula where there is a narrowing in the geometry, and a much larger pressure drop is observed from cut-plane no. 8 to 9, which is near the epiglottis that is creating a jet.

In Figure 4.4, it is observed that there are large variations in area-averaged velocity throughout the geometry. There is also poor correlation in some locations between the theoretical velocity of 250 ml/s divided by the area in each cut-plane and the area-averaged velocity. It is found that the volumetric flow rate is not constant throughout the entire geometry either, which could indicate non-converged results. However, the trends are similar, as the post-operative velocities are larger than the pre-operative ones in the nasal cavities and the pre- and post-operative velocities become more similar in the lower parts of the geometries, as it should since the geometries are identical in the lower parts. From cut-plane no. 5 and down, the area in each defined cut-plane switches between larger and smaller for each plane, giving the pattern seen in the figures for the area-averaged velocity (Figure 4.4) and Reynolds number (Figure 4.5). The area-averaged velocity and Reynolds number vary opposite of each other, meaning that when the velocity rises, the Reynolds number goes down, and vice versa. This is caused by the varying cross-sectional areas. The difference between the area-averaged velocity for the pre- and post-operative geometries is only present before cut-plane no. 5, after which the two geometries are identical. The difference is especially prominent from the inlet to cut-plane 1, corresponding to where the operation has taken place.
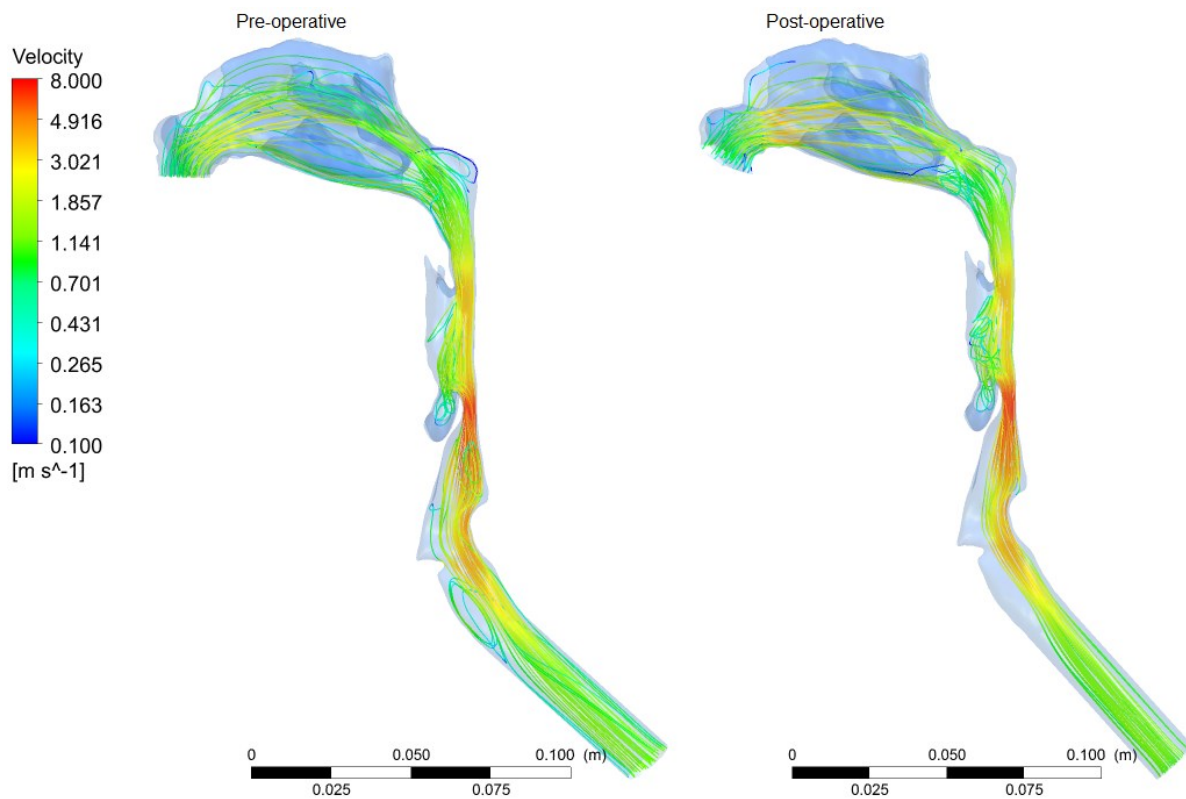
Figure 4.6: Velocity streamlines generated with 50 evenly distributed release points in the two nostrils, seen from the left, magnitude in logarithmic scale; comparison of flows in pre- and post-operative geometries

31
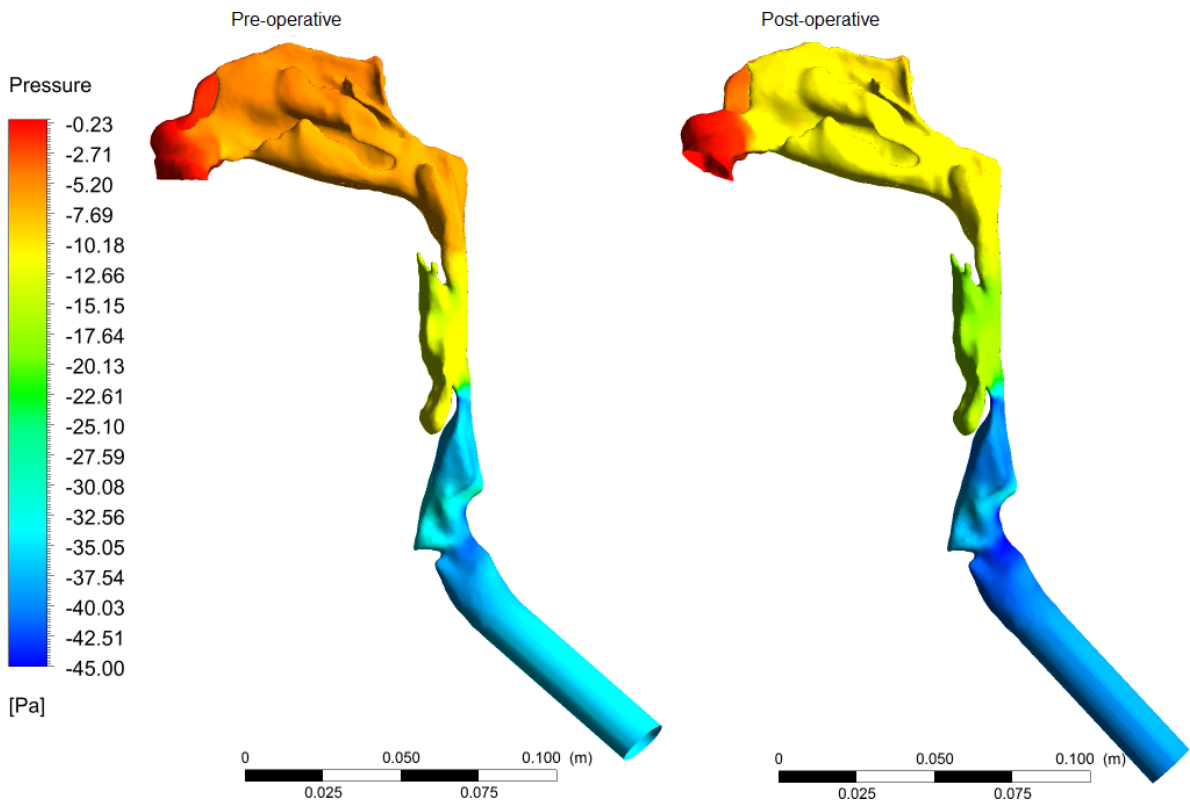
Figure 4.7: Wall pressure, seen from the left; comparison of flows in pre- and post-op. geometries
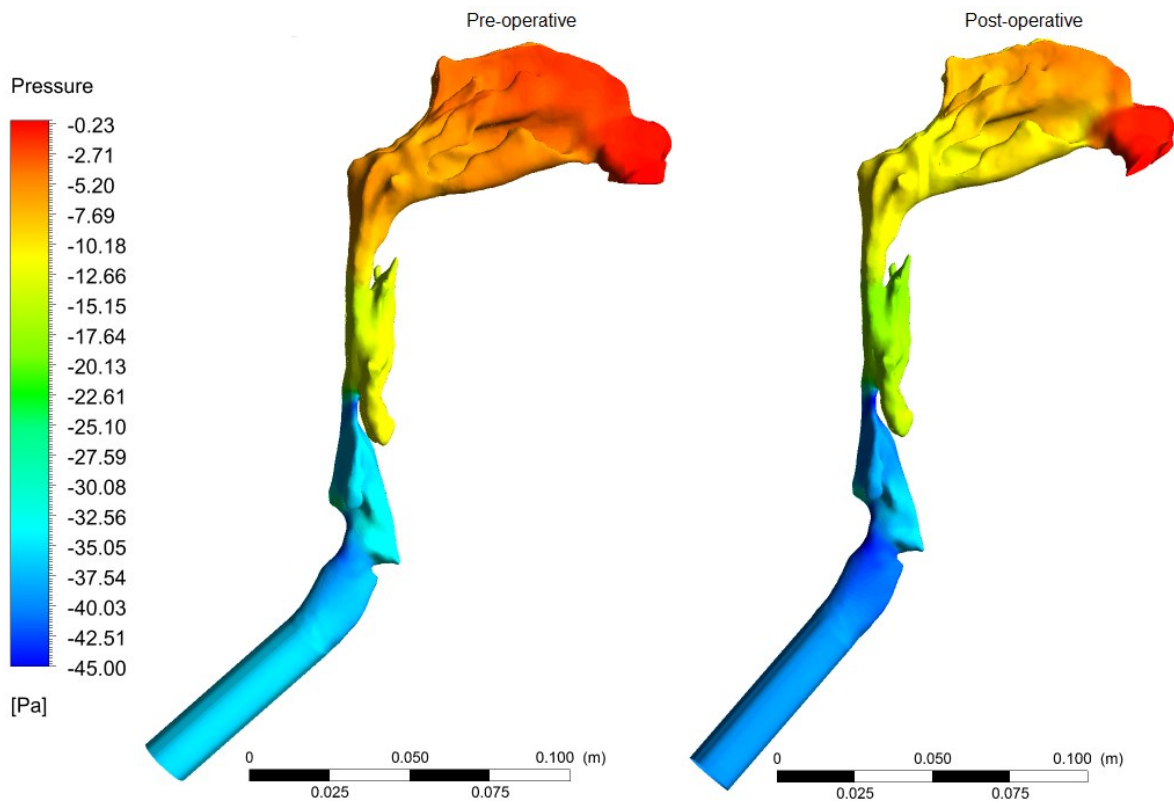
Figure 4.8: Wall pressure, seen from the right; comparison of flows in pre- and post-op. geometries
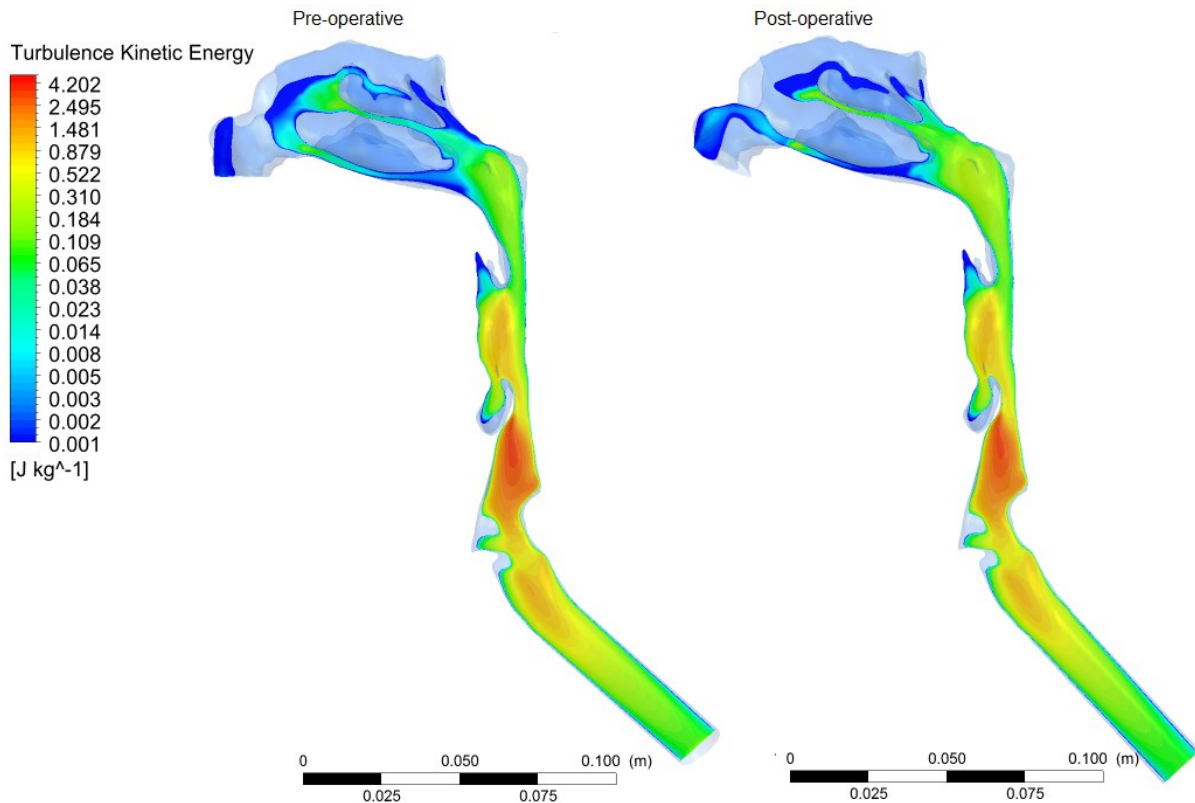
Figure 4.9: Turbulence kinetic energy in a vertical plane cut through the left nasal cavity, magnitude in logarithmic scale; comparison of flows in pre- and post-op. geometries

The velocity streamlines in Figure 4.6 indicate that there are some differences in the paths of the streamlines, but the magnitudes of velocity in the two cases are very similar. The biggest differences are observed in the nasal cavity, which is where the operation took place, behind the oral cavity, right after the epiglottis and at the beginning of the extension where the esophagus starts. In the post-operative situation, the velocity seems to have more swirl in the oropharynx behind the oral cavity, while the rest of the locations mentioned have less swirl.

The wall pressure distribution is depicted in Figure 4.7 and Figure 4.8, seen from the left and right side respectively. It is easily observed that the two situations have the same type of division, with larger pressure drops right after the inlet, at the uvula and at the epiglottis. The major difference between the pre- and post-operative results seems to be that the pressure drop right after the inlet is significantly larger after surgery, as was observed in Figure 4.3 as well. This correspond to the larger velocity at cut-plane 1 for the post-operative geometry compared to the pre-operative geometry, and higher velocity gives higher pressure drop. The trend further down is the same for the two geometries, which is to be expected since the geometries are identical from the nasopharynx and down.

The turbulent kinetic energy can be seen in Figure 4.9. There are some minor differences in the results before and after surgery in the nasal cavity. However, from the nasopharynx and down, the pre- and post-operative results are virtually identical. The observed difference could just be artificial, as the vertical planes are located slightly different in the nasal cavity due to different positioning in the CT scans. It is believed that the small difference in TKE in the beginning of the geometry is insignificant to the results further downstream since the TKE becomes identical in the nasopharynx.
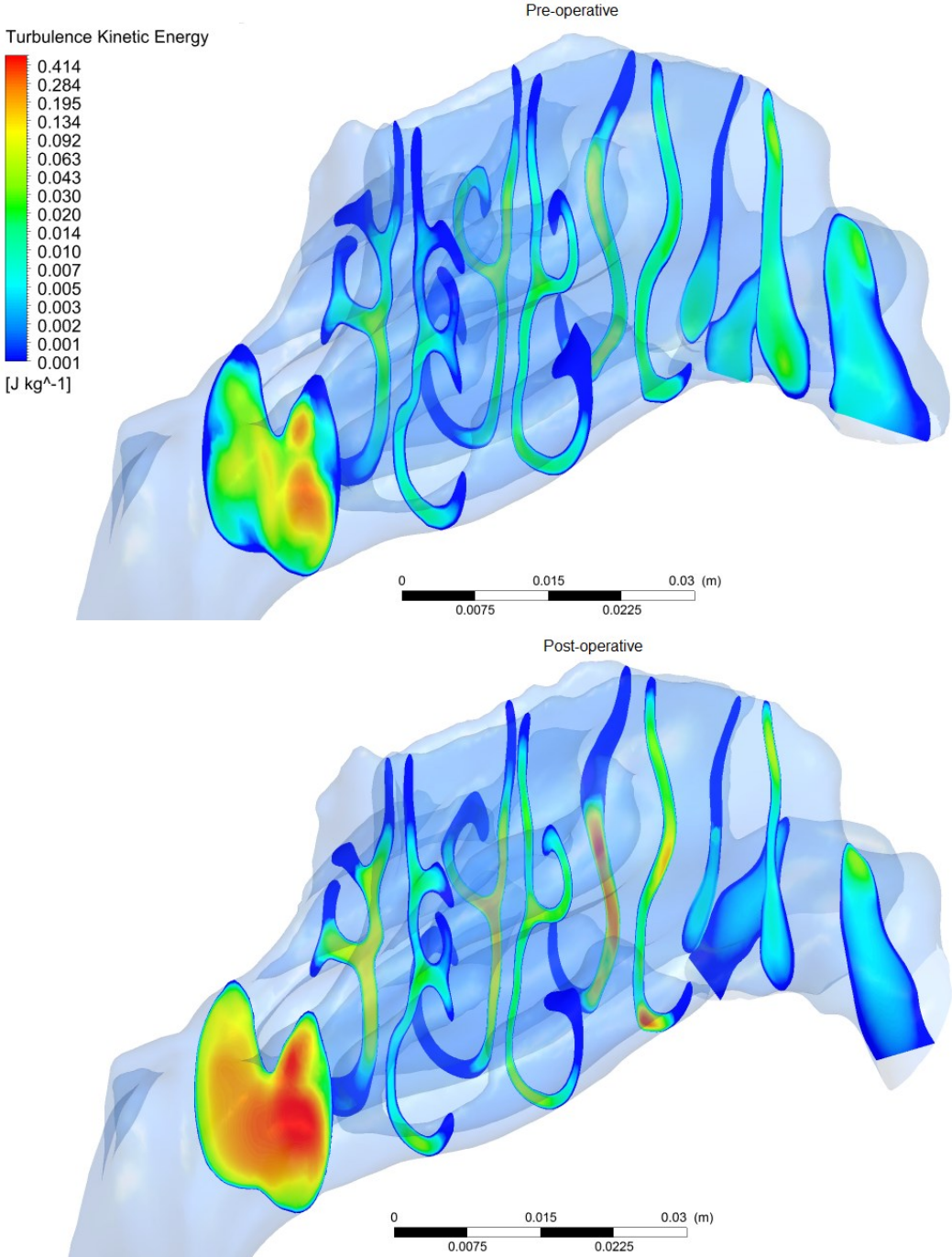
Figure 4.10: Turbulence kinetic energy in vertical planes through the nasal cavity, magnitude in logarithmic scale; comparison of flows in pre- and post-operative geometry
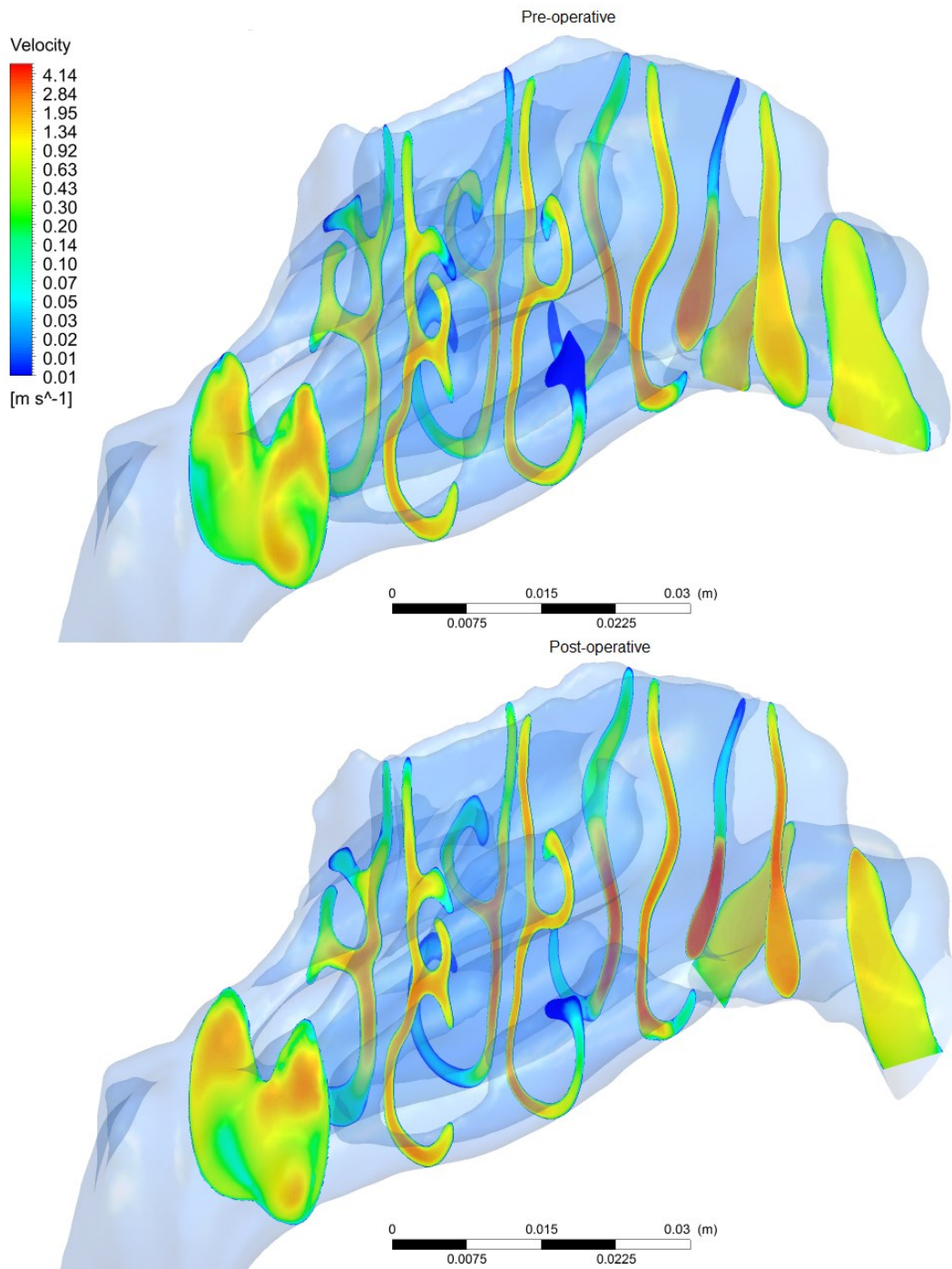
Figure 4.11: Velocity modulus contours in vertical planes through the nasal cavity, magnitude in logarithmic scale; comparison of flows in pre- and post-operative geometry

As can be seen in the figures above, both the turbulence kinetic energy (Figure 4.10) and the velocity modulus (Figure 4.11) in the nasal cavity show the same trends, but the values are higher for the post-operative geometry than the pre-operative one. This is consistent with the other results in this chapter.

5 Comparison with experimental data

To have some validation of the CFD results, they must be compared to experimental data. One type of measurement that is performed in hospitals is rhinomanometry. Rhinomanometry is conducted by closing one nostril completely while the other nostril is connected to a tube, creating one open nostril where the air can flow freely and be measured. When the patient breathes normally through the open nostril, the pressure is measured at the closed nostril, which is equal to the pressure where the nasal cavities meet. The pressure at the open nostril is also measured, and by subtracting the two pressures, the pressure drop over the nasal cavity is obtained. The volumetric flow rate through the open nostril is measured as well, and a graph showing the relationship between volumetric flow rate and pressure drop from nostril to nasopharynx is produced. A schematic sketch of the process can be seen in Figure 5.1. The process is repeated twice, first for the normal, congested state, and second, after use of a nasal spray to decongest the nose. Both states are presented in rhinomanometry graphs. The rhinomanometry graph for patient no. 12 before surgery is presented in Figure 5.2.
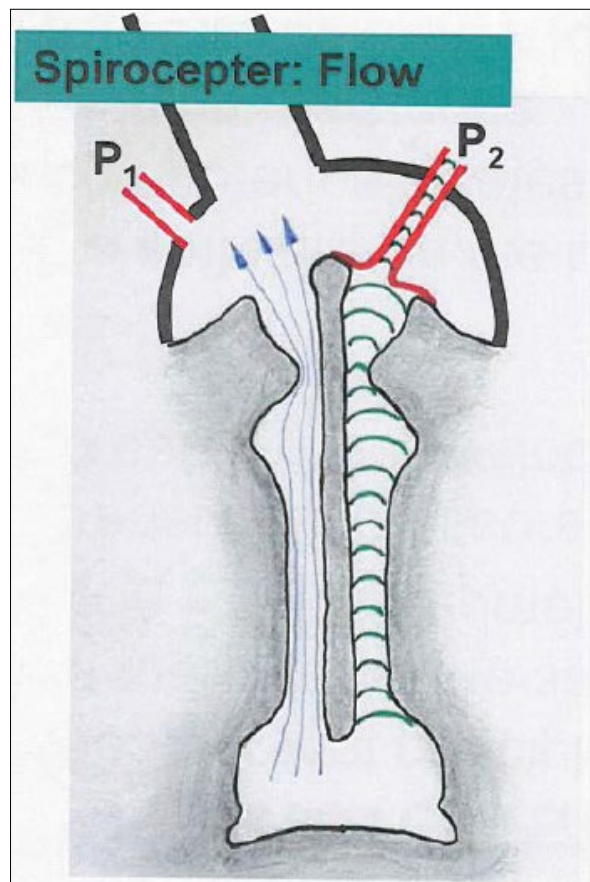
Figure 5.1: Schematic view of nasal cavity from above; principle of rhinomanometry
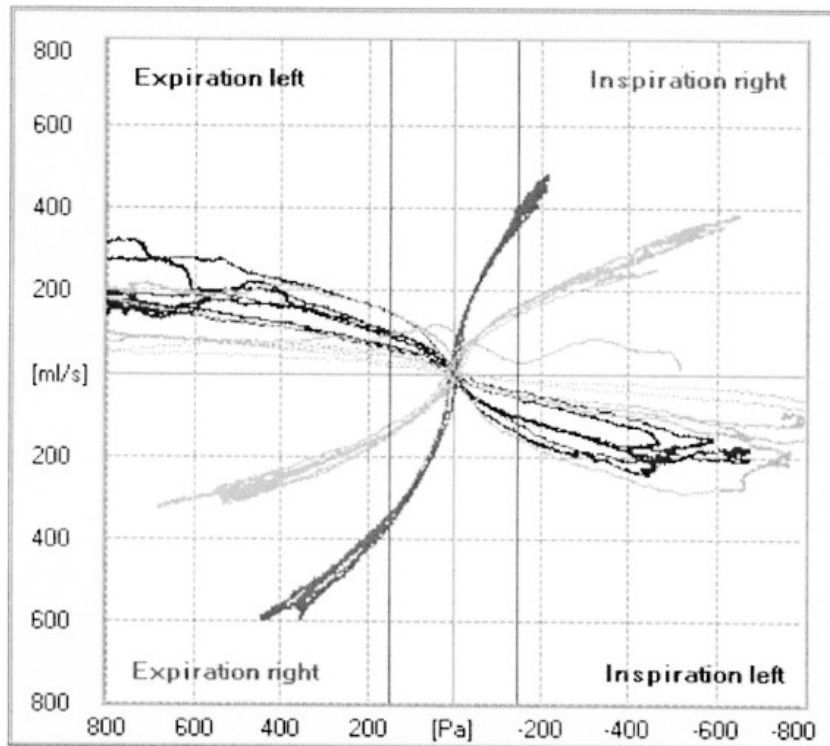
Figure 5.2: Rhinomanometry for patient 12 before surgery; light gray is in congested state, while the darker gray is after decongestion with a nasal spray

The CFD simulations were conducted with the same setup as the pre-operative base case described in subchapter 3.3, except for the boundary conditions. Both the inlet and outlet boundary conditions were velocity conditions determined by using flow rates from the rhinomanometry, multiplied by the area of the left or right nostril or the outlet, depending on which boundary condition was applicable. The inlets are each of the nostrils (cut-plane no. 0, cf. Figure 4.1), while the outlet is the end of the extension from the trachea (cut-plane no. 11, cf. Figure 4.1). Since the base case is based on constant inspiration, we have only considered inspiration for comparison between CFD and rhinomanometry data. The wall boundary conditions of no-slip and zero roughness height were kept as before. The resulting inlet and outlet boundary conditions can be seen in Table 5.1. The areas used are quantified by ANSYS CFD Post [3]. The chosen flow rates correspond to the rhinomanometry data for patient no. 12.

38

Table 5.1: Inlet and outlet boundary conditions for CFD simulations for pre-operative rhinomanometry comparison

Inspiration right			Inspiration left		
Area inlet right [m²]	**Flow rate [ml/s]**	**BC right [m/s]**	**Area inlet left [m²]**	**Flow rate [ml/s]**	**BC left [m/s]**
A=0.0001599	q=100	U=0.62539	A=0.0001137	q=50	U=0.43975
	q=200	U=1.25078		q=100	U=0.87951
	q=300	U=1.87617		q=150	U=1.31926
	q=400	U=2.50156		q=200	U=1.75902
	q=500	U=3.12695		q=250	U=2.19877
Area outlet [m²]	**Flow rate [ml/s]**	**BC out [m/s]**	**Area outlet [m²]**	**Flow rate [ml/s]**	**BC out [m/s]**
A=0.0002433	q=100	U=0.411015	A=0.0002433	q=50	U=0.205508
	q=200	U=0.822030		q=100	U=0.411015
	q=300	U=1.233046		q=150	U=0.616523
	q=400	U=1.644061		q=200	U=0.822030
	q=500	U=2.055076		q=250	U=1.027538

It was assumed that the decongested state would be closer to the CFD model due to the limited ability to capture mucus and soft tissue in CT images. A mean representative curve was created by visual approximation for the decongested state to be able to compare the CFD results with the rhinomanometry data. The CFD simulations were performed, setting a velocity outlet condition matching a velocity inlet condition in one of the nostrils, so the volumetric flow rate was conserved, while the other nostril had a velocity inlet condition of 0. The resulting graph with the CFD results and the mean rhinomanometry data is depicted in Figure 5.3.
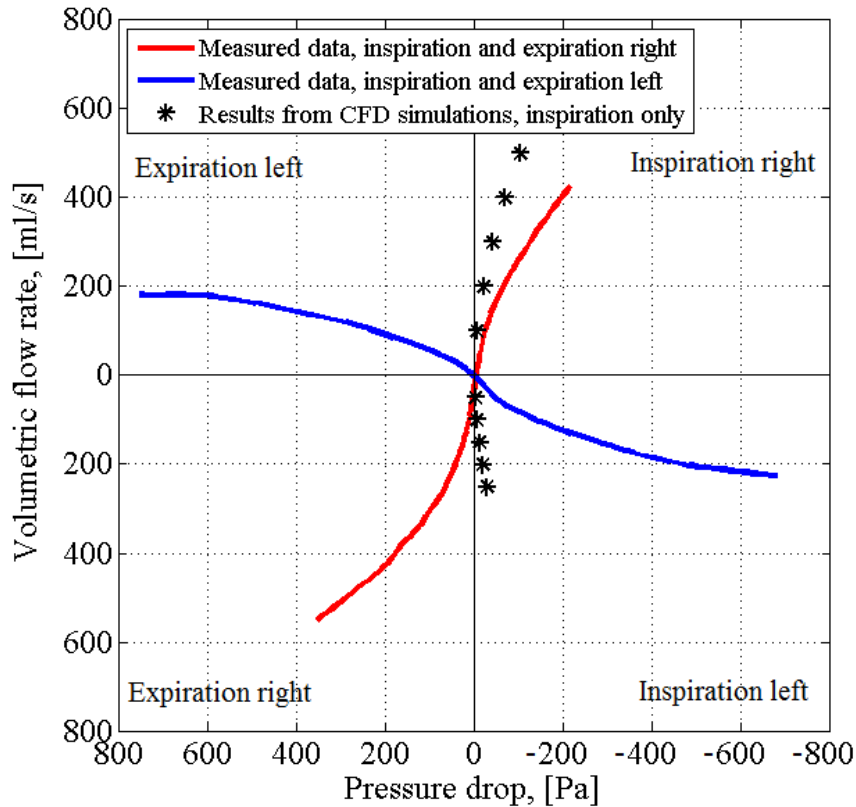
Figure 5.3: Comparison of CFD results and rhinomanometry data for patient 12, pre-operative

It is observed that the experimental data and the CFD results do not correspond very well. The deviation is significant, leading to the suspicion that there is a systematic error in the simulations. It has previously been argued that choice of turbulence model has only minor impact [1], excluding this as a source for the large deviations. It is suspected that discrepancies between the actual airway geometry and the model geometry may cause the error. The geometry is extracted from CT data, where the picture has a black color where there is air, white color where there are bony structures, and the gray in between is soft tissue. Therefore, it is difficult to decide which grayscale is the actual border between tissue and air and this clearly leads to an uncertainty in the actual border between air and solid. In addition, the distance represented by one pixel in the image is relatively large compared to the small gaps that exist, for instance in the narrow nasal cavities, such that an error in pixel interpretation can potentially lead to a significant error. One can also debate how accurate the rhinomanometry data are in the first place in terms of calibration and procedures. Another cause of error could be the simplification of a smooth wall. This is not a realistic situation, with hair and mucus inside the nose causing disturbances, and possibly turbulent effects, in the flow. Furthermore, the accelerating/decelerating flow and transient/unsteady boundary layers may not be well represented by steady-state simulations with constant flow rates.

6 Sensitivity study setup

In order to verify the numerical results, a sensitivity study of the pre-operative geometry is conducted. As mentioned in chapter 5, it is suspected that the geometry or the smooth wall simplification are sources of error. Thus, the geometry dependence and the wall boundary condition must be investigated. Other factors chosen to be investigated are the inlet and outlet boundary conditions, as well as the grid size.

The base case conditions for the pre-operative geometry, as stated in Ch. 3.3, are the following:

- Inlet conditions: Gauge pressure of zero for both left and right inlet. Turbulent intensity of 5% and turbulent viscosity ratio of 10.
- Outlet condition: Volumetric flow rate of 250 ml/s, divided by the area, giving an outlet velocity of 1.0276 m/s (set as an inlet velocity with negative value/direction).
- Wall boundary condition: No slip. Smooth wall, i.e. zero roughness height.

In the specialization project by the undersigned [1], the turbulence boundary conditions were investigated by changing the turbulence intensity to 1% and 10% and compare the results to the base case result where the turbulence intensity was 5%. The conclusion was that the turbulence intensity did not affect the results significantly, within this range.

6.1 Airways geometry

As described in chapter 5, it is suspected that the geometry used is incorrect. A pixel in the CT images is 0.4 mm wide. Thus, wrong interpretation can lead to an error since the scales in the geometry, for instance in the nasal cavity, are very small. To check the dependence on the airways geometry, a new geometry is created by removing one pixel from the airways' flow domain around the entire geometry, making the geometry about 0.4 mm narrower. The new outlet area is then 0.000188 m^2 compared to the base case outlet area of 0.000257 m^2. With a volumetric flow rate at the outlet of 250 ml/s, the new outlet velocity condition is 1.3298 m/s. The narrower geometry was made by Maria R. Jordal and it was meshed by co-supervisor Sverre Gullikstad Johnsen [10] with a size limitation of 1 mm, the same limitation as the base-case mesh.

6.2 Inlet and outlet boundary conditions

As mentioned in chapter 0, it has been observed that for many problems, the outlet condition is the gauge pressure, which is the pressure difference from the atmospheric pressure. For our problem, this proves impractical since the outlet is located inside the human body and it is challenging to measure the pressure at this location. It is chosen to have the base case outlet condition as a velocity corresponding to a volumetric flow rate of 250 ml/s. Having a velocity outlet condition forces the outlet velocity profile to be uniform which in many cases would be unphysical, while a pressure outlet condition lets the outflow profile freely adjust itself to a natural state, with lower flow velocity near the wall and higher near the center. The simulation with the base case showed that the gauge pressure at the outlet is about -36 Pa. To see if the type of outlet condition can affect the results of the simulation, a simulation was run with a pressure outlet condition, and the value was set to -36 Pa. The inlet condition and the rest of the parameters were left unchanged.

To check the inlet condition, another simulation was performed by changing the inlet condition from a total gauge pressure to a velocity condition for each nostril, even though this is expected to give the same unrealistic, uniform inflow profile as mentioned in the previous paragraph. The values chosen are the area-averaged velocity from the base case calculations, namely 0.9444 m/s for the left nostril and 0.9005 m/s for the right nostril. The geometry is still the pre-operative geometry with the base case mesh. The outlet condition is a velocity corresponding to a volumetric flow rate of 250 ml/s, like in the base case simulations. All other parameters were left unchanged as well. When doing simulations with both the inlet and outlet boundary conditions being velocities, the reference point for pressure is not defined. This must be considered when evaluating the results, as the gauge pressure and pressure drop might not be the same.

6.3 Wall boundary conditions

The assumption of a smooth wall is quite unrealistic since the inside of the nose has hair and mucus along the walls. It is therefore of interest to investigate the effect a non-smooth wall boundary condition has on the flow. The sensitivity study was done by adding a roughness height of 0.2 mm [31] to the wall. To be able to add wall roughness in ANSYS [3], enhanced wall treatment must be abandoned and standard wall functions must be implemented instead. The roughness constant was kept as the default value of 0.5, which corresponds to uniform, tightly packed sand-grains in a pipe [7]. The other parameters were also left unchanged.

6.4   Grid size

The sensitivity to grid size needs to be investigated to check if the base case mesh is sufficiently fine. The base case is a mesh with 1.4 million cells, and its generation is described in chapter 3.2. To study the sensitivity to the grid size, two other meshes were generated by co-supervisor Sverre Gullikstad Johnsen [10]. Both meshes have an inflation layer consisting of 5 layers like the base case mesh does, and the other settings were the same, except for the size limitations. A medium size mesh was made with a size limitation of 0.8 mm, which resulted in a mesh with 6.8 million cells, and a fine mesh was generated by setting the size limitation to 0.5 mm, resulting in a mesh with 10.1 million cells. A coarser mesh could have been included as well, to have more validation of the grid size, but this was discarded for this thesis.

7 Results of sensitivity study

7.1 Airways geometry

The sensitivity to airways geometry was investigated as described in chapter 6.1. The simulations in the narrower geometry diverged, so a new, finer mesh was made by Sverre G. Johnsen [10] consisting of 8.9 million cells. The residuals for the continuity, k, ε, and x-, y- and z-velocities for this mesh started at about 1 and settled satisfyingly at values between 10^{-7} and 10^{-10}. The mass was conserved from the inlet to the outlet, and the pressure and velocity fields stabilized. Comparisons of results from the base case geometry and the narrower geometry for different variables are depicted below and on the next pages.
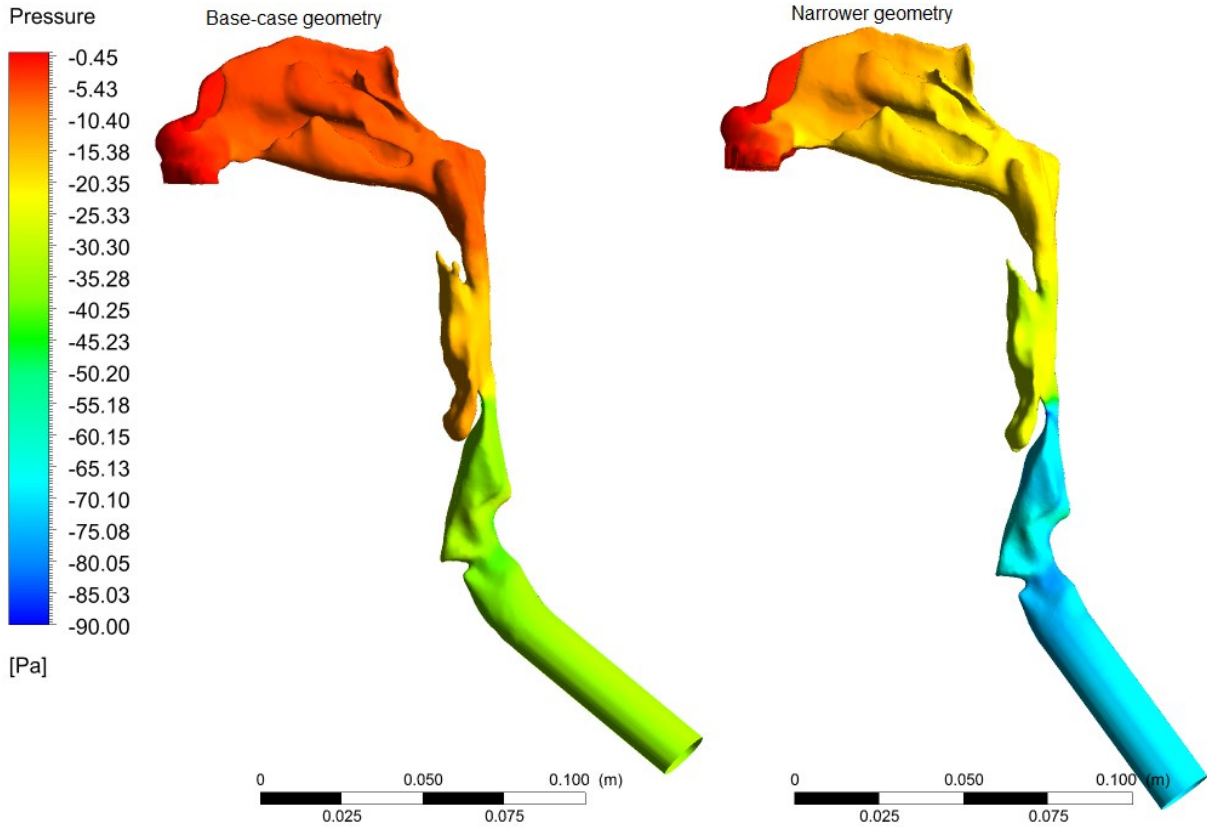
Figure 7.1: Wall pressure, seen from the left; comparison of flows in the pre-operative base-case geometry and a narrower geometry
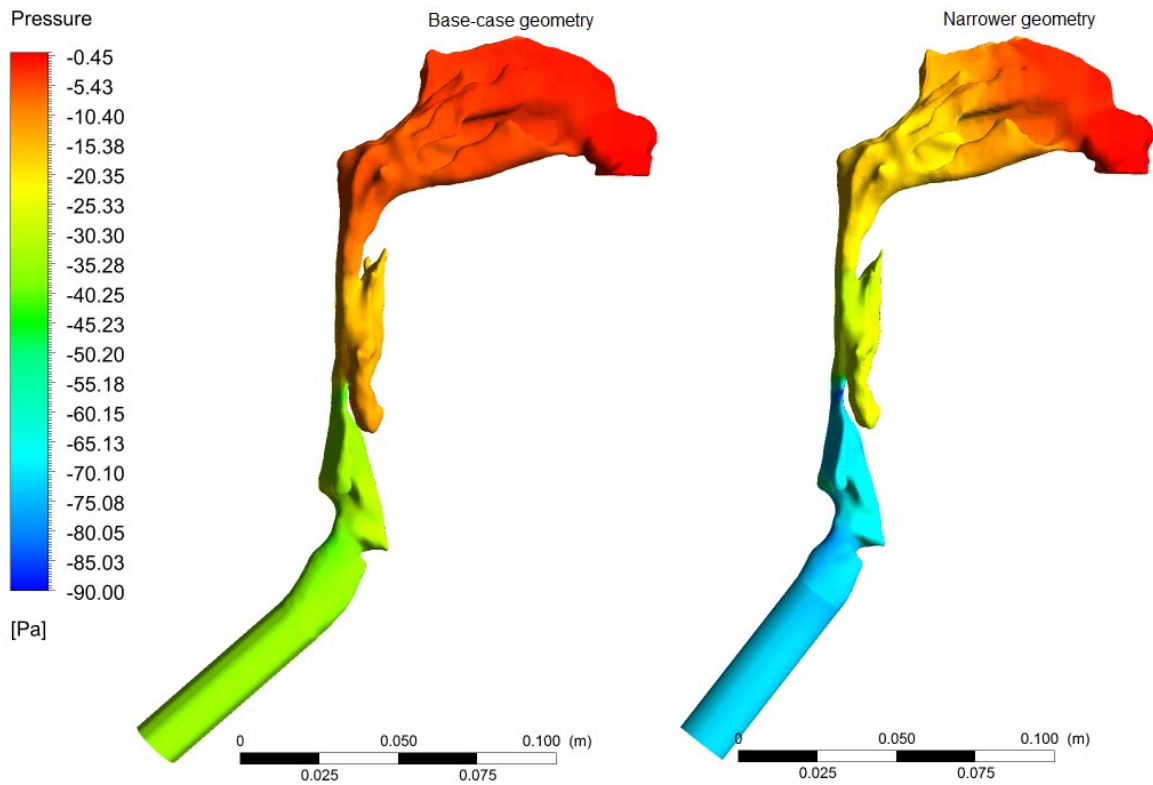
Figure 7.2: Wall pressure, seen from the right; comparison of flows in the pre-operative base-case geometry and a narrower geometry

Figure 7.3: Turbulence kinetic energy in a vertical plane cut through the left nasal cavity, in logarithmic scale; comparison of flows in the pre-operative base-case geometry and a narrower geometry

Figure 7.4: Velocity streamlines generated with 50 evenly distributed release points in the two nostrils, seen from the left, magnitude in logarithmic scale; comparison of flows in the pre-operative base-case geometry and a narrower geometry

The wall pressure in Figure 7.1 and Figure 7.2 show a significant difference. With a narrower geometry, the pressure drop has about doubled at the outlet, while in the rest of the geometry, the pressure drop has more than doubled. The largest difference seems to be from the inlets to cut-plane no. 1, where the narrower geometry shows a much larger pressure drop than the base case. The two geometries show the same sectioning in pressure drop right after the inlet, at the uvula and at the epiglottis. The turbulence kinetic energy in Figure 7.3 is quite similar for the two geometries, with the narrower geometry having a slightly higher value for the TKE throughout most of the geometry. This can especially be seen after the epiglottis, where the TKE is at its highest. The velocity streamlines in Figure 7.4 also have higher magnitudes throughout the entire geometry and especially around the epiglottis. The paths of the streamlines are quite similar, but have some differences in the narrow parts of the geometry. The oropharynx and nasopharynx show much more swirl for the narrower geometry, which could be an important factor in OSAS. Close-up figures of the turbulence kinetic energy and velocity modulus in the nasal cavities are depicted on the next pages and they confirm these observations.

Figure 7.5: Turbulence kinetic energy in vertical planes through the nasal cavities, magnitude in logarithmic scale; comparison of flows in the pre-operative base case geometry and a narrower geometry
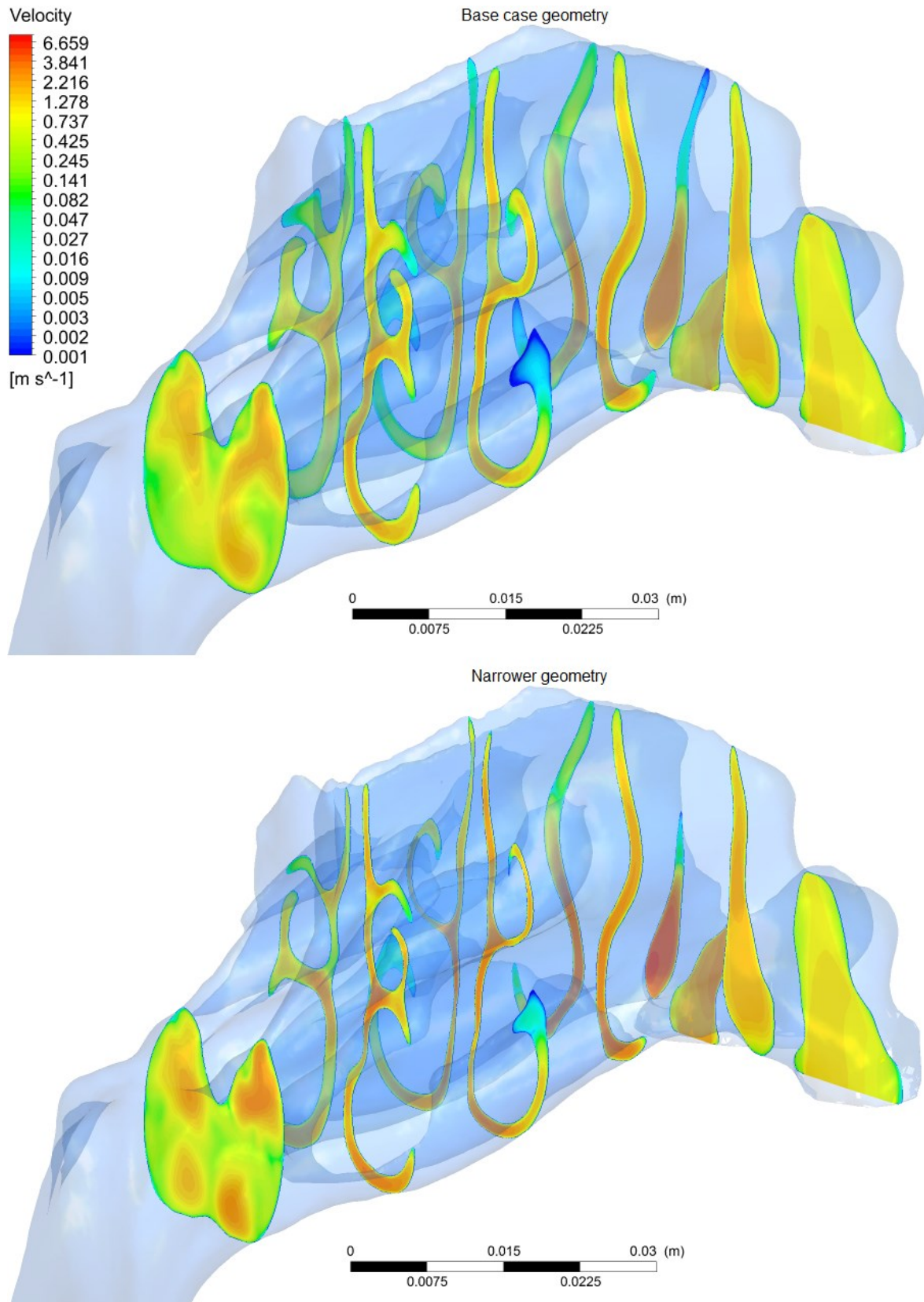
Figure 7.6: Velocity modulus in vertical planes through the nasal cavities, magnitude in logarithmic scale; comparison of flows in the pre-operative base case geometry and a narrower geometry

To quantify the differences in the pressure and velocity, graphs comparing the results from the two geometries were produced for the area-averaged pressure and area-averaged velocity values at the defined cross-sections from Figure 4.1.
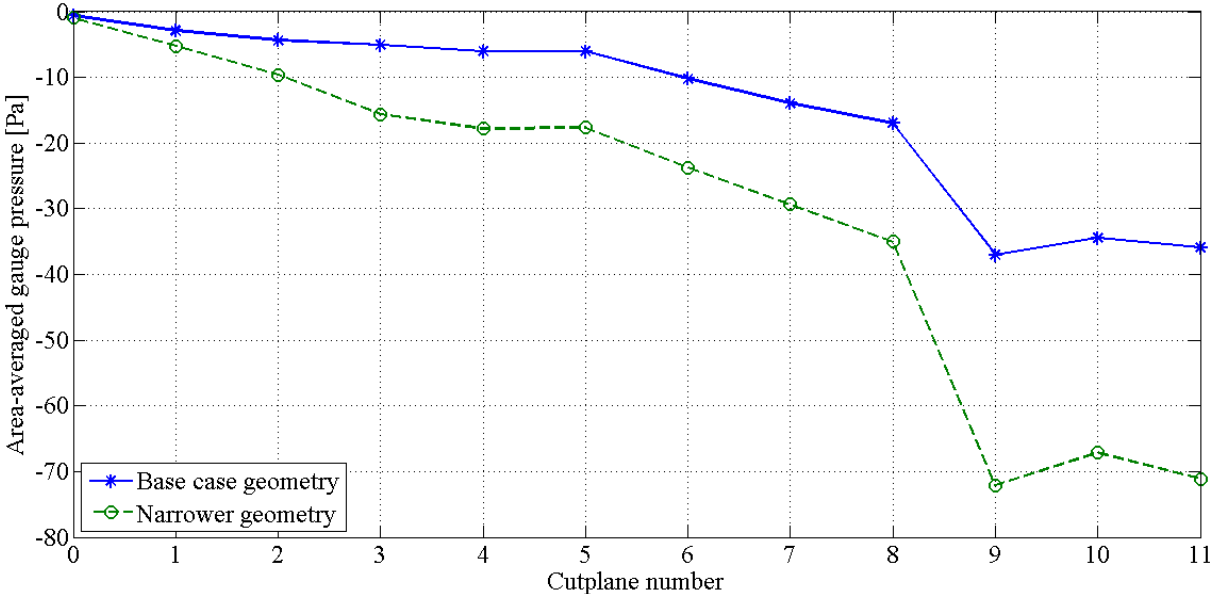
Figure 7.7: Area-averaged gauge pressure plotted at cross-sections marked in Fig. 4.1 for the base case geometry results and results for a narrower geometry
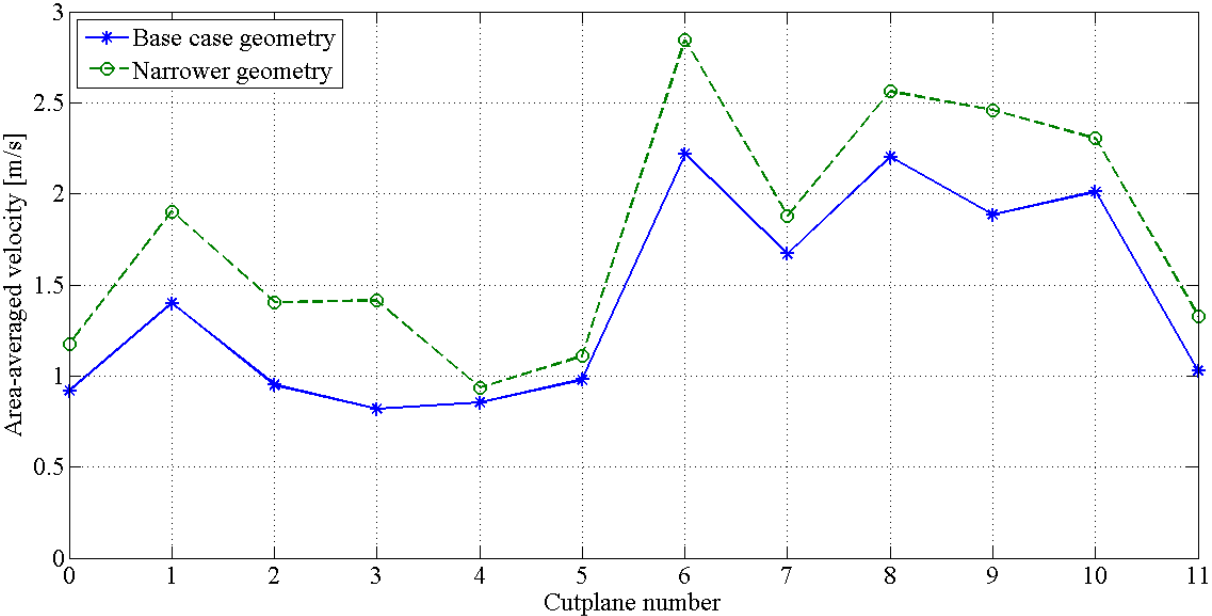
Figure 7.8: Area-averaged velocity plotted at cross-sections marked in Fig. 4.1 for the base case geometry results and results for a narrower geometry

50

The area-averaged gauge pressure in Figure 7.7 confirms the statement that the pressure drop in the narrower geometry is about doubled at the outlet and more than doubled throughout the geometry. The area-averaged velocity in Figure 7.8 confirms that the velocity is higher in the narrower geometry than the base case geometry for all locations.

7.2 Inlet and outlet boundary conditions

An investigation of the dependence on the outlet condition was performed as described in chapter 6.2. The results are shown in the figures below and on the next pages.

Figure 7.9: Wall pressure, seen from the left; comparison of flows in the pre-operative base-case geometry with velocity outlet condition and results with a pressure outlet condition

Figure 7.10: Wall pressure, seen from the right; comparison of flows in the pre-operative base-case geometry with velocity outlet condition and results with a pressure outlet condition
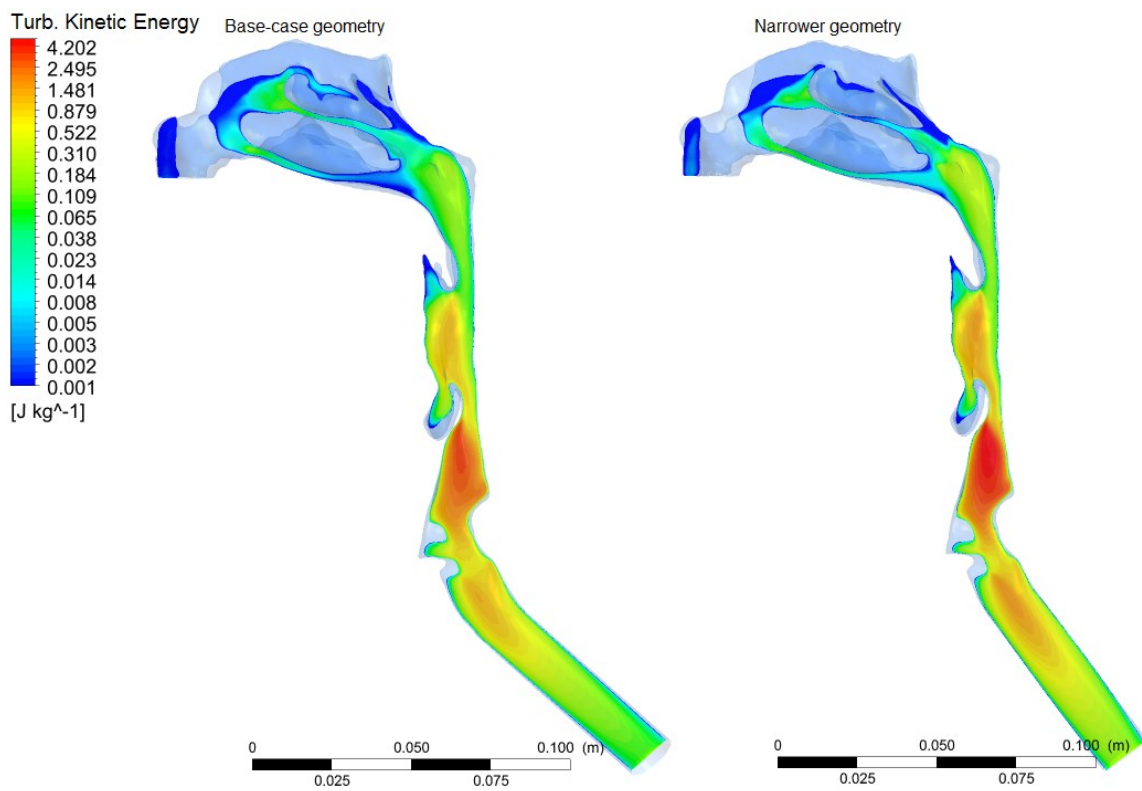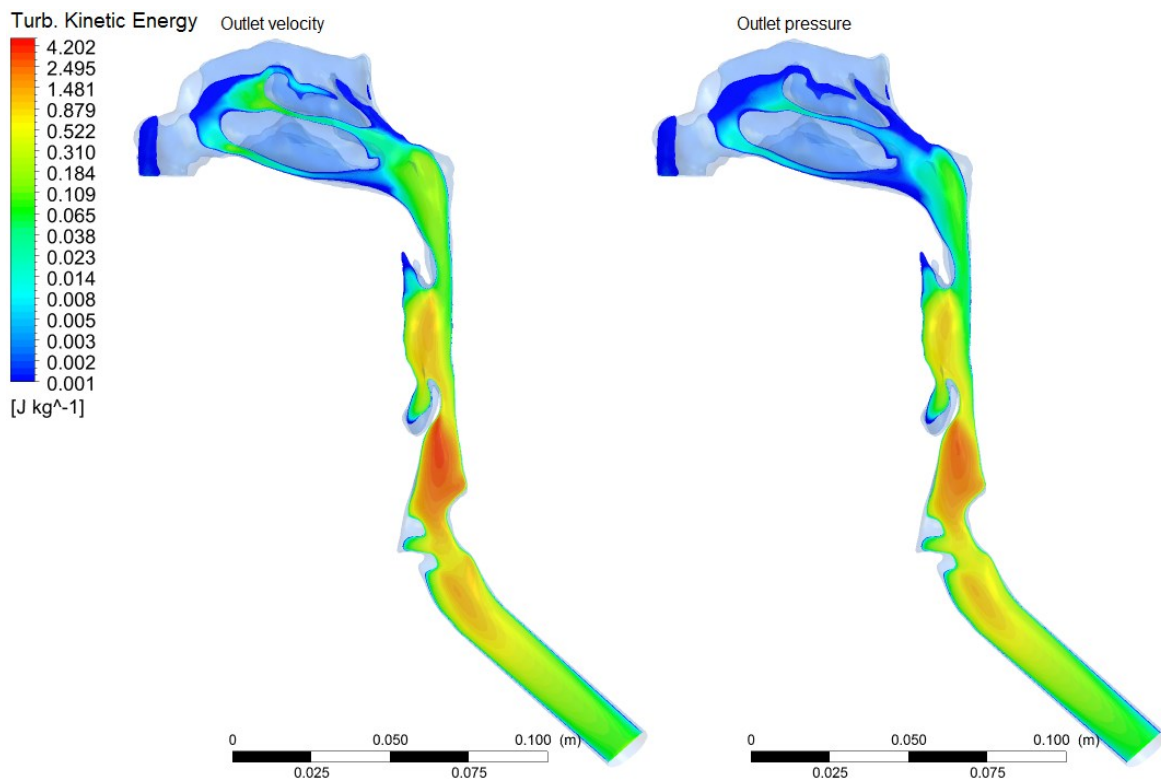

Figure 7.11: Turbulence kinetic energy in a vertical plane cut through the left nasal cavity, in logarithmic scale; com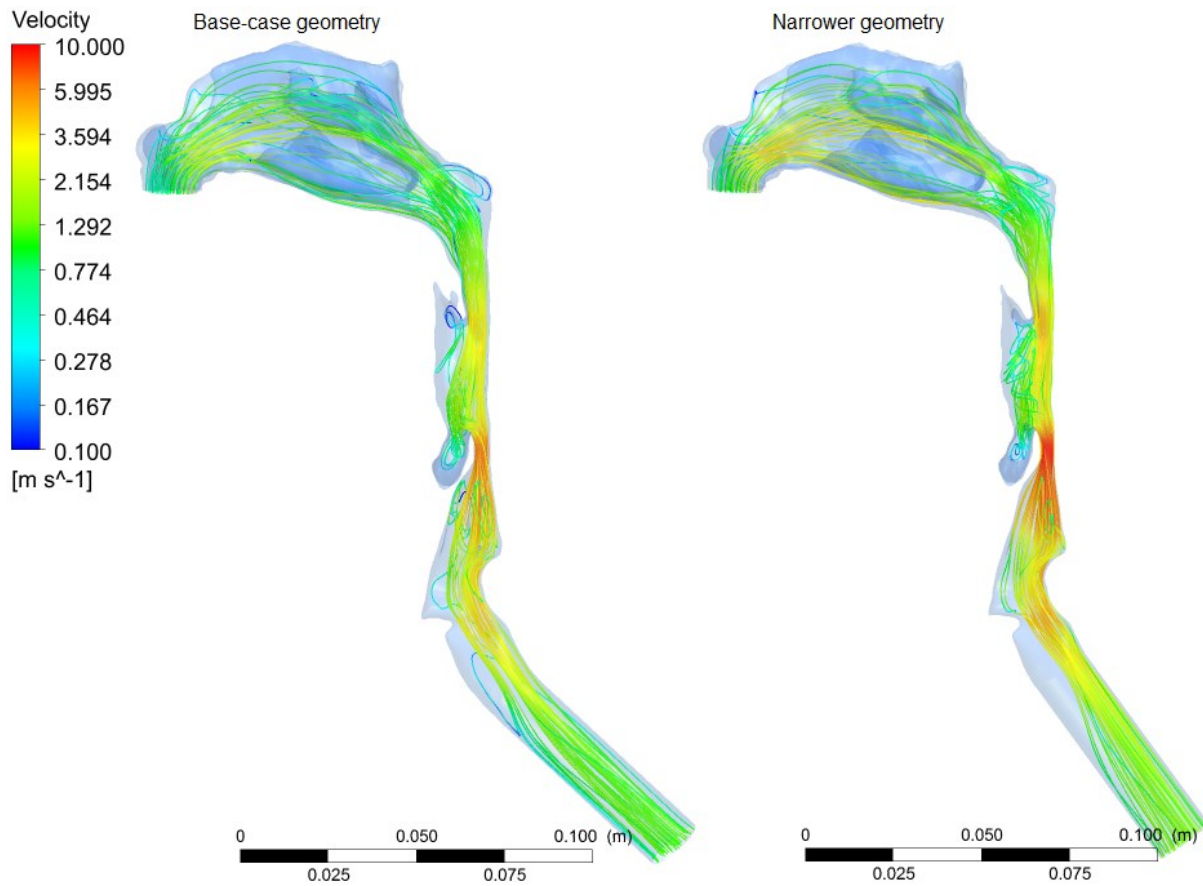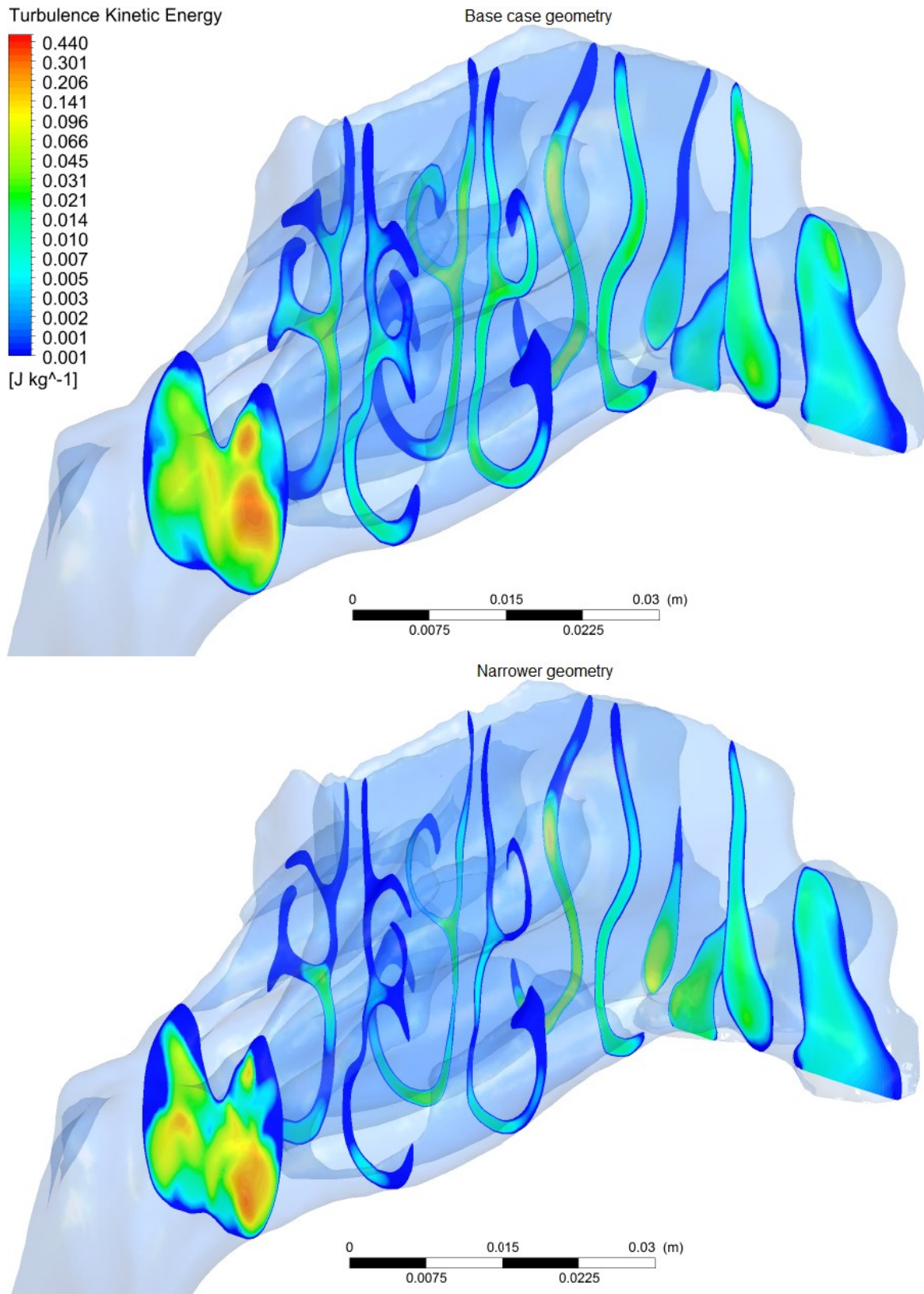parison of flows in the pre-operative base-case geometry with velocity outlet condition and results with a pressure outlet condition
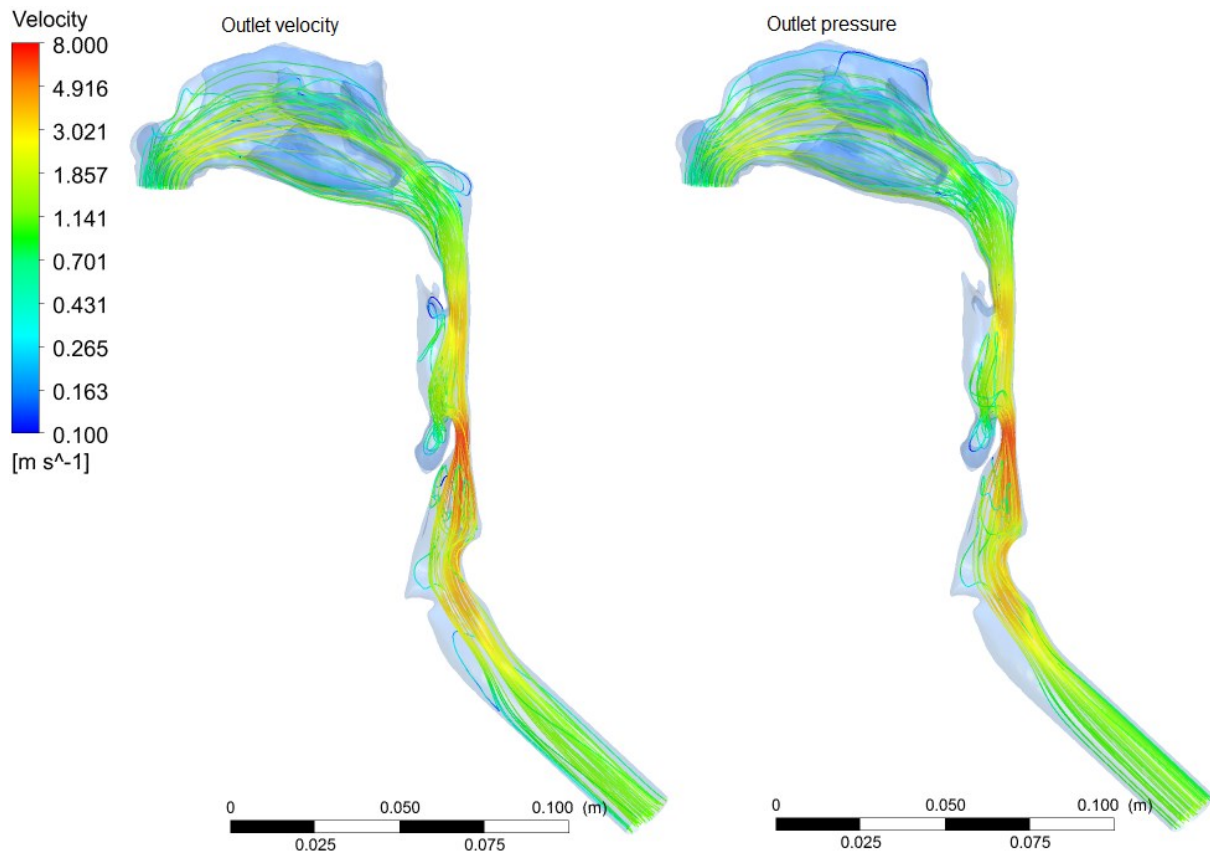
Figure 7.12: Velocity streamlines generated with 50 evenly distributed release points in the two nostrils, seen from the left, magnitude in logarithmic scale; comparison of flows in the pre-operative base-case geometry with velocity outlet condition and results with a pressure outlet condition

The wall pressure seen in Figure 7.9 and Figure 7.10 are identical, indicating that the choice of outlet condition does not affect this variable. The turbulence kinetic energy in Figure 7.11 is slightly different in the nasal cavity and in the nasopharynx when comparing the two outlet conditions. There is also some difference around the epiglottis, where the pressure outlet condition displays a smaller value for the TKE than the velocity outlet condition. The velocities in Figure 7.12 show the same magnitude for the two outlet conditions, while the paths differ a little. However, these path differences are minor and the overall picture displays the same trend. One can therefore conclude that the type of outlet condition chosen does not affect the flow significantly.

A quantification of these results can be seen in the graphs on the next page. The area-averaged pressure shows some difference from cut-plane no. 6, while it is highly similar before this point. The area-averaged velocity shows a slight deviation throughout the entire plot. The estimated error in the outlet pressure (relative to the base-case value) is ±0.1 Pa.

Figure 7.13: Area-averaged gauge pressure plotted at cross-sections marked in Fig. 4.1 for the base case results with velocity outlet and comparative results with pressure outlet

Figure 7.14: Area-averaged velocity plotted at cross-sections marked in Fig. 4.1 for the base case results with velocity outlet and comparative results with pressure outlet

The sensitivity to type of inlet condition was also looked into, with the approach described in chapter 6.2. Again, the residuals for the continuity, k, ε, and x-, y- and z-velocities converged satisfactory, to values between 10^{-5} and 10^{-8}, starting from about 1, the mass was conserved, and the velocity and pressure profiles stabilized.

54
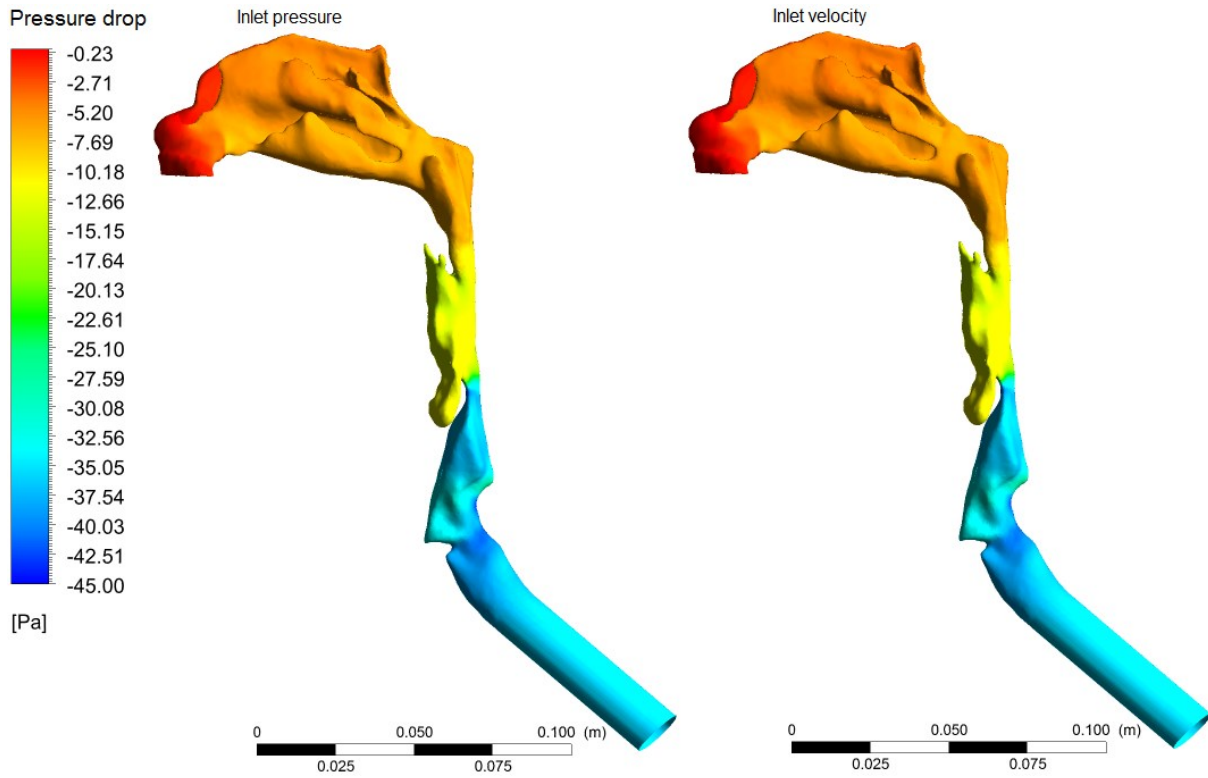
Figure 7.15: Wall pressure drop, seen from the left; comparison of flows in the pre-operative base-case geometry with pressure inlet condition and results with a velocity inlet condition
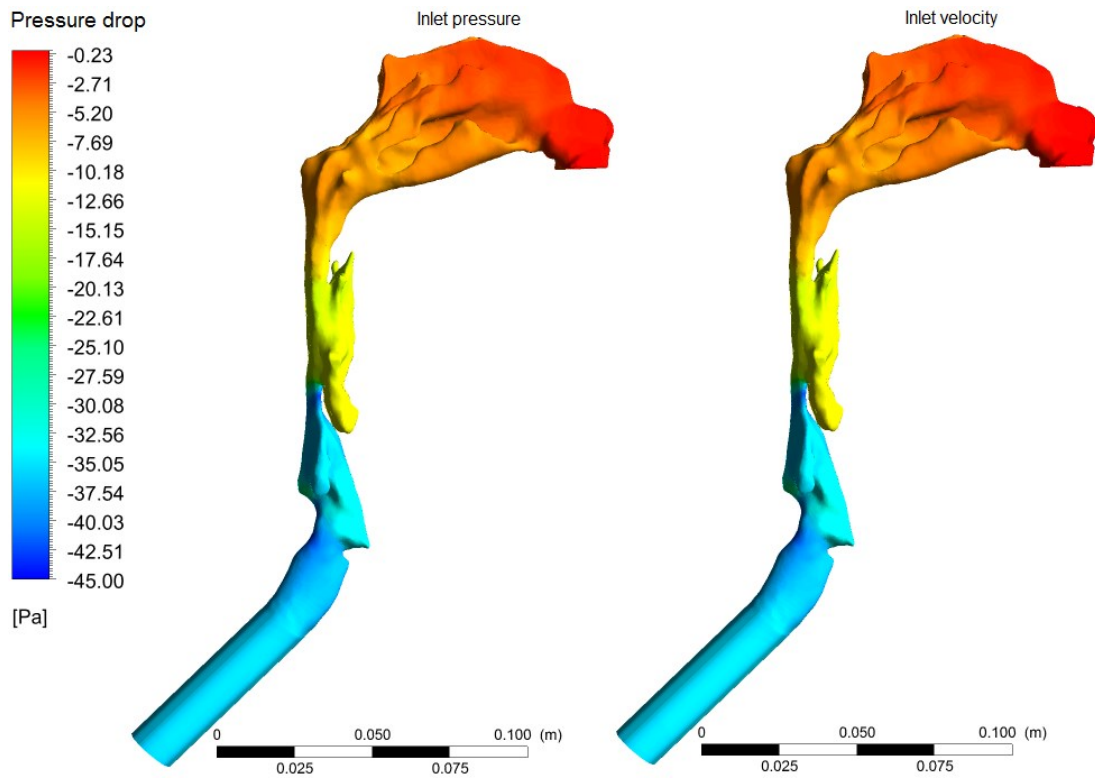
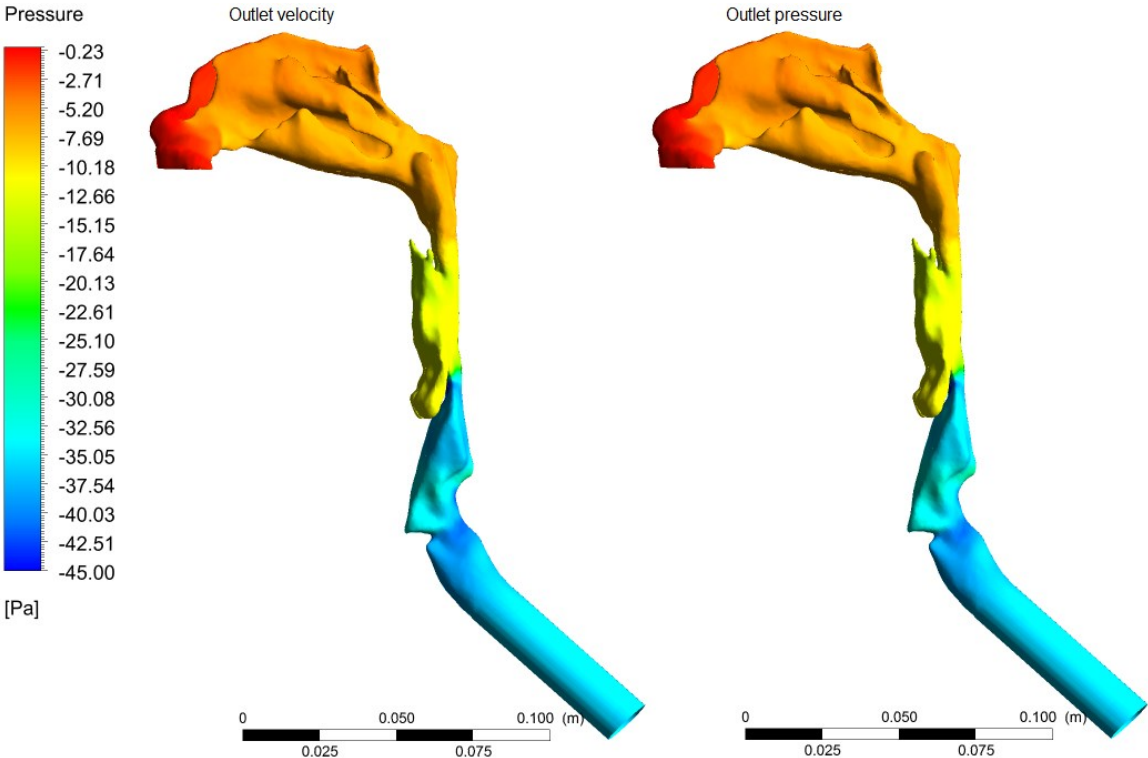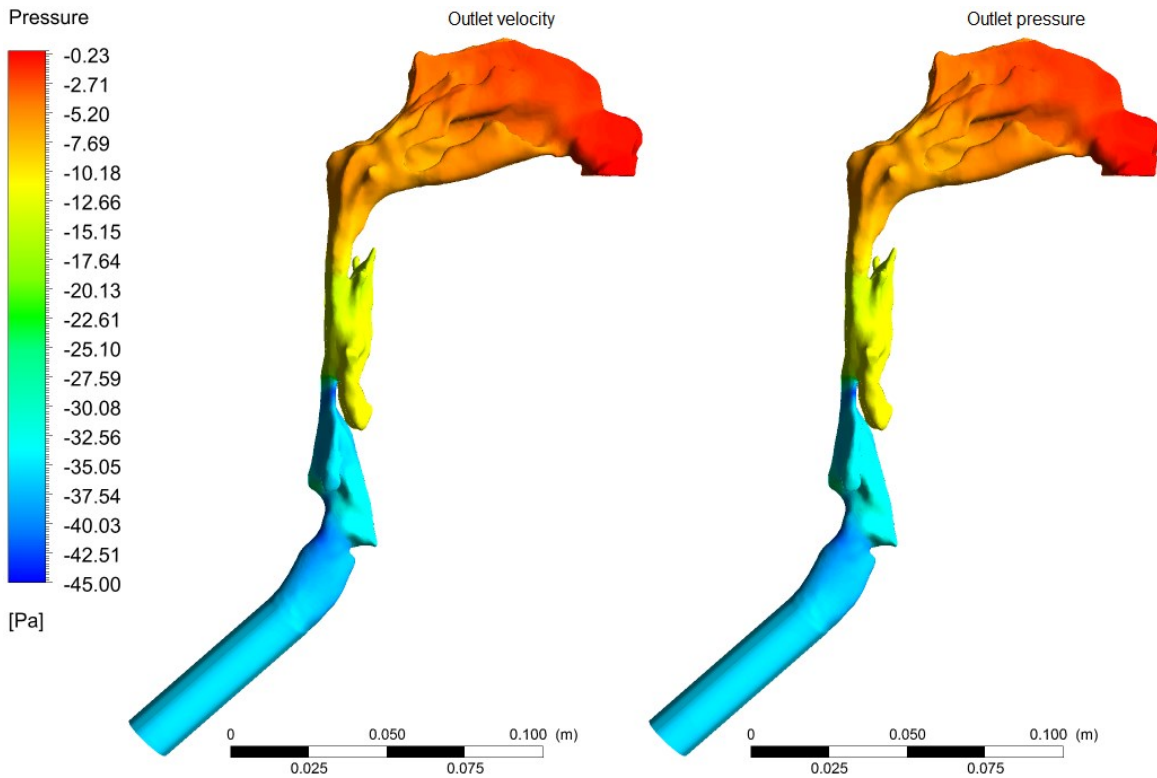*Figure 7.16: Wall pressure drop, seen from the right; comparison of flows in the pre-operative base-case geometry with pressure inlet condition and results with a velocity inlet condition*
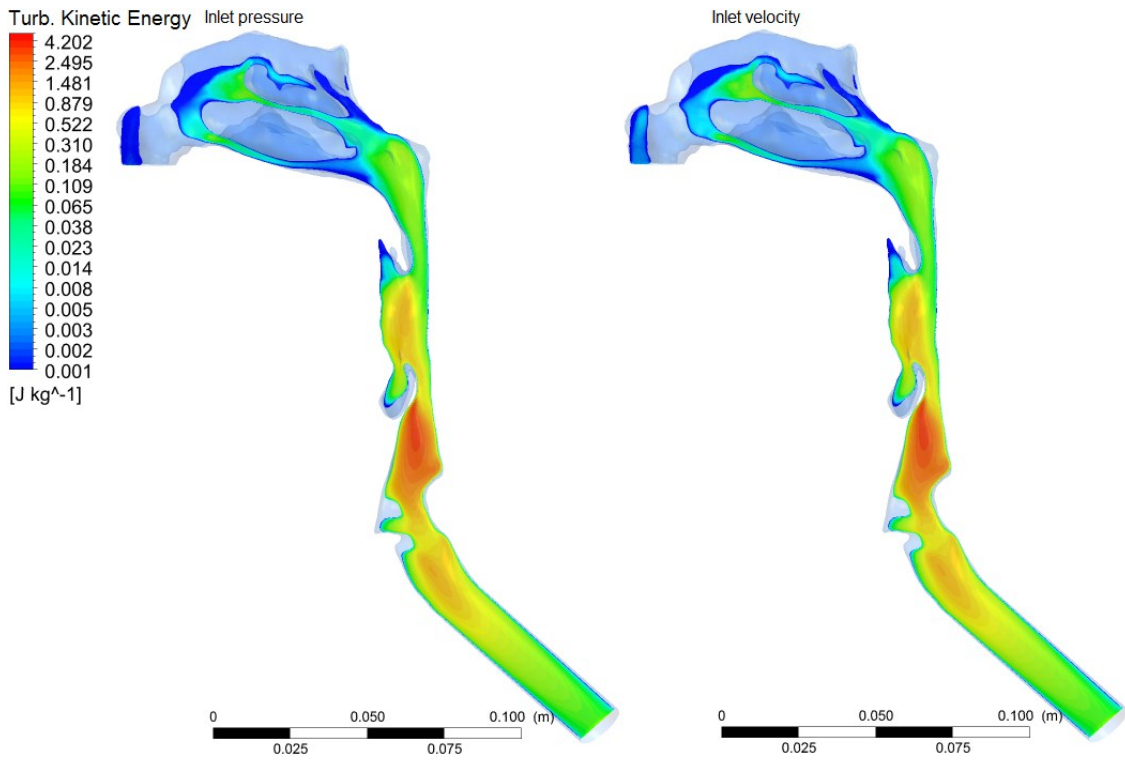
Figure 7.17: Turbulence kinetic energy in a vertical plane cut through the left nasal cavity, in logarithmic scale; comparison of flows in the pre-operative base-case geometry with pressure inlet condition and results with a velocity inlet condition
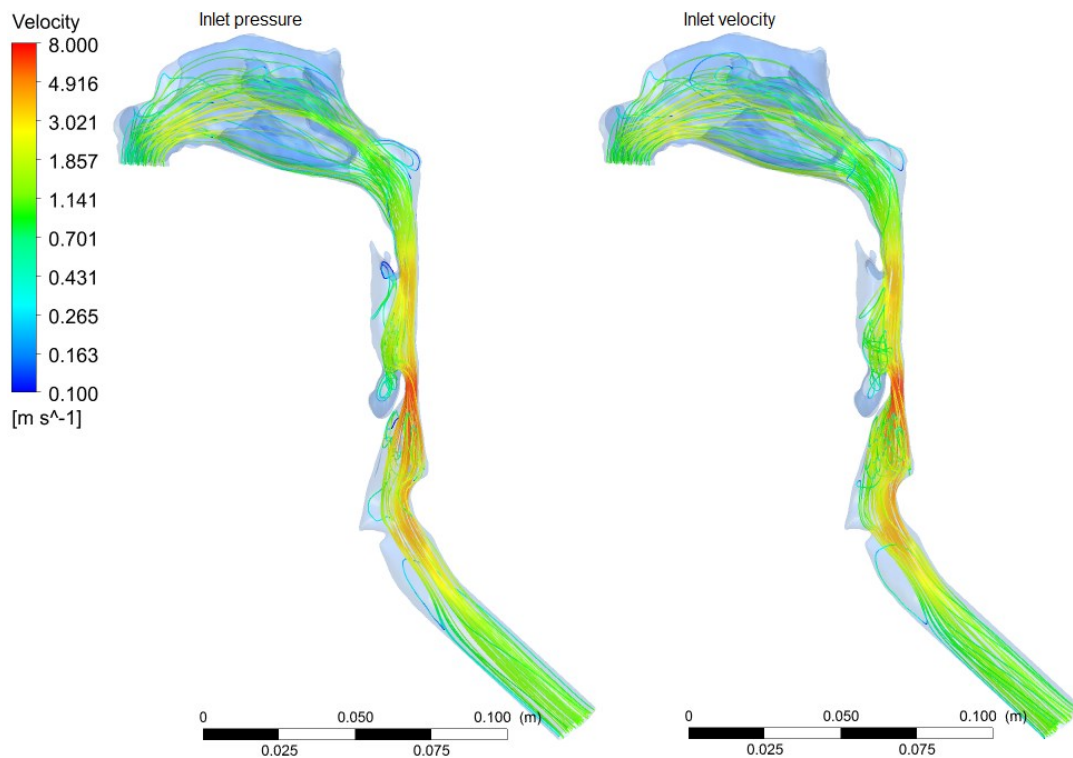
Figure 7.18: Velocity streamlines generated with 50 evenly distributed release points in the two nostrils, seen from the left, magnitude in logarithmic scale; comparison of flows in the pre-operative base-case geometry with pressure inlet condition and results with a velocity inlet condition

56

The wall pressure drops depicted in Figure 7.15 and Figure 7.16 are identical. When doing simulations with velocities as the inlet and outlet boundary conditions, and thus not defining the reference point for pressure, the software chooses to have zero gauge pressure at the outlet, so to compare results, the pressure drop is presented, not the gauge pressure as before. The turbulence kinetic energy in Figure 7.17 show two identical plots, except for right behind the inlets. The velocity streamlines in Figure 7.18 are similar in velocity magnitude, but the paths have more swirl in the velocity inlet situation. From these figures, one can conclude that in our model it is insignificant whether a pressure or velocity is used as an inlet condition. This is quantifiably verified in the area-averaged pressure and velocity graphs below and on the next page, confirming the insignificance of type of inlet condition.
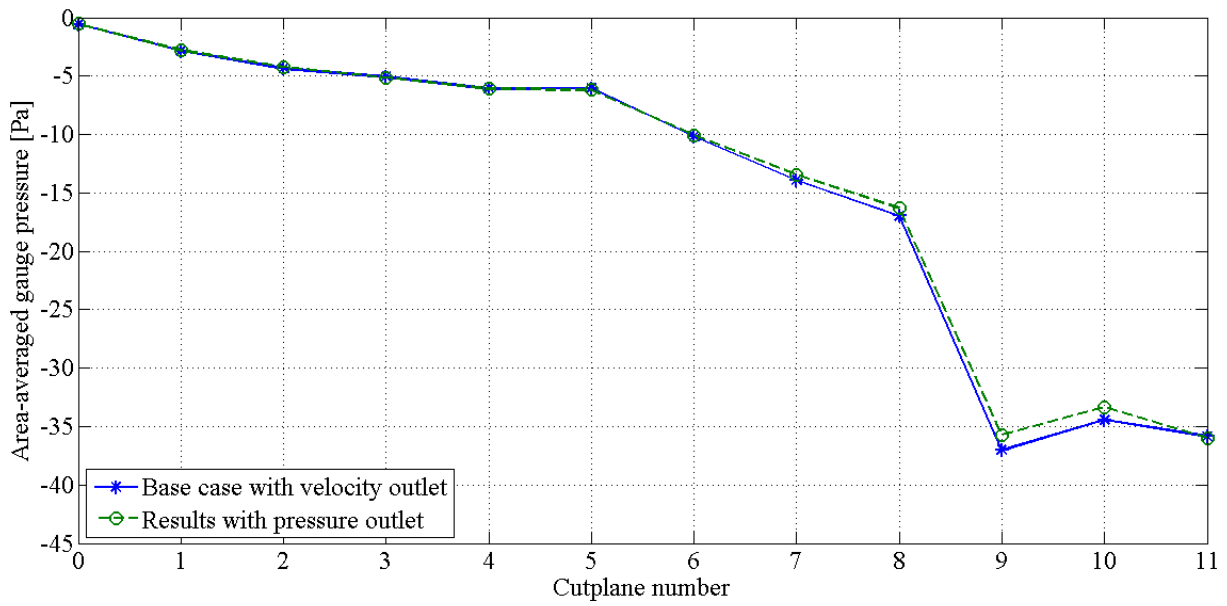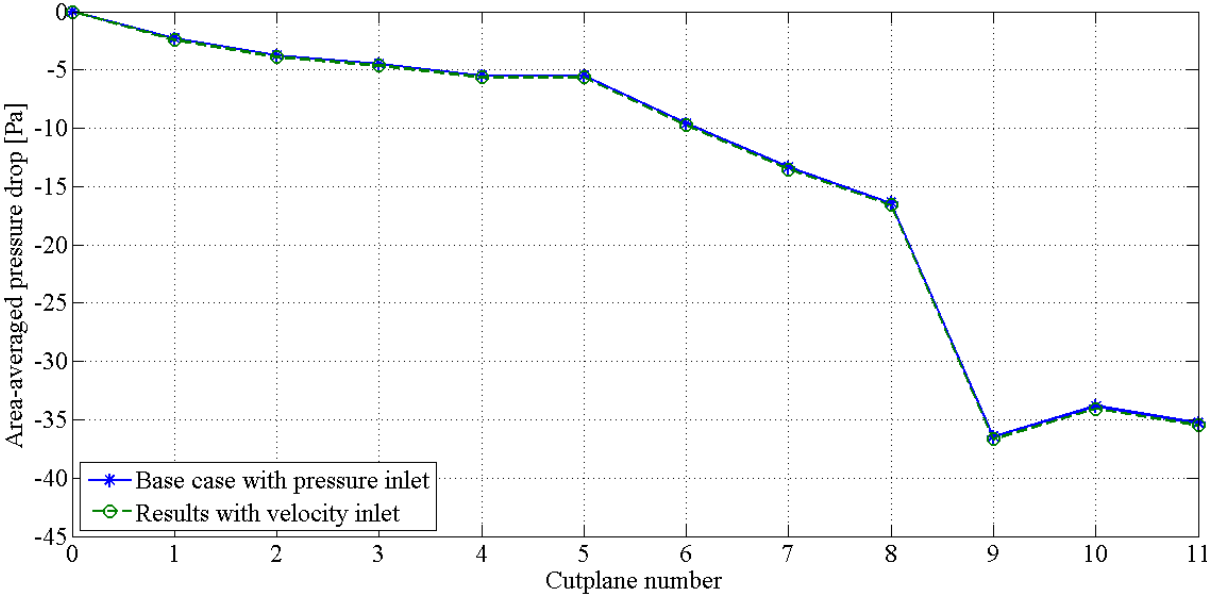

Figure 7.19: Area-averaged pressure drop plotted at cross-sections marked in Fig. 4.1 for the base case results with pressure inlet and comparative results with velocity inlet
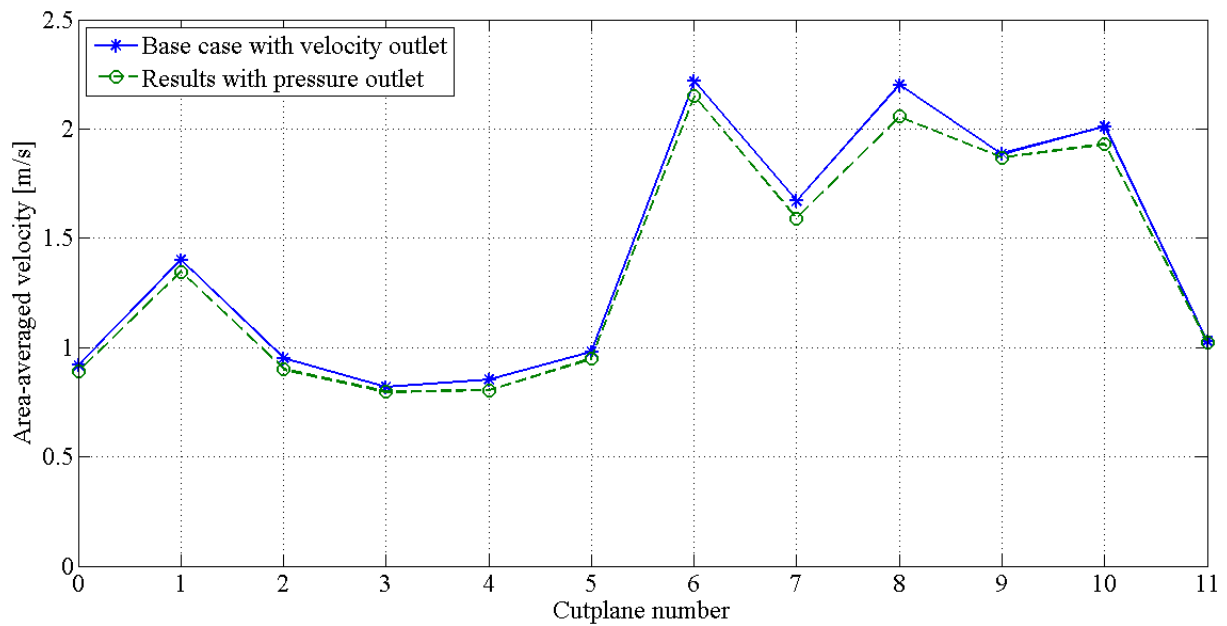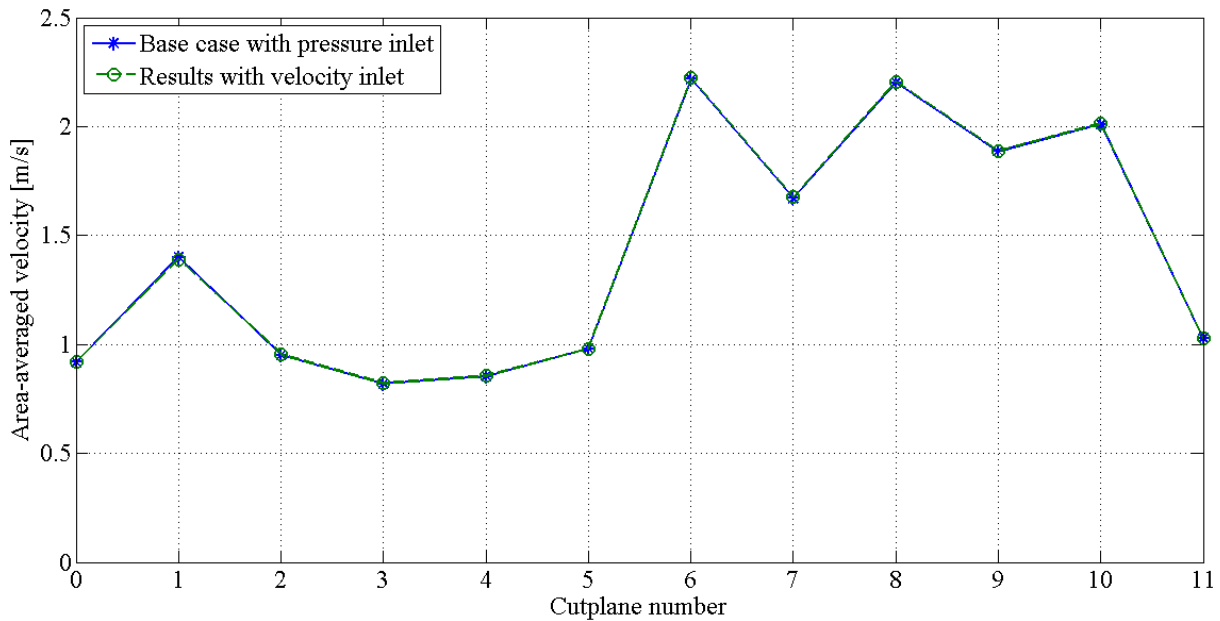
Figure 7.20: Area-averaged velocity plotted at cross-sections marked in Fig. 4.1 for the base case results with pressure inlet and comparative results with velocity inlet

7.3   Wall boundary conditions

The sensitivity to wall boundary condition was examined as described in chapter 6.3. For the pre-operative geometry with added roughness to the wall, the residuals for the continuity, k, ε, and x-, y- and z-velocities converged to values between 10^{-1} and 10^{-2}, which are not satisfyingly low values. It was also attempted to obtain satisfactory convergence by using a finer mesh of 10.1 million cells, but these results did not converge either. A comparison of the results from the pre-operative base case simulation and from a pre-operative geometry with a roughness height of 0.2 mm are depicted on the next pages. The results for the post-operative geometries with and without wall roughness are also included to highlight the difference in results due to a possible non-converged result in the pre-operative rough wall situation. Due to time constraints, it was not possible to re-run the pre-operative geometry. Therefore, the post-operative results for smooth and rough wall are also included to serve as a basis to draw a conclusion on the impact that roughness has on the flow. The post-operative base-case mesh of 1.3 million cells was utilized for the smooth wall simulation, while a finer mesh of 6.0 million cells, produced by Sverre G. Johnsen [10], was used for the post-operative rough wall simulation.
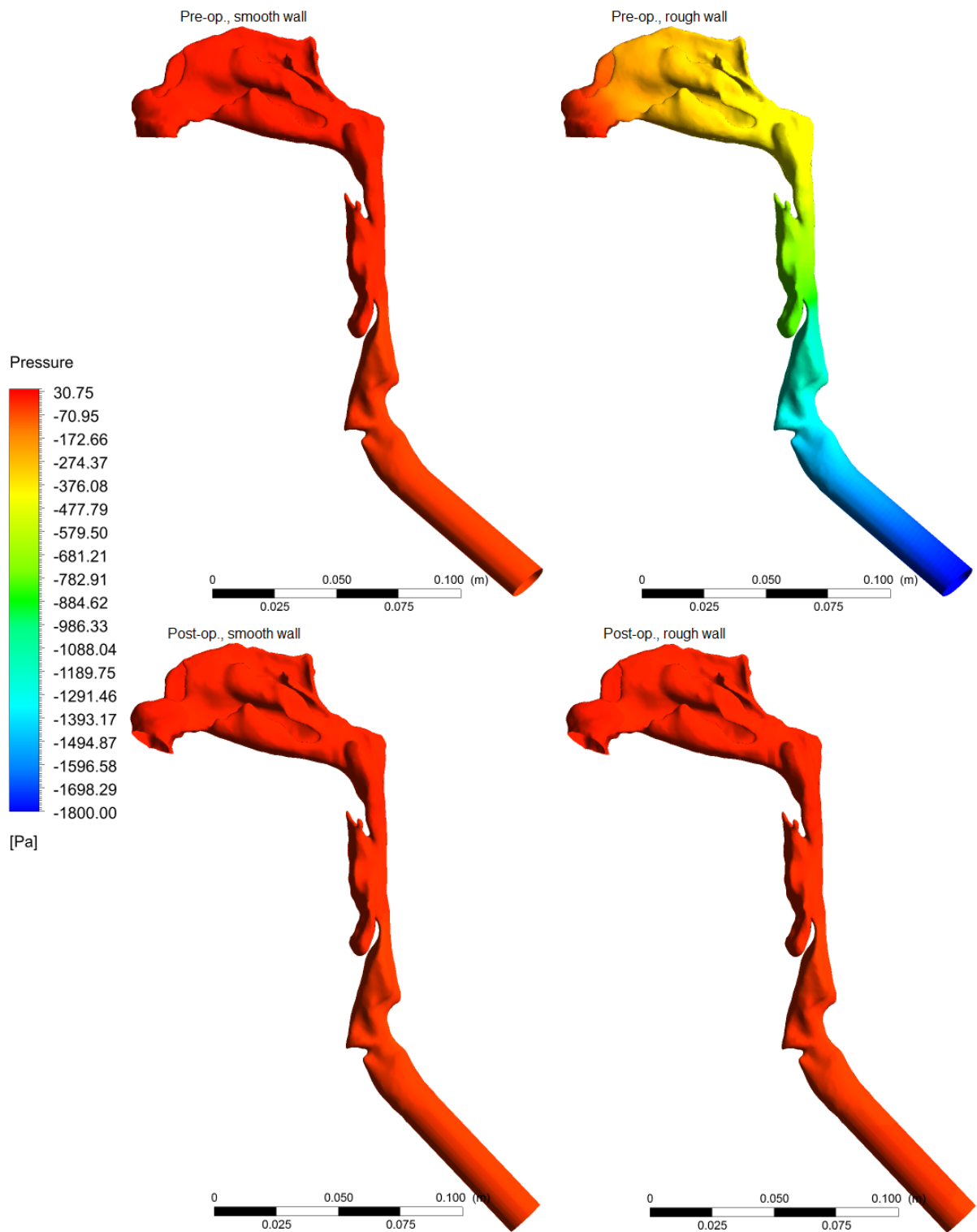
Figure 7.21: Wall pressure, seen from the left; comparison of flows in the pre-operative (upper) and post-operative (lower) geometry in the base-case with a smooth wall (left) and a wall with added roughness (right)

59

Figure 7.22: Turbulence kinetic energy in a vertical plane cut through the left nasal cavity, in logarithmic scale; comparison of flows in the pre-operative (upper) and post-operative (lower) geometry in the base-case with a smooth wall (left) and a wall with added roughness (right)

Figure 7.23: Velocity streamlines generated with 50 evenly distributed release points in the two nostrils, seen from the left, magnitude in logarithmic scale; comparison of flows in the pre-operative (upper) and post-operative (lower) geometry in the base-case with a smooth wall (left) and a wall with added roughness (right)

The wall pressure seen from the left is depicted in Figure 7.21, with a linear, large-range scale. It shows a clear deviation in the pre-operative, rough wall situation from the three other simulations. The pressure results from the pre-operative smooth wall and the post-operative rough and smooth wall simulations are in the same range as the previous base-case results, while the pre-operative rough wall gives pressure values about 40 times higher. In the turbulence kinetic energy plot (Figure 7.22) and velocity streamlines plot (Figure 7.23), the pre-operative, rough wall situation is observed to deviate from the other three situations as well. The deviation is also clear when looking at the area-averaged pressure and velocity in the graphs below and on the next page. One can suspect that the calculations with pre-operative geometry and a rough wall have not converged properly. To obtain reliable results, one should study the numerical solvers used in the calculations or perhaps try a different mesh.

Figure 7.24: Area-averaged gauge pressure plotted at cross-sections marked in Fig. 4.1 for the pre-operative base case results with a smooth wall and results from a rough wall simulation

Figure 7.25: Area-averaged velocity plotted at cross-sections marked in Fig. 4.1 for the pre-operative base case results with a smooth wall and results from a rough wall simulation

Since post-operative results have been obtained, they are included in the figures below and on the next pages to serve as a basis for the conclusion on wall roughness.
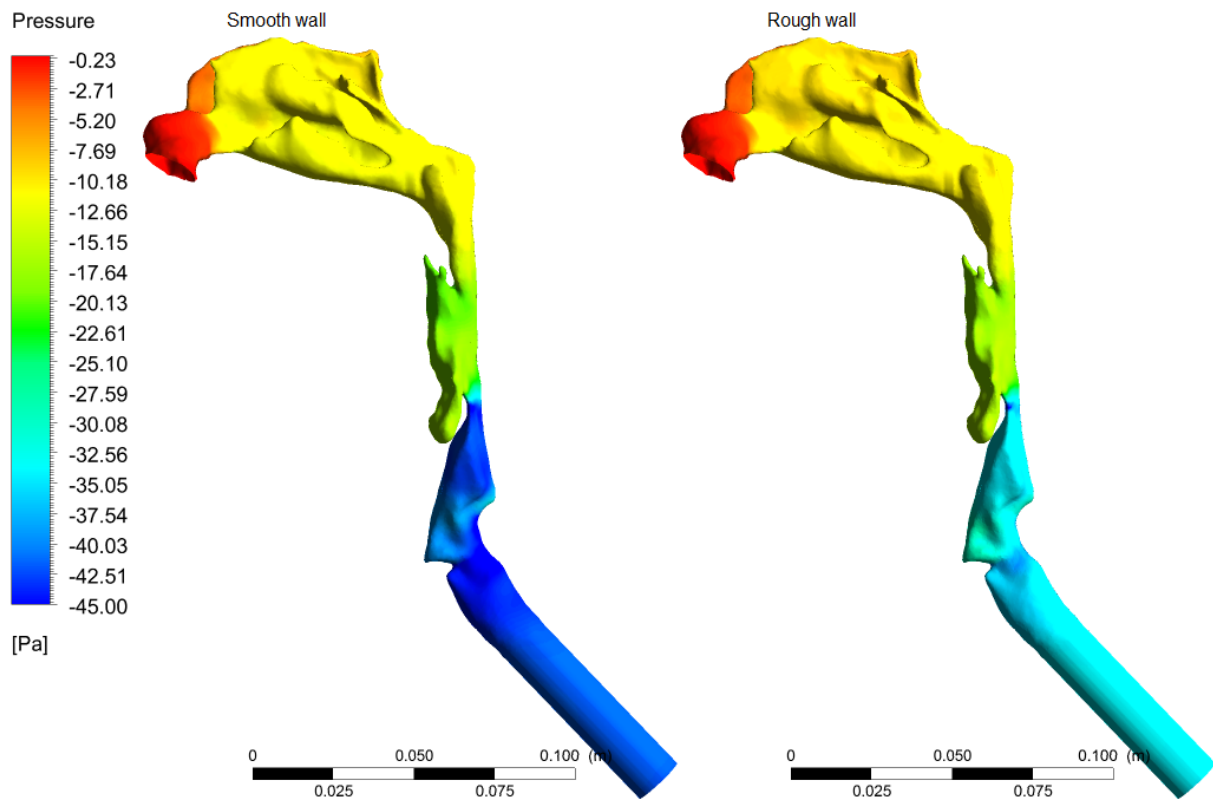
Figure 7.26: Wall pressure, seen from the left; comparison of flows in the post-operative geometry in the base-case with a smooth wall (left) and a wall with added roughness (right)
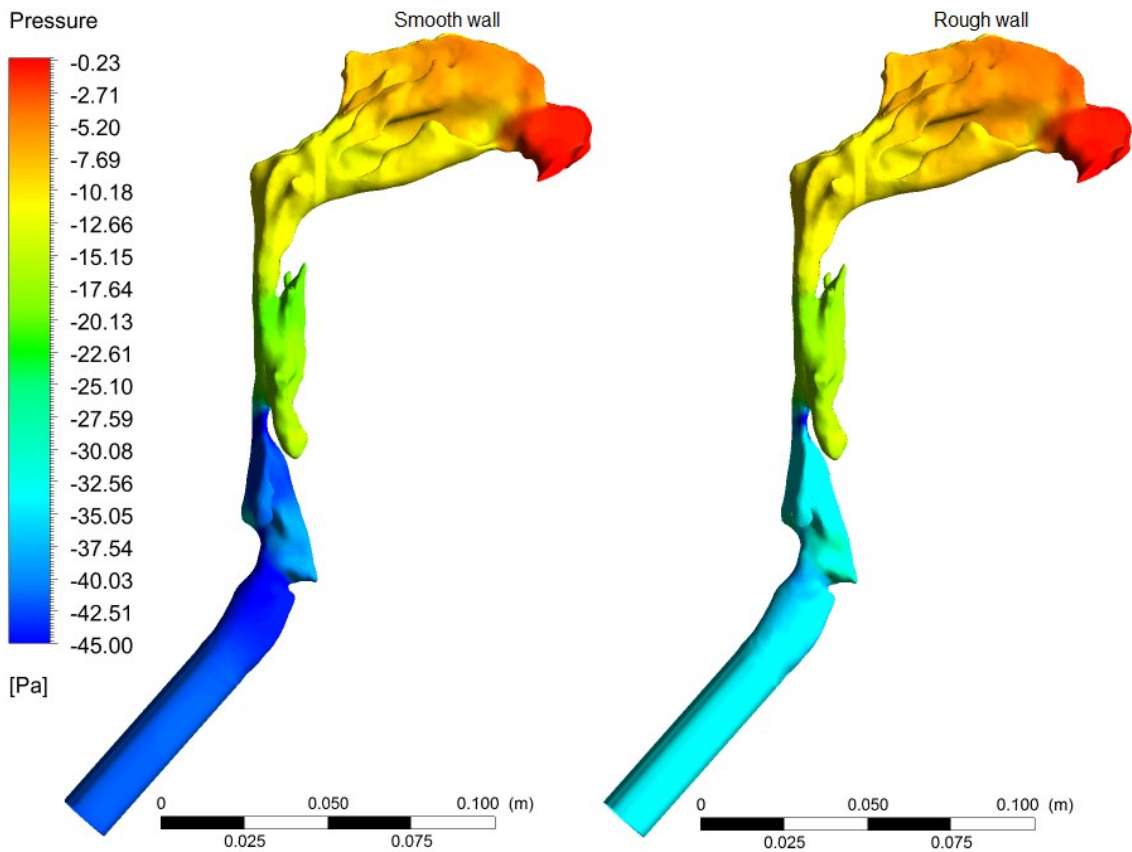
Figure 7.27: Wall pressure, seen from the right; comparison of flows in the post-operative geometry in the base-case with a smooth wall (left) and a wall with added roughness (right)
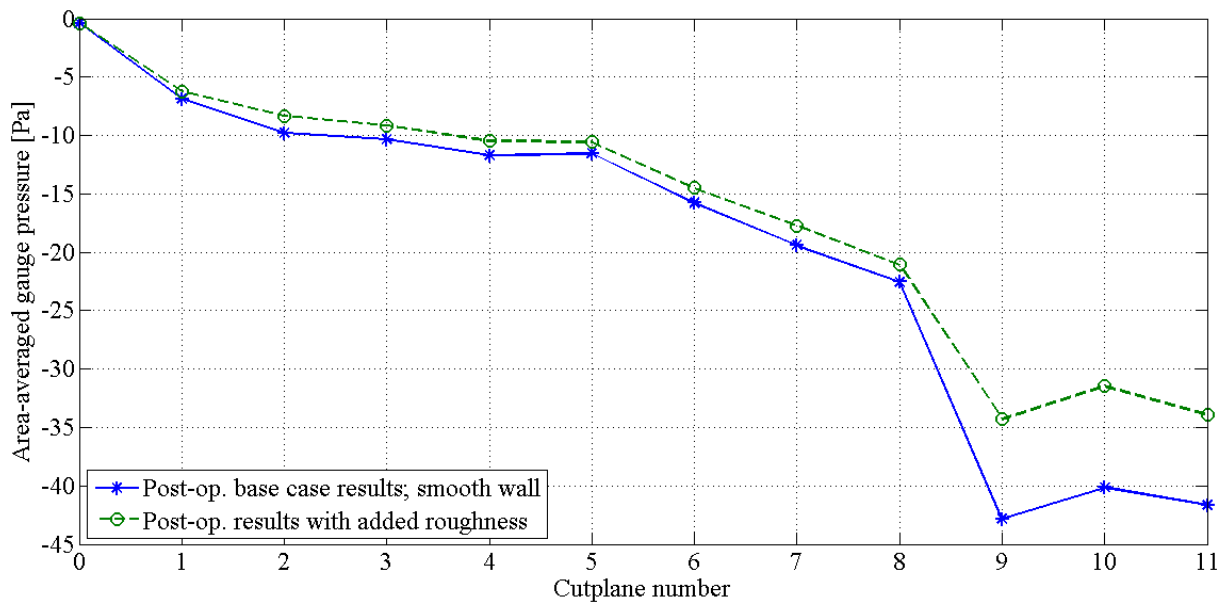
Figure 7.28: Area-averaged gauge pressure plotted at cross-sections marked in Figure 4.2 for the post-operative base case results with a smooth wall and results from a rough wall simulation

64
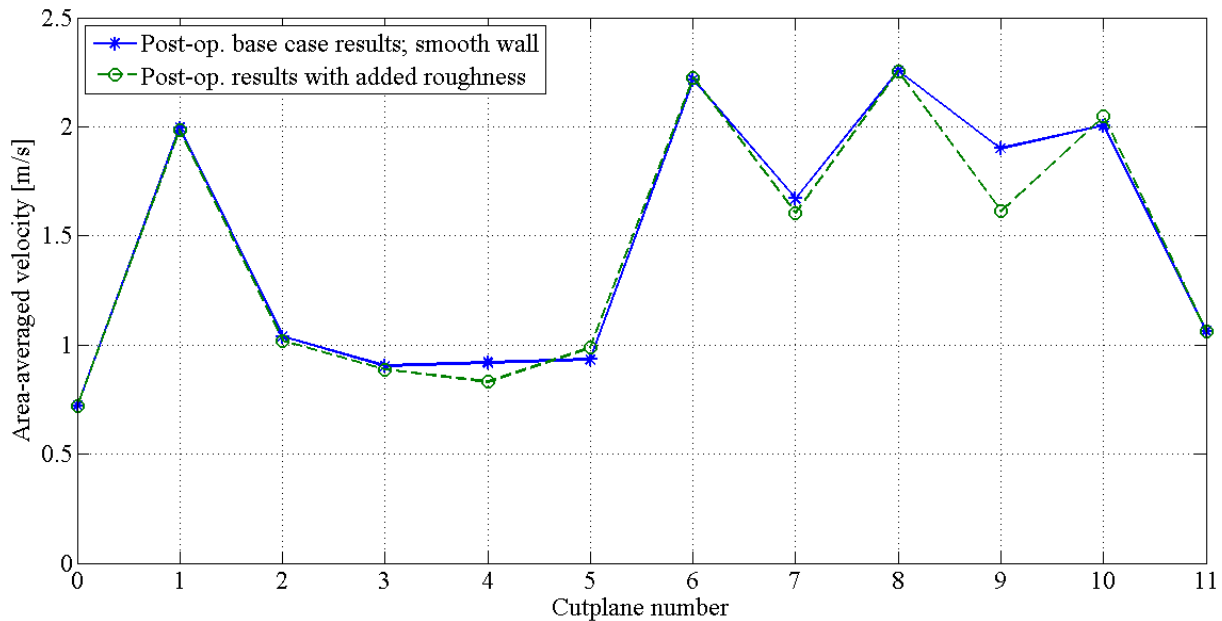
Figure 7.29: Area-averaged velocity plotted at cross-sections marked in Fig. 4.2 for the post-operative base case results with a smooth wall and results from a rough wall simulation

As can be seen in Figure 7.26, Figure 7.27 and Figure 7.28, the pressure drop is smaller when the wall has added roughness. The area-averaged velocity in Figure 7.29 is quite similar for the two situations, with the velocity being a bit smaller for the rough wall situation in some locations. It was expected that the roughness would only have a small impact on the pressure drop since the flow has low Reynolds numbers. The motivation for studying wall roughness was to see if this would provide additional friction loss to explain the significantly higher pressure drop seen in rhinomanometry measurements compared to CFD models with smooth walls. Although further research might be necessary, with respect to wall roughness, the preliminary conclusion is that wall roughness cannot explain the observed discrepancy between CFD models and measurements.

7.4   Grid size

The grid sensitivity was investigated as described in chapter 6.4. To see if the simulations had converged, the residuals for the continuity, k, ε, and x-, y- and z-velocities were monitored. For the grid with 10.1 million cells, the residuals started at about 1, and converged to values of around 10^{-7}, while the residuals for the 6.8 million cells grid converged to values between 10^{-4} and 10^{-9}. The base case mesh's residuals for the continuity, k, ε, and x-, y- and z-velocities converged to values between 10^{-4} and 10^{-8}. The resulting plots for the two finer grids compared to the base case simulation are depicted on the next pages.
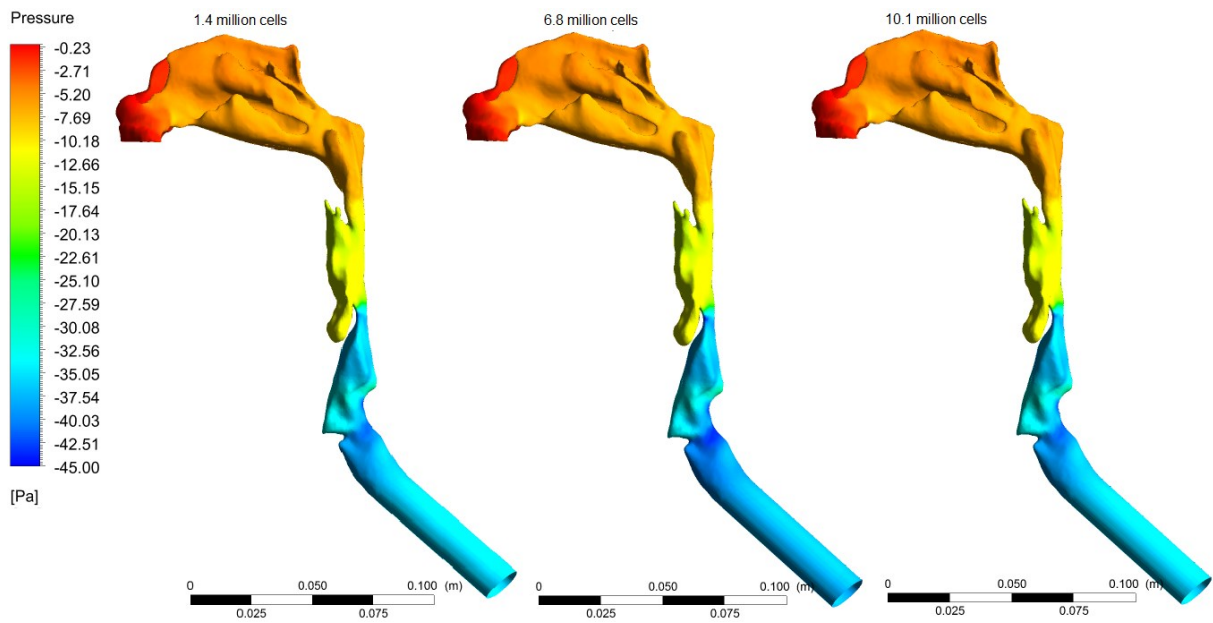
Figure 7.30: Wall pressure, seen from the left; comparison of flows in the pre-operative base-case geometry with three different meshes
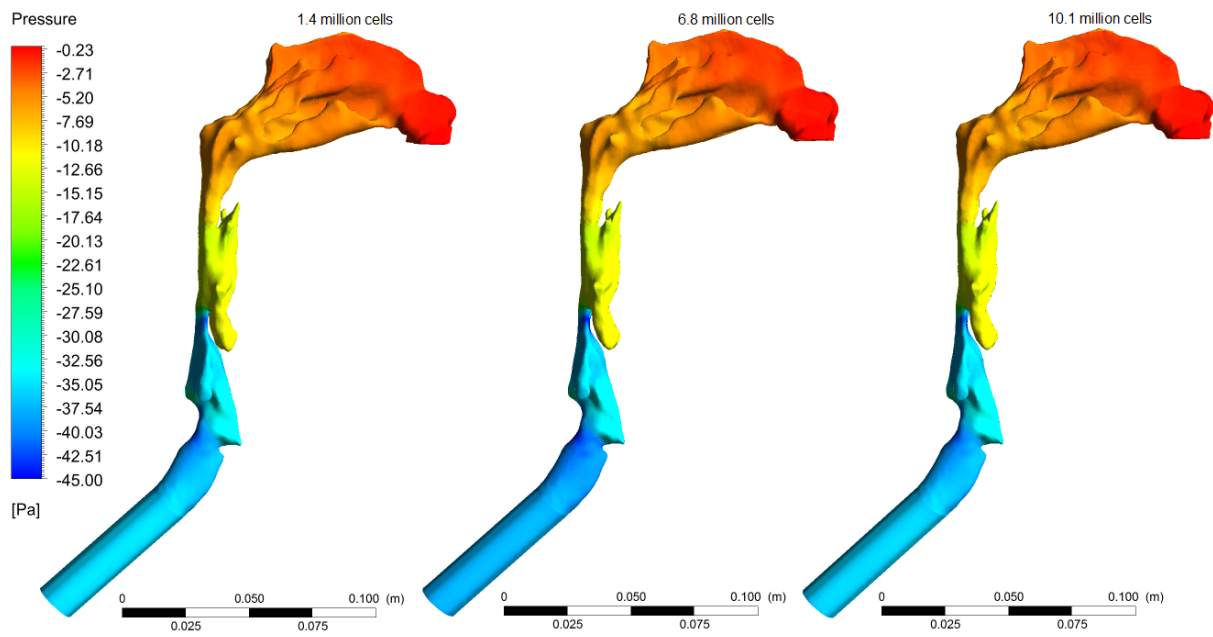
Figure 7.31: Wall pressure, seen from the right; comparison of flows in the pre-operative base-case geometry with three different meshes
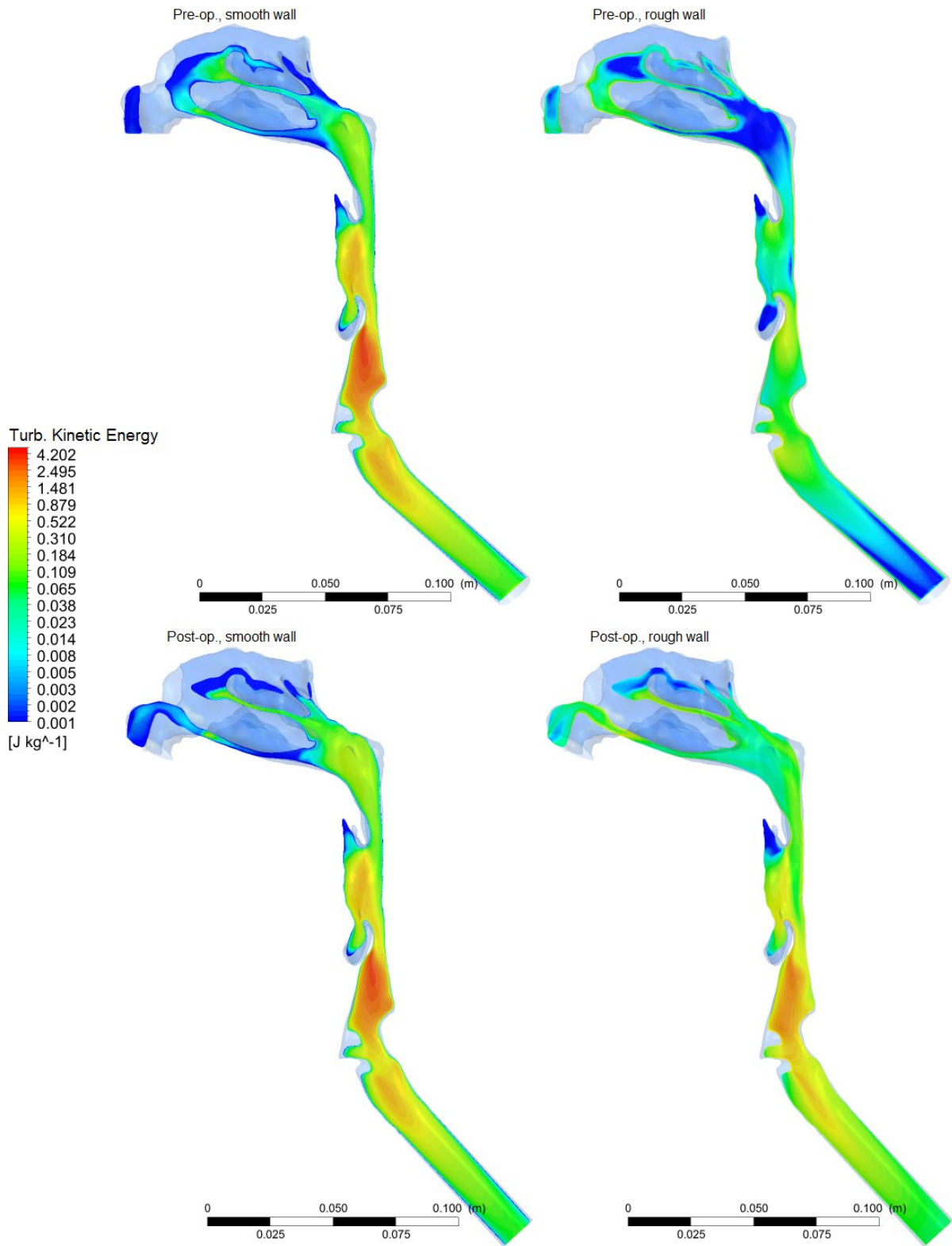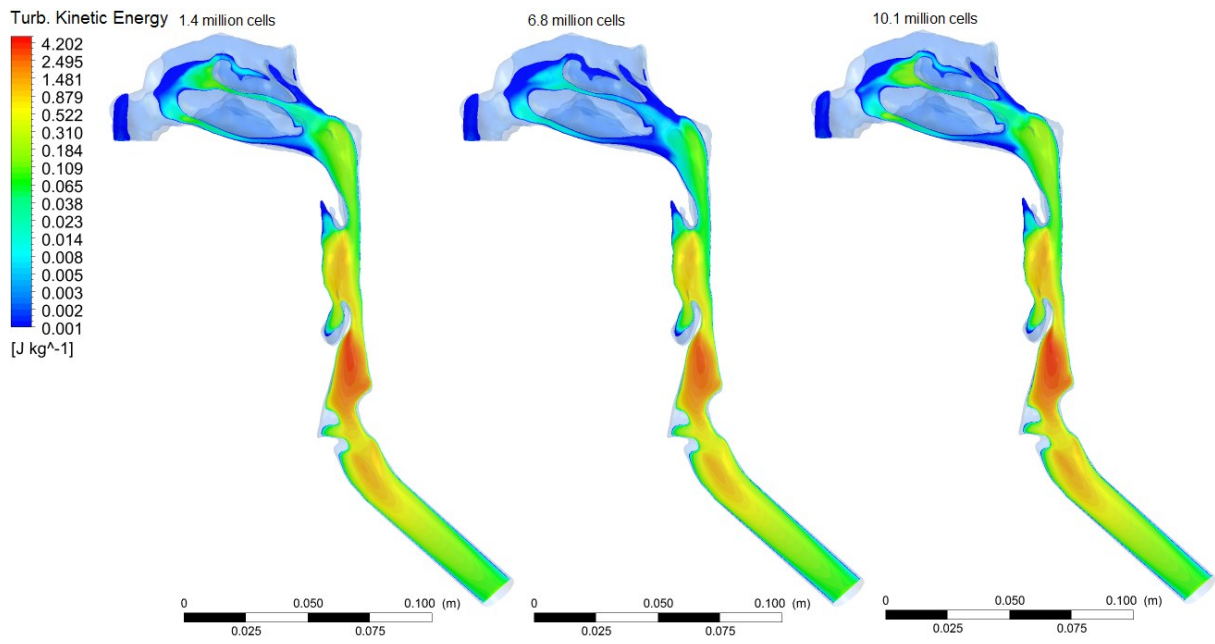
Figure 7.32: Turbulence kinetic energy in a vertical plane cut through the left nasal cavity, in logarithmic scale; comparison of flows in the pre-operative base-case geometry with three different meshes
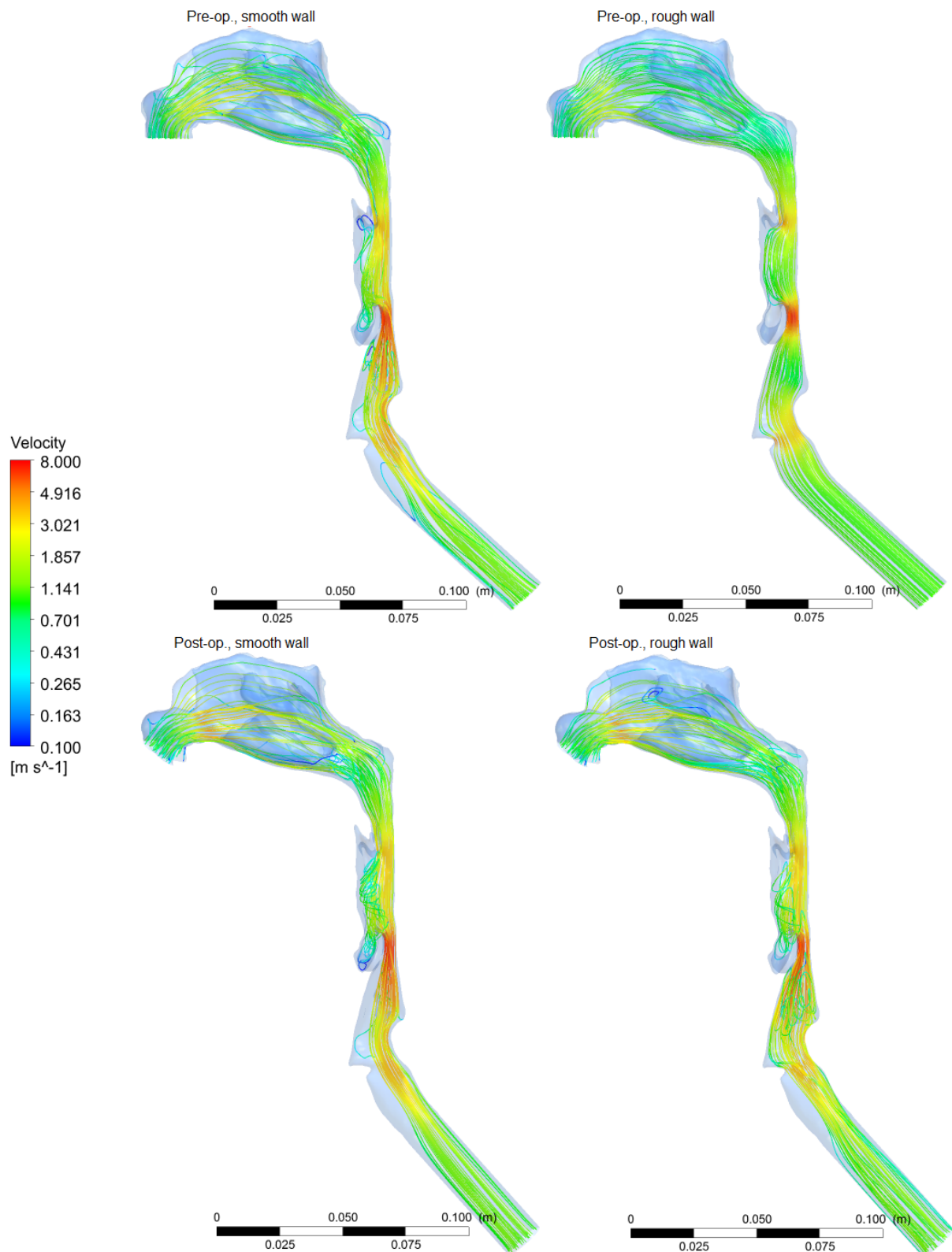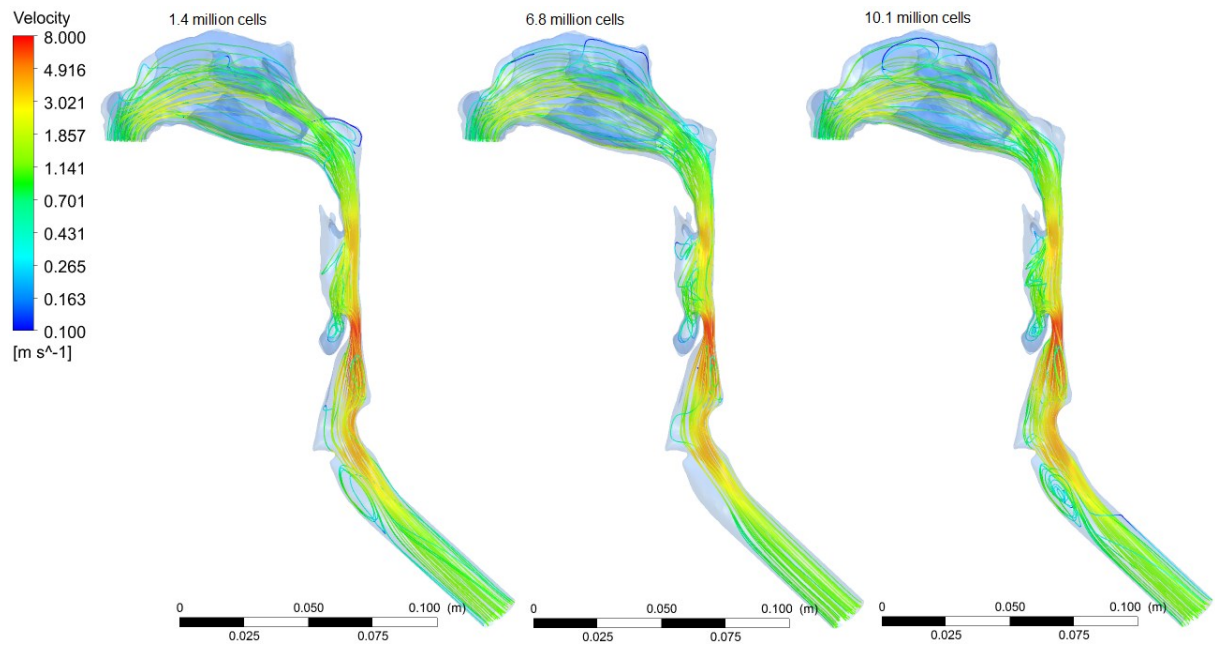

Figure 7.33: Velocity streamlines generated with 50 evenly distributed release points in the two nostrils, seen from the left, magnitude in logarithmic scale; comparison of flows in the pre-operative base-case geometry with three different meshes

As one can see in Figure 7.30 and Figure 7.31, the three grids yield virtually no difference in wall pressure. Figure 7.32 shows the turbulence kinetic energy and there are only small differences between the results for the three grids. The grids consisting of 1.4M and 10.1M cells yield almost identical TKE results, while the TKE results for the 6.8M cells grid, differ a little bit from the other two in the nasal cavity and after the epiglottis. However, these differences are minor, and since it is the finest and the coarsest grid that are the most alike, one can suspect that the 6.8M grid is of poor quality. The velocity magnitude is identical for the three grids, but the paths of the velocity streamlines show some difference, which can be seen in Figure 7.33. This is especially prominent in the oropharynx behind the oral cavity and further down after the epiglottis. To obtain a quantification of the differences, graphs have been produced for the area-averaged pressure and velocity, which are depicted below and on the next page.
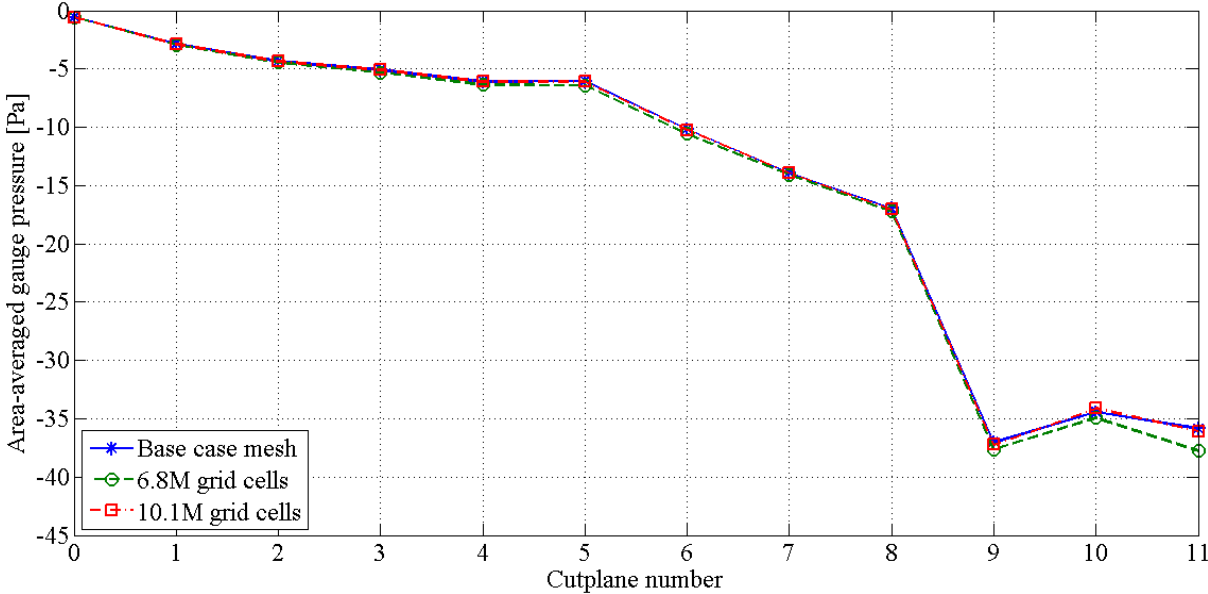
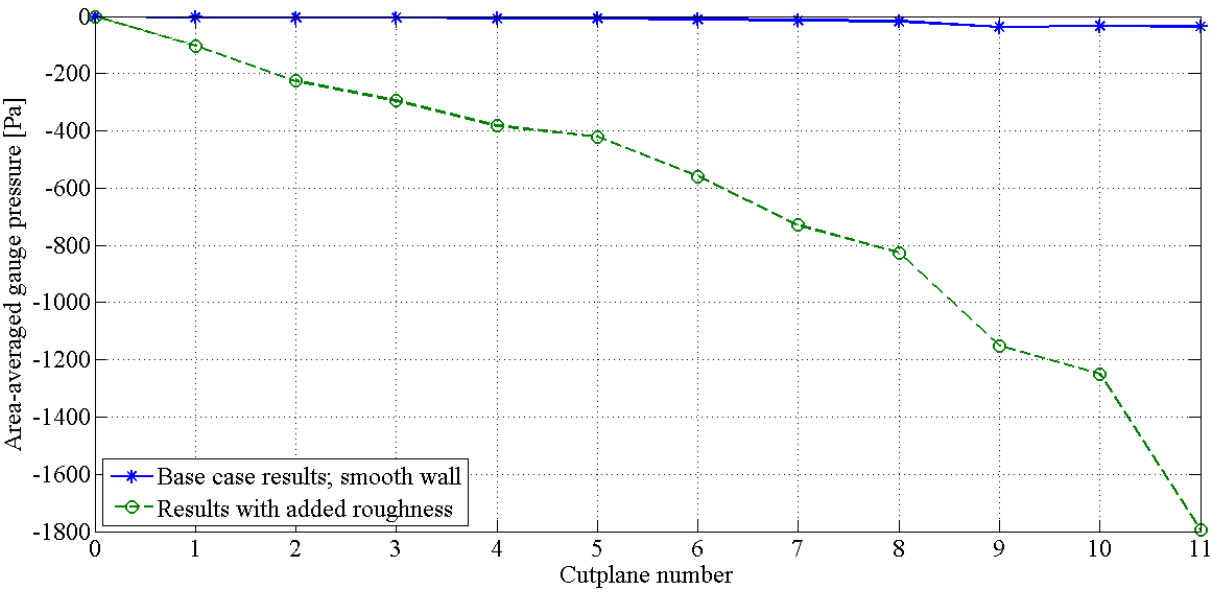*Figure 7.34: Area-averaged gauge pressure plotted at cross-sections marked in Fig. 4.1 for the base case results and results from two finer meshes*

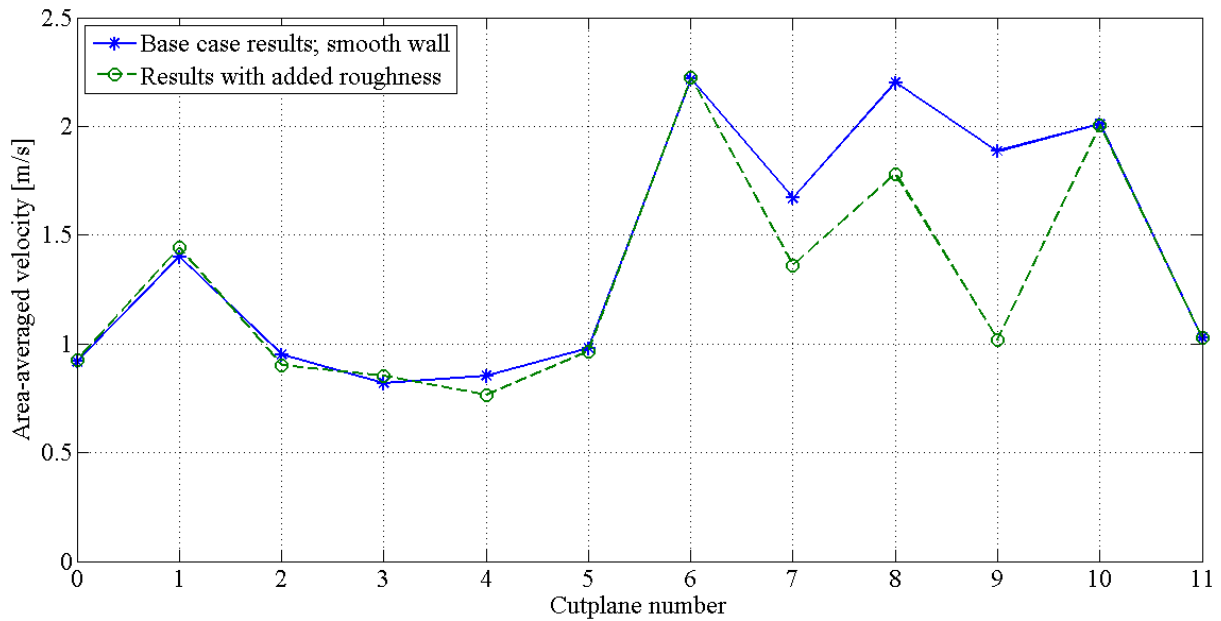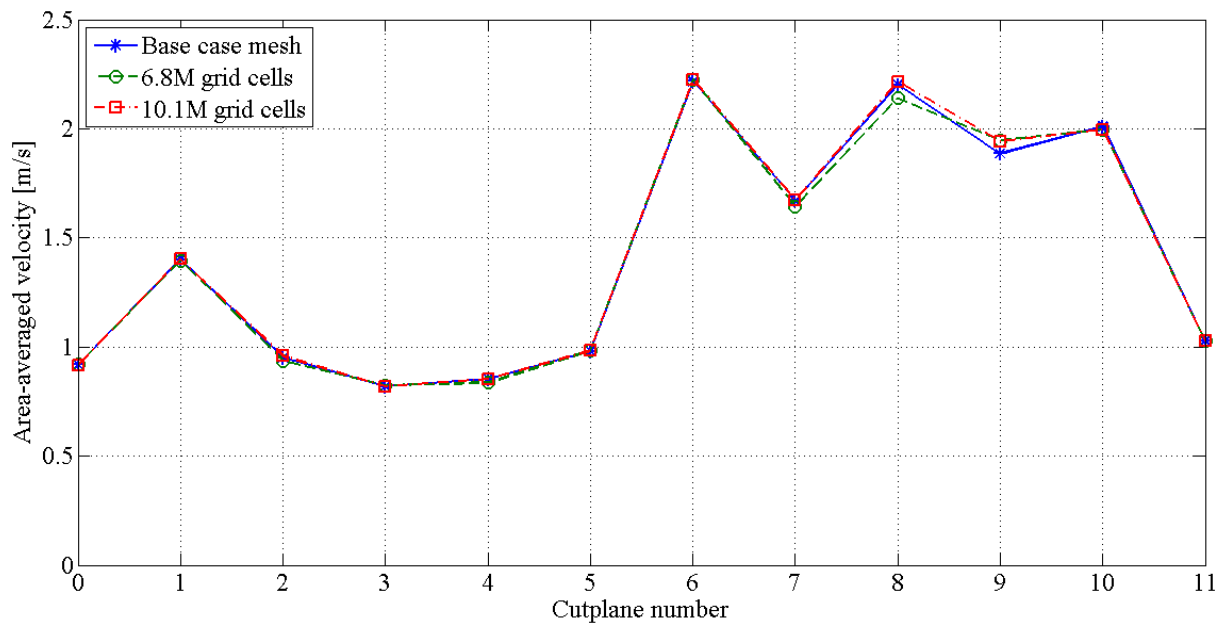*Figure 7.35: Area-averaged velocity plotted at cross-sections marked in Fig. 4.1 for the base case results and results from two finer meshes*

From the graphs in Figure 7.34 and Figure 7.35, one can observe that it is the 6.8M grid cells mesh that has the most deviating results. There is some difference between the base case mesh and the 10.1M grid cells mesh in the area-averaged pressure between cut-planes no. 7 and 10. Nevertheless, for the rest of the geometry regarding area-averaged velocity, and for the area-averaged gauge pressure in the entire geometry, the results for the base-case mesh and the 10.1M mesh are identical, leading to the conclusion that the base case mesh is sufficiently fine.

8 Conclusions

In the current study, patient-specific CFD simulations were conducted to examine the difference between the pre- and post-operative CFD results for the patient, and then the pre-operative results were compared with experimental data to study possible correlation. The effect of changing important model parameters such as effective geometry, inlet, outlet and wall boundary conditions, and grid size has been addressed through a sensitivity study.

The surgery performed on the patient in this study was a septoplasty, which is a procedure to straighten the septum. The simulation results predict that after surgery the flow is accelerated in the front part of the nasal cavity, causing an increase in pressure drop through this region. This contradicts the rhinomanometry data obtained for the same patient indicating lower pressure drop after surgery. The reason for the discrepancy is unresolved and needs further investigations. One explanation is that the rhinomanometry data are inaccurate, the other is that CFD, in its current state, is not able to predict this flow accurately enough.

With the aim of explaining the observed difference, a sensitivity study on some of the essential model input parameters was carried out. First, the airway geometry was investigated. When creating a geometry using CT imaging, it is challenging to choose the right border between tissue and air. By removing one pixel around the entire geometry, a narrower geometry was obtained. The simulation gave promising results, with higher values for the pressure drop, turbulence kinetic energy and velocity. The pressure drop was approximately twice as large in the narrower geometry compared to the base-case geometry, but still not as high as indicated by the rhinomanometry data.

A sensitivity study revealed that the flow was unaffected by choosing either uniform velocity or uniform pressure as the inlet and outlet boundary conditions. The base-case wall boundary condition is a smooth wall, which is a relatively large simplification when considering the small length scales that exist in for instance the nasal cavity, so the effect of wall roughness was investigated as well. The pre-operative simulation with a rough wall did not converge, so post-operative results were used for examinations. It was expected that the roughness would only have a small impact on the pressure drop due to the flow's low Reynolds numbers, which was also observed in the results. Thus, the preliminary conclusion was that wall roughness cannot explain the observed discrepancy between CFD models and measurements.

Lastly, the grid sensitivity was investigated by comparing three meshes of varying number of cells. The results led to the conclusion that the base-case mesh consisting of 1.4 million cells is sufficiently fine, as these results match the results from the finer mesh of 10.1 million cells well.

9 Further work

The goal is that CFD should become a reliable tool for studying flow patterns in the human body and assist medical personnel in making a diagnosis and predicting the success of treatment. We cannot yet draw this conclusion, as the CFD results compared to rhinomanometry data do not correlate well. To progress, it is crucial to evaluate the accuracy of the rhinomanometry data before attempting to modify the modeling approach.

The simplification of a fixed inlet velocity is not realistic, since the actual flow rate varies similarly to a sine function, with inhalation and exhalation. There are some characteristics for an accelerated flow that are not taken into account when having a constant inflow velocity. More realistic flow rates should be included in future research in order to capture the effects of accelerating and decelerating velocity on friction and flow pattern in general.

Our problem is assumed to be a steady problem, since our focus is on a constant inflow with no rapid changes. In reality, this might not be the case, since a realistic flow will consist of, among other things, inspiration, expiration, obstructions and sharp inhalation, such as gasping. Even if the boundary conditions are steady, the flow pattern might change with time. The steady state assumption could cause poor convergence for some turbulence models [1]. In future work, one should instead use a transient solver, as the flow includes several recirculating zones that are transient in nature.

A geometry sensitivity study has been performed, but more investigation of this issue should be included in future research on the topic. The same goes for the wall boundary condition, as the pre-operative rough wall simulation did not converge properly and it was only a preliminary conclusion that wall roughness could not explain the discrepancy between CFD and experimental data. In addition, only one roughness height was included, so to study this issue further, one should investigate several roughness heights and perhaps also several roughness constants. One should also consider including a different type of wall boundary condition, such as slip on the wall due to mucus.

It might not be the right approach to simply make a smaller geometry or add roughness, when it could be several factors affecting the flow simultaneously. When the different parameters have been investigated and if two or more factors show significant effects in the flow, one should consider combining the different factors and perform new investigations.

Rigid wall is another simplification made which is not entirely correct. The pressure induced deformation of the soft tissue in the human upper airways can affect the flow greatly. For better results, one should consider conducting simulations with a more realistic non-rigid wall and some level of fluid-structure interaction.

References

[1] Aasgrav, E. (2016) *CFD simulations of turbulent flow in the upper airways*. Project work. The Norwegian University of Science and Technology.

[2] Aasgrav, E., Johnsen, S.G., Simonsen, A.J. and Müller, B. (2017) CFD simulations of turbulent flow in the upper airways, *CFD2017: 12th International Conference on CFD in Oil & Gas, Metallurgical and Process Industries*. Trondheim, Norway, 30 May - 1 June, 2017.

[3] ANSYS (2017), http://www.ansys.com.

[4] Bredberg, J. (2000) On the wall boundary condition for turbulence models. Internal Report, Chalmers University of Technology. Available at: https://www.researchgate.net/publication/255608559_On_the_Wall_Boundary_Condition_for_Turbulence_Models

[5] El Gharbi, N., Absi, R., Benzaoui, A. and Amara, E.H. (2009) Effect of near-wall treatment on airflow simulations, *International conference on computational methods for energy engineering and environment: ICCM3E*. Sousse, Tunisia, 20-22 November, 2009. pp. 185-189.

[6] Flemons, W.W., Buysse, D., Redline, S., Oack, A., Strohl, K., Wheatley, J., Young, T., Douglas, N., Levy, P., McNicolas, W., Fleetham, J., White, D., Schmidt-Nowarra, W., Carley, D. and Romaniuk, J. (1999) Sleep-related breathing disorders in adults: Recommendations for syndrome definition and measurement techniques in clinical research, *SLEEP*, 22(5), pp. 667-689.

[7] *FLUENT 6.3 User's Guide* (2006). Available at: https://www.sharcnet.ca/Software/Fluent6/html/ug/main_pre.htm (Accessed: 05.06.17).

[8] Fogel, R.B., Malhotra, A. and White, D.P. (2004) Sleep - 2: Pathophysiology of obstructive sleep apnoea/hypopnoea syndrome, *Thorax*, 59(2), pp. 159-163. doi: 10.1136/thx.2003.015859

[9] ITK-SNAP (2014), http://www.itksnap.org/pmwiki/pmwiki.php.

[10] Johnsen, S.G. (2016-2017) Private communication.

[11] Jordal, M.R. (2015) *Geometry retrieval from CT and MRI of the human upper airways*. Project work. The Norwegian University of Science and Technology.

[12] Jordal, M.R. (2016) *Patient specific numerical simulation of flow in the human upper airways*. Master's thesis. The Norwegian University of Science and Technology.

[13] Jordal, M.R., Johnsen, S.G., Dahl, S.K. and Müller, B. (2017) Patient Specific Numerical Simulation of Flow in the Human Upper Airways for Assessing the Effect of Nasal Surgery, *CFD 2017: 12th International Conference on CFD in Oil & Gas, Metallurgical and Process Industries*. Trondheim, Norway, 30 May - 1 June, 2017.

[14] Kamat, S.S. (2015) *Practical Applications of Mechanical Ventilation*. JP Medical Publishers. pp. 82.

[15] Karthik, T. S. D. (2011) Turbulence models and their applications, *10th Indo German Winter Academy*. Presentation. Indian Institute of Technology Madras. Available at: www.leb.eei.uni-erlangen.de/winterakademie/2011/report/content/course01/pdf/0112.pdf

[16] Kleinstreuer, C. and Zhang, Z. (2003) Laminar-to-turbulent fluid-particle flows in a human airway model, *International Journal of Multiphase Flow*, 29, pp. 271-289.

[17] Longest, P.W. and Vinchurkar, S. (2007) Validating CFD predictions of respiratory aerosol deposition: Effects of upstream transition and turbulence, *Journal of Biomechanics*, 40, pp. 305-316. doi:10.1016/j.jbiomech.2006.01.006

[18] Lu, M.Z., Liu, Y. and Ye, J.Y. (2012) Turbulent flow pattern in upper airway with obstructed sleep apnea, *15th International Symposium on Flow Visualization, ISFV15*. Minsk/Belarus, 25-28 June, 2012.

[19] Luo, X.Y., Hinton, J.S., Liew, T.T. and Tan, K.K. (2004) LES modelling of flow in a simple airway model, *Medical Engineering & Physics*, 26, pp. 403-413. doi:10.1016/j.medengphy.2004.02.008

[20] Ma, B. and Lutchen, K.R. (2009) CFD simulation of aerosol deposition in an anatomically based human large-medium airway model, *Annals of Biomedical Engineering*, 37(2), pp. 271-285. doi: 10.1007/s10439-008-9620-y

[21] Mihaescua, M., Murugappanb, S., Kalrac, M., Khoslab, S. and Gutmark, E. (2008) Large Eddy Simulation and Reynolds-Averaged Navier–Stokes modeling of flow in a realistic pharyngeal airway model: An investigation of obstructive sleep apnea, *Journal of Biomechanics*, 41, pp. 2279–2288. doi:10.1016/j.jbiomech.2008.04.013

[22] Mylavarapu, G., Murugappan, S., Mihaescu, M., Kalra, M., Khosla, S. and Gutmark, E. (2009) Validation of computational fluid dynamics methodology used for human upper airway flow simulations, *Journal of Biomechanics*, 42, pp. 1553-1559. doi:10.1016/j.jbiomech.2009.03.035

[23] Nithiarasu, P., Hassan, O., Morgan, K., Weatherill, N.P., Fielder, C., Whittet, H., Ebden, P. and Lewis, K.R. (2008) Steady flow through a realistic human upper airway geometry, *International Journal for Numerical Methods in Fluids*, 57, pp. 631-651. doi: 10.1002/fld.1805

[24] Nithiarasu, P., Liu, C.-B. and Massarotti, N. (2007) Laminar and turbulent flow calculations through a model human upper airway using unstructured meshes, *Communications in Numerical Methods in Engineering*, 23, pp. 1057-1069. doi: 10.1002/cnm.939

[25] OSAS (2014) *Modeling of Obstructive Sleep Apnea by Fluid-Structure Interaction in the Upper Airways*. Available at: http://www.osas.no (Accessed: 16.05.17).

[26] Pope, S.B. (2004) Ten questions concerning the large-eddy simulation of turbulent flows, *New Journal of Physics*, 6(35). PII: S1367-2630(04)73040-2

[27] Pope, S.B. (2000) *Turbulent Flows*. Cambridge University Press.

[28] Riazuddin, V.N., Zubair, M., Abdullah, M.Z., Rushdan, I., Shuaib, I.L., Hamid, S.A. and Ahmad, K.A. (2011) Numerical study of inspiratory and expiratory flow in a human nasal cavity, *Journal of Medical and Biological Engineering*, 31(3), pp. 201-206. doi: 10.5405/jmbe.781

[29] Ritchey, G (2014) *Dental Management of Obstructive Sleep Apnea*. Available at: https://www.sciencebasedmedicine.org/dental-management-of-obstructive-sleep-apnea/ (Accessed: 01.11.16).

[30] Shao, J., Bhushan, S., Xing, T. and Stern, F. (Year unknown) Turbulence modeling in computational fluid dynamics (CFD). Lecture presentation. University of Idaho. Available at: http://taoxing.net/index.php?p=1_12_CFD-Materials

[31] Shi, H., Kleinstreuer, C. and Zhang, Z. (2007) Modeling of inertial particle transport and deposition in human nasal cavities with wall roughness, *Aerosol Science*, 38, pp. 398-419. doi:10.1016/j.jaerosci.2007.02.002

[32] Shih, T.H., Liou, W.W., Shabbir, A., Yang, Z. and Zhu, J. (1995) A new k-ε eddy viscosity model for high Reynolds number turbulent flows, *Computers Fluids*, 24(3), pp. 227-238. doi: 10.1016/0045-7930(94)00032-T

[33] Sondak, D. L. (1992) *Wall functions for the k-ε turbulence model in generalized nonorthogonal curvilinear coordinates*. PhD dissertation. Iowa State University.

[34] Stapleton, K. W., Guentsch, E., Hoskinson, M. K. and Finlay, W. H. (2000) On the suitability of k-ε modeling for aerosol deposition in the mouth and throat: A comparison with experiment, *Journal of Aerosol Science*, 31(6), pp. 739-749. PII: S0021-8502(99)00547-9

[35] Stylianou, F.S., Sznitman, J. and Kassinos, S.C. (2016) Direct numerical simulation of particle laden flow in a human airway bifurcation model, *International Journal of Heat and Fluid Flow*, pp. 1-34. doi: 10.1016/j.ijheatfluidflow.2016.07.013

[36] Tu, J., Inthavong, K. and Ahmadi, G. (2013*) Computational Fluid and Particle Dynamics in the Human Respiratory System*. Springer. pp. 19-20. doi: 10.1007/978-94-007-4488-2

12th International Conference on CFD in Oil & Gas, Metallurgical and Process Industries
SINTEF, Trondheim, Norway
May 30th – June 1st 2017

CFD 2017

Appendix A: Paper for the CFD2017 conference

CFD SIMULATIONS OF TURBULENT FLOW IN THE HUMAN UPPER AIRWAYS

Elin AASGRAV[1*], Sverre G. JOHNSEN[2], Are J. SIMONSEN[2], Bernhard MÜLLER[1]

[1] NTNU, dept. Energy and Process Technology, 7491 Trondheim, NORWAY

[2] SINTEF Materials and Chemistry, 7465 Trondheim, NORWAY

* E-mail: eaasgrav@gmail.com

ABSTRACT

In this paper, investigations are conducted using Reynolds-averaged Navier-Stokes (RANS) turbulence models to investigate the importance of turbulence modelling for nasal inspiration at a constant flow rate of 250 ml/s. Four different, standard turbulence models are tested in a model geometry based on pre-operative CT images of a selected obstructive sleep-apnea syndrome (OSAS) patient. The results show only minor differences between them. Furthermore, the turbulence models do not give significantly different results than a laminar flow model. Thus, the main conclusion is that effects of turbulence are insignificant in CFD modelling of the airflow in the pre-operative model of the upper airways of the chosen patient.

Keywords: CFD, Biomechanics, Obstructive Sleep Apnea, Turbulence, Upper airways.

NOMENCLATURE

Greek Symbols

δ_{ij} Kronecker delta, [-].

ρ Mass density, [kg/m^3].

ν Kinematic viscosity, [m^2/s].

ν_T Turbulence eddy viscosity, [m^2/s].

Latin Symbols

k Turbulence kinetic energy, [m^2/s^2].

p Pressure, [Pa].

$\boldsymbol{U}$ Velocity vector, [m/s].

U_i Mean velocity component in the i direction, [m/s].

x, y, z Cartesian coordinates, [m].

Sub/superscripts

i, j, k Spatial coordinate indexes.

w Wall.

INTRODUCTION

Snoring is caused by the soft parts of the upper airways collapsing and preventing the air from flowing freely. In some cases, snoring is so severe that medical attention is required. The most severe form, called obstructive sleep apnea syndrome (OSAS) involves complete blocking of the airway during sleep because of the collapse of e.g. relaxed muscles and soft tissue due to e.g. Venturi effect and gravity, in particular when the patient is lying in the supine position. It affects 2-4 % of the population. A variety of treatment options exists, but currently there are no available methods for predicting the outcome of the treatment. In order to gain insight into the biomechanical mechanisms of OSAS, computational fluid dynamics (CFD) simulations of flow in the human upper airways have been performed.

In short, the conclusions from previous studies indicate that the turbulence model that compares best with experimental data varies from case to case. Mihaescua et al. (2008) conclude that the Large Eddy Simulation (LES) modelling approach is a better option compared to the standard Reynolds-Averaged Navier-Stokes (RANS) models k-ε and k-ω, with k-ω being slightly better than k-ε. The RANS modelling approach is not able to capture flow separation effects, which are important for the understanding of the flow, as well as the LES approach. Riazuddin et al. (2011) conducted a study of inspiratory and expiratory flow in the nasal cavity using a k-ω SST turbulence model. The results were validated with experimental and numerical data from other studies, and they showed good correlation. The conclusion of the study was that the k-ω SST model gave accurate and reliable results for the flow involving adverse pressure gradients. Ma et al. (2009) used a realizable k-ε model when simulating flow and aerosol delivery in the human airways, and obtained good agreement with experimental data. Stapleton et al. (2000) used a standard k-ε model and concluded that CFD simulation do not compare very well with experimental data. They argued that the reason for this could be that particle deposition is very sensitive to pressure drop and recirculation, highlighting the need for accuracy in the reproduction of these flow characteristics to obtain good

results. Longest et al. (2007) considered variations of the k-ω turbulence model. The standard k-ω model gave good agreement with experimental results, but a low-Reynolds number (LRN) k-ω model improved the results. They also emphasized the importance of accurate inlet conditions to obtain good results.

The studies all agree that CFD analysis of the human upper airways is a great tool for giving a realistic representation of flow related problems. Choosing a specific turbulence model can be challenging, because it depends, among other things, on the geometry and Reynolds number. The literature suggests that standard turbulence models are not always accurate enough, but improved models that take into consideration effects such as recirculation and separation, can provide results that agree well with empirical data. However, to our knowledge, no systematic studies have been published to compare and assess various turbulence models in the human upper airways (Quadrio et al., 2014).

The human upper airways consist of complex meatuses of highly varying cross-sections with hydraulic diameters ranging from milli- to centimeter-scale. Additionally, the sinusoidal nature of the intrathoracic pressure, due to the inhalation/expiration cycle, results in a wide range of flow velocities, hence Reynolds numbers. Most likely, the airflow is transitional, due to the relatively low maximum Reynolds number and the limited time to develop the turbulent boundary layers.

The current paper focuses on investigating the qualitative and quantitative differences between standard turbulence models applied to a patient-specific, rigid-wall geometry of the upper airways, investigated by Aasgrav (2016) based on CT images (Jordal, 2016). The study includes a sensitivity study with respect to grid size as well as turbulence boundary conditions. The present work is a part of the collaboration project "Modelling of obstructive sleep apnea by fluid-structure interaction in the upper airways" aiming to demonstrate the applicability of CFD as a clinical tool in OSAS diagnostics and treatment (OSAS, 2016). The project is a collaboration between NTNU, SINTEF and St. Olavs Hospital, the university hospital in Trondheim, and is funded by the Research Council of Norway.

MODEL DESCRIPTION

Computational Geometry and Mesh of the Human Upper Airways

The geometry retrieval is based on pre-operative CT scans of "Patient 12" (Moxness, 2014), provided by the Department of Radiology and Nuclear Medicine at St. Olavs Hospital, the university hospital in Trondheim. A detailed description of the process of retrieving the geometry can be found in the M.Sc. thesis by Jordal (2016). The resulting 3D geometry was modified to get an even distribution of outflow. The final pre-operational geometry used for further investigations is shown in Figure 1. The geometry has two inlets (left and right nostrils) and one outlet (trachea). The oral cavity was not considered in the model, and neither were the paranasal sinuses.
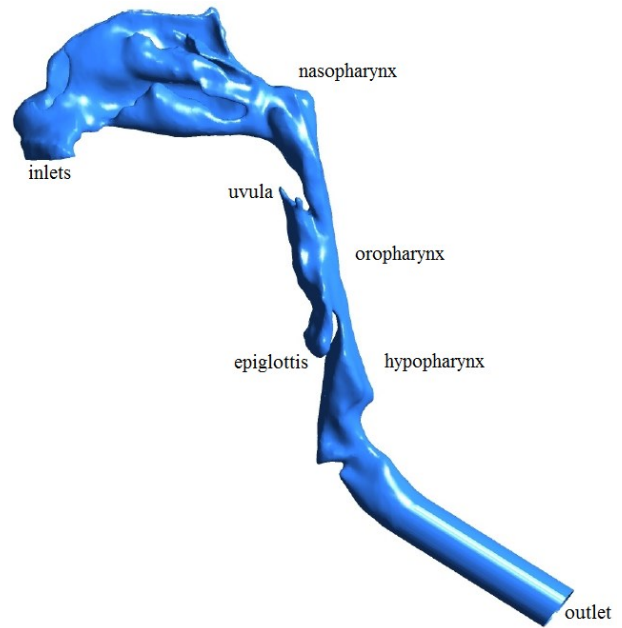
Figure 1: Final pre-operative model used in simulations, seen from the left (Jordal, 2016)
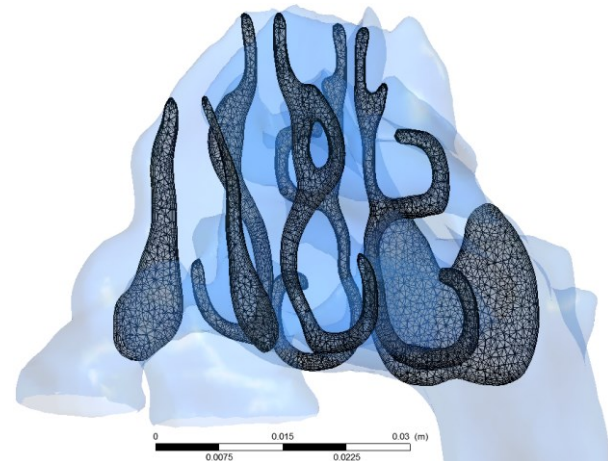
Figure 2: Base-case computational mesh in the nasal cavity, displayed on the cut-planes 1-4 (see Figure 4)

The meshing was done in ANSYS Meshing (Ansys, 2017), version 16.2. In order to get good results for the near-wall effects, an inflation layer consisting of five layers was utilized at the wall. The option "Size Function" in ANSYS Meshing was set to "Proximity and Curvature", where proximity captures the effects of tight gaps and thin sections, like for instance in the nasal cavity, and curvature captures sharp changes in flow direction, like we have in the nasopharynx. For the base-case, the size limitation was set to 1 mm. This resulted in a mesh with ca. 1.4 million grid cells. Details of the grid can be seen in figures 2 and 3. The grid sensitivity was investigated by comparing the base-case mesh to a refined mesh consisting of 6.8 million grid cells (size limitation of 0.8mm) and a coarser mesh consisting of 0.81 million grid cells (size limitation of 2.0mm), using the realizable k-ε turbulence model (see next section).
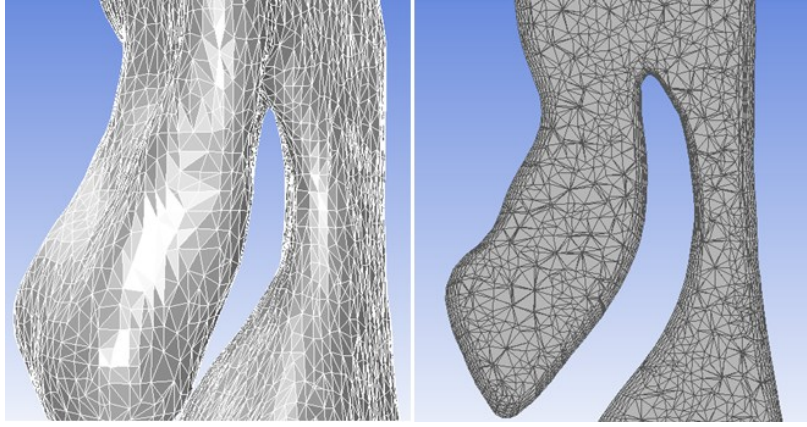
Figure 3: Details of the base-case mesh at the epiglottis; on the wall and in an arbitrary cut-plane

Mathematical Models for Turbulent Flow in the Human Upper Airways

The Navier-Stokes equations describe fluid flow and thus are the foundation for the mathematical modelling of the airflow in the human upper airways. Due to the low Mach number (Ma<<0.3), the flow is considered incompressible, and the governing equations take the following form (Pope, 2000):

Continuity equation
$$\nabla \cdot \boldsymbol{U} = 0 \tag{1}$$

Momentum equation
$$\frac{D\boldsymbol{U}}{Dt} = -\frac{1}{\rho}\nabla p + \nu\nabla^2\boldsymbol{U} \tag{2}$$

Here, $\boldsymbol{U}$ is the velocity vector, p is the pressure, ρ is the mass density and ν is the kinematic viscosity.

Even though we have a relatively low maximum Reynolds number of about 2000, we include effects of turbulence. Several solution approaches exist, with Reynolds-averaged Navier-Stokes (RANS) modelling being the most utilized one. Other popular methods are Large Eddy Simulation (LES) and Direct Numerical Simulation (DNS). DNS is solving the Navier-Stokes equations numerically for all significant spatial and temporal scales and does not involve any additional modelling of turbulence. LES involves explicit representation of the large-scale turbulent eddies containing anisotropic energy, while the smaller-scale, more isotropic turbulent motions are modelled. Although LES has a significantly lower computational cost than DNS, the RANS approach is far less computationally demanding. This makes RANS the desired approach in most practical cases. Here, we consider the RANS equations, where the Reynolds stress tensor is determined by the Boussinesq approximation.

RANS equations
$$\frac{\partial U_i}{\partial x_i} = 0 \tag{3}$$

$$\frac{\partial U_i}{\partial t} + U_j\frac{\partial U_i}{\partial x_j} = -\frac{\partial p}{\rho\partial x_i} + \nu\frac{\partial^2 U_i}{\partial x_j\partial x_j} - \frac{\partial \overline{u_i'u_j'}}{\partial x_j} \tag{4}$$

Boussinesq approximation
$$-\overline{u_i'u_j'} = 2\nu_T S_{ij} - \frac{2}{3}k\delta_{ij} \tag{5}$$

Mean strain-rate tensor
$$S_{ij} = \frac{1}{2}\left(\frac{\partial U_i}{\partial x_j} + \frac{\partial U_j}{\partial x_i}\right) \tag{6}$$

Here, U_i and U_j are the mean velocity components in the i and j directions, respectively ($i, j \in \{x, y, z\}$), p is the mean pressure, k is the turbulence kinetic energy, ν_T is the eddy viscosity to be defined by the RANS model, δ_{ij} is the Kronecker delta, and the Einstein summation convention is employed. The Reynolds stress models are generally divided into categories based on how many equations need to be solved, with the two-equation models being the most used and the most verified RANS types.

Numerical Approximation

The governing equations were solved using the commercial CFD software ANSYS Fluent 16.2 (Ansys, 2017). In the following, simulation results from the upper airways geometry shown in the previous section are shown, for various standard RANS turbulence models as well as laminar flow. Coupled solver was employed for the pressure-velocity coupling. For pressure and momentum, second order upwind solvers were chosen, while for the turbulent kinetic energy and turbulent dissipation rate, a first order upwind solver was determined to be accurate enough. Standard material properties for air was employed (mass density of 1.225 kg/m^3 and viscosity of 1.7894·10^{-5} Pa s).

Boundary conditions were:
- Atmospheric total pressure at the inlets (nostrils)
- Velocity outlet corresponding to an inspiratory volumetric flow rate of 250 ml/s
- No-slip condition at the walls
- Turbulence intensity of 5%
- Turbulent viscosity ratio of 10

The sensitivity to turbulence boundary conditions at the inlets were investigated by testing the sensitivity to reducing the turbulence intensity at the inlets to 1% and increasing it to 10%.

RESULTS

The described setup was simulated with four different turbulence models, namely the standard k-ε and k-ω models, as well as realizable k-ε and k-ω SST. The four models were checked against laminar flow by comparing the area-averaged pressure at selected cross-sections throughout the geometry (see Figure 4). The results are shown in Figure 5. The models showed only minor differences in results upstream of the epiglottis. Some differences are observed downstream of the epiglottis, but it is believed that the effects so far down do not affect the flow further up where the airway collapses in OSAS.

It is to be expected that the difference between a laminar model and various turbulence models is minor, because the maximum Reynolds number in the flow is about 2000, indicating that the flow is mainly laminar. Because of the complex geometry inducing separated flow, the flow most likely has some turbulence features as well. The total pressure, $p_{tot} = p_{stat} + 0.5\rho U^2$, decreases throughout the geometry as it should, while the static pressure depicted in Figure 5 does not show this behavior for all the models because of the highly varying velocity.

Both of the k-ε models' residuals converged to an acceptable value, where the residuals for continuity, k, ε, and x-, y- and z-velocities started at about 1, and converged to values between 10^{-4} and 10^{-8}, with a steady state solver. None of the k-ω models' residuals converged as desired with steady state. Thus, a transient simulation was needed to achieve residuals in the range of 10^{-4}-10^{-8}. Despite the steady-state boundary conditions, the solution might be transient due to unsteady vortices in regions with separated flow. In this case, a converged steady-state solution would be unfeasible.

The realizable k-ε model was chosen for the grid and turbulence boundary condition sensitivity studies. First, a sensitivity study was conducted to investigate the sensitivity to turbulent intensity at the inlets, as described in the Model Description chapter. In Figure 6, it is seen that the turbulent kinetic energy differences that exist close to the inlets, due to the different turbulence intensity boundary conditions, decay as the air progresses through the nasal cavity, such that the effect of changing the inlet boundary condition is negligible when considering the flow entering the nasopharynx. Furthermore, we found that the velocity streamlines and velocity magnitude are largely unaffected by the turbulence intensity. Second, a grid sensitivity study as described in the previous chapter was performed utilizing a base-case grid (1.4M grid cells), a refined grid (6.8M grid cells) and a coarser grid (0.81M grid cells). Figure 7 shows a comparison of the area-averaged pressure at the selected cross-sections for the different grids. It is evident that the coarsest mesh differs from the base case and the finer mesh, leading to the conclusion that grid independency is achieved for the base case sizing and finer resolutions. The velocity streamlines in Figure 8 show that the three different meshes give some differences in the flow patterns. This is especially prominent right after the epiglottis and in the oropharynx behind the oral cavity. Here, the refined mesh portrays more swirl in the flow, indicating higher vorticity in these regions, a characteristic of the flow pattern that could be an important factor in the understanding of OSAS. The coarser mesh has less swirl than the two other meshes, indicating that the mesh is too coarse to capture the complexity and turbulence effects of the flow. The wall pressure was found not to show any difference between the three meshes. The turbulence kinetic energy plot was similar for the two finer meshes, while it differed greatly for the coarser mesh, giving the same conclusion that the coarser mesh does not have a large enough resolution to capture the turbulence effects.

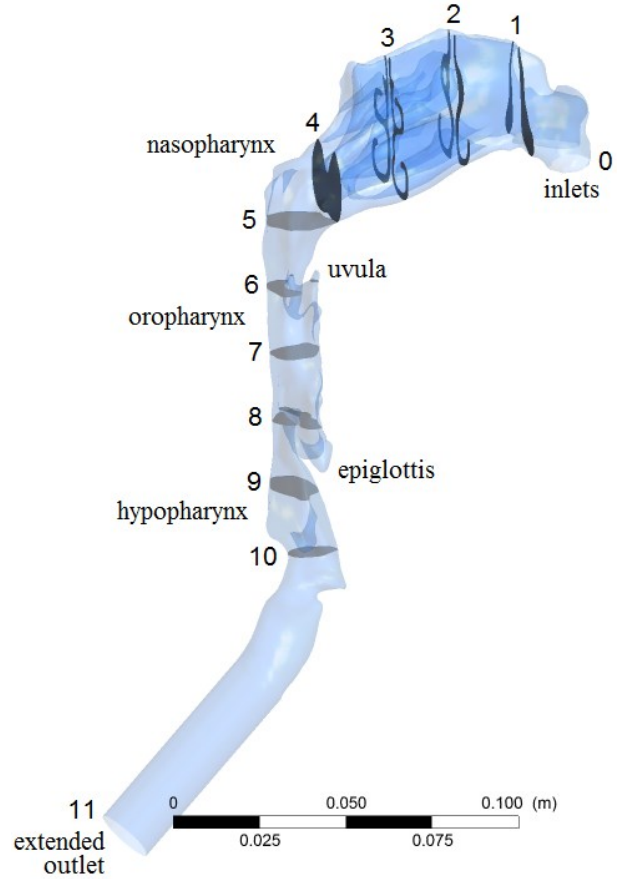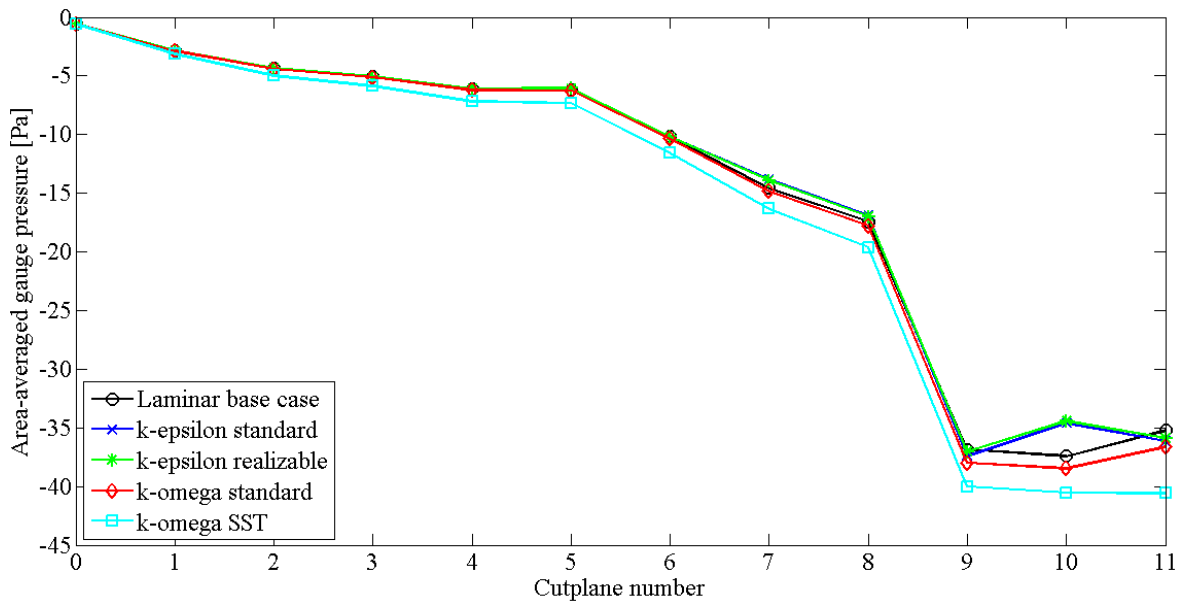**Figure 4:** Location and numbering of cross-sections in the final pre-op geometry

Figure 5: Comparison of area-averaged pressure for the laminar base-case and four different turbulence models
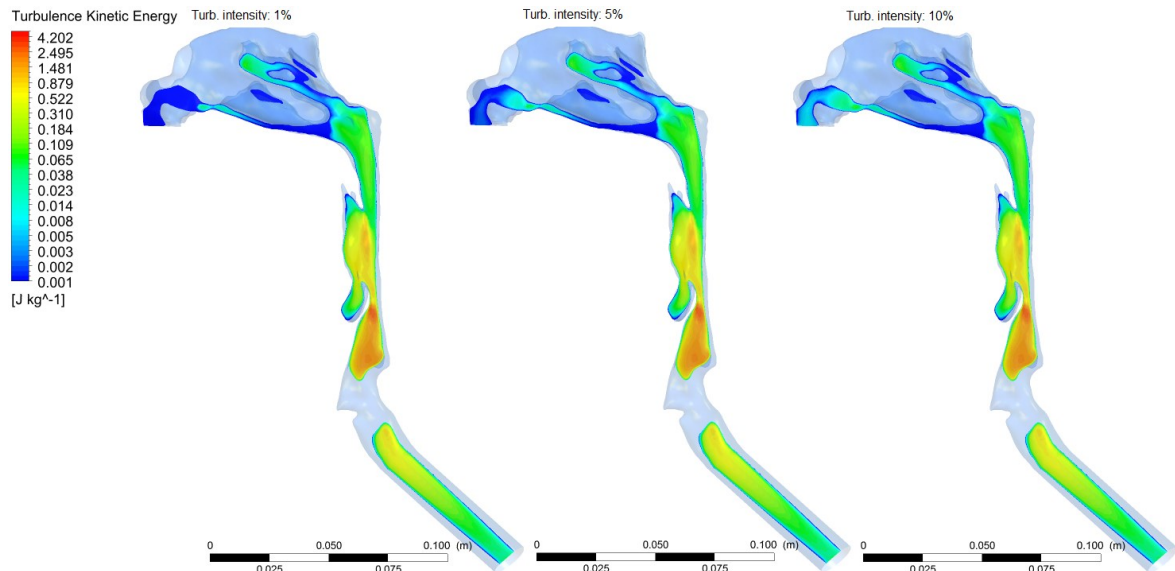

Figure 6: Turbulence kinetic energy for different turbulent intensities using the base case mesh, logarithmic scale
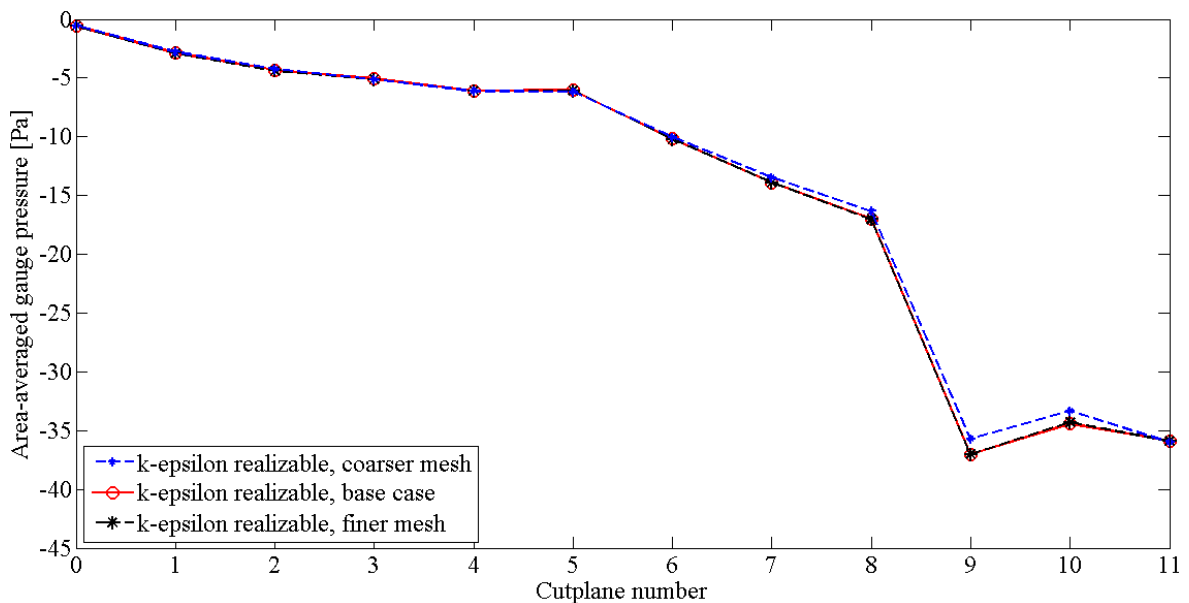

Figure 7: Comparison of area-averaged pressure for the turbulent base-case, and a finer and coarser mesh
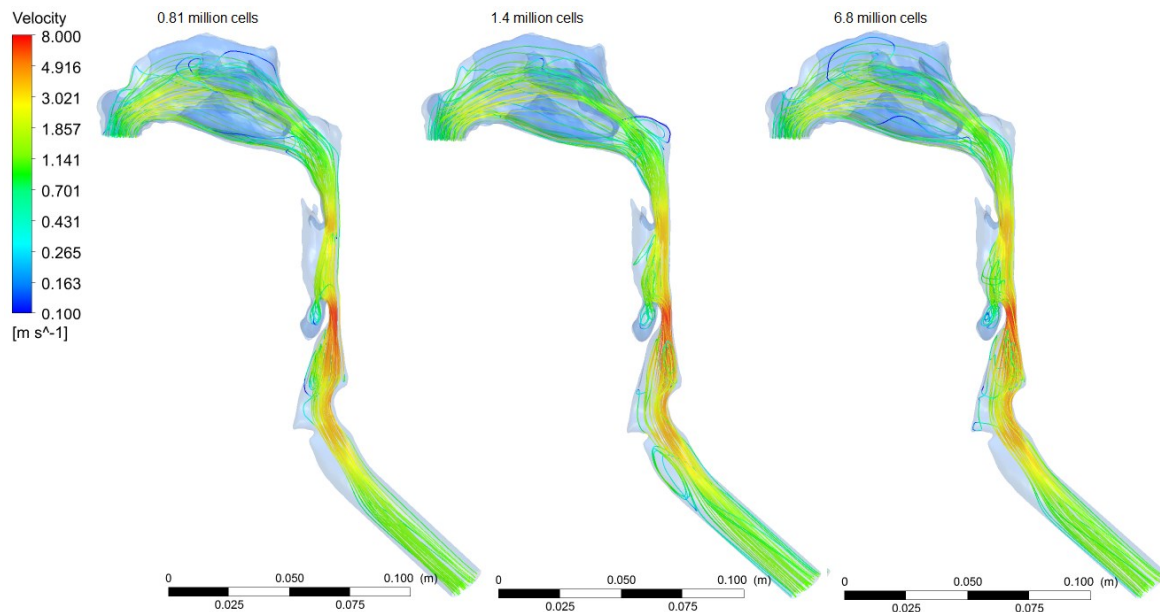
Figure 8: Velocity streamlines for different meshes, logarithmic scale

CONCLUSIONS

CFD simulations of airflow in the human upper airways were performed to investigate and assess the importance of turbulence modelling. Four different standard RANS turbulence models were compared to a laminar flow model at a constant inspiratory volumetric flow rate of 250 ml/s in a model geometry based on pre-operative CT images of an OSAS patient. The area-averaged pressure at selected cross-sections upstream of the epiglottis were largely unaffected by the choice of laminar or turbulent flow models. Thus, the main conclusion of the study is that effects of turbulence are insignificant in CFD modelling of the airflow in the pre-operative model of the upper airways of the chosen patient. It remains to investigate other volumetric flow rates.

Employing the realizable k-ε model, the effect of varying turbulence inlet boundary conditions was investigated by varying the turbulent intensity at the inlets from 1% to 10%. No significant effect was observed downstream of the nasal cavities.

Finally, a grid sensitivity study was conducted to assess the grid independency of the computed results. The base-case mesh, based on a cell size limitation of 1 mm and consisting of 1.4 million cells, showed some discrepancy in the flow pattern in some regions, but produced almost exactly the same pressure loss results as a refined mesh consisting of 6.8 million cells (size limitation of 0.8 mm). A coarser mesh consisting of 0.81 million cells was not able to reproduce the results and thus did not have the required resolution to capture the turbulence effects.

REFERENCES

AASGRAV, E., (2016), "CFD simulations of turbulent flow in the upper airways", NTNU, M.Sc. specialization project.

ANSYS (2017), http://www.ansys.com.

JOHNSEN, S.G., (2016), Private communication.

JORDAL, M. R., (2016), "Patient Specific Numerical Simulation of Flow in the Human Upper Airways", NTNU, M.Sc. thesis.

LONGEST, P.W., and VINCHURKAR, S., (2007), "Validating CFD predictions of respiratory aerosol deposition: Effects of upstream transition and turbulence", *Journal of Biomechanics*, **40**, 305-316.

MA, B., and LUTCHEN, K.R., (2009) "CFD simulation of aerosol deposition in an anatomically based human large-medium airway model", *Annals of Biomedical Engineering*, **37**, 271-285.

MIHAESCUA, M., MURUGAPPANB, S., KALRAC, M., S. KHOSLAB, S., and GUTMARK, E., (2008), "Large Eddy Simulation and Reynolds-Averaged Navier–Stokes modeling of flow in a realistic pharyngeal airway model: An investigation of obstructive sleep apnea", *Journal of Biomechanics*, **41**, 2279–2288.

MOXNESS, M.H. and NORDGÅRD, S., (2014), "An observational cohort study of the effects of septoplasty with or without inferior turbinate reduction in patients with obstructive sleep apnea," *BMC Ear, Nose and Throat Disorders*, **14**.

OSAS, (2016), "Modeling of Obstructive Sleep Apnea by Fluid-Structure Interaction in the Upper Airways", http://www.osas.no.

POPE, S.B., (2000). *Turbulent Flows*. Cambridge University Press.

QUADRIO, M., PIPOLO, C., CORTI, S., LENZI, R., MESSINA, F., PESCI, C., and FELISATI, G., (2014), "Review of computational fluid dynamics in the assessment of nasal air flow and analysis of its limitations", *Eur Arch Otorhinolaryngol*, **271**, 2349-2354.

RIAZUDDIN, V.N., ZUBAIR, M., ABDULLAH, M.Z., RUSHDAN, I., SHUAIB, I.L., HAMID, S.A., and AHMAD, K.A., (2011), "Numerical study of inspiratory and expiratory flow in a human nasal cavity", *Journal of Medical and Biological Engineering*, **31**, 201-206.

STAPLETON, K.W., GUENTSCH, E., HOSKINSON, M.K., and FINLAY, W.H., (2000), "On the suitability of k-ε modeling for aerosol deposition in the mouth and throat: A comparison with experiment", *Journal of Aerosol Science*, **31**, 739-749.

NTNU		Prepared by	Number	Date
		HSE section	HMSRV2601E	09.01.2013
HSE		Approved by	Replaces	
		The Rector		01.12.2006

Hazardous activity identification process

Unit: Department of Energy and Process Engineering (EPT)

Line manager:

Participants in the identification process (including their function):

Short description of the main activity/main process: Master project for student Elin Aasgrav.

Project title: Investigation of CFD simulations of flow in the upper airways

Date: 06.06.17

Is the project work purely theoretical? (YES/NO): YES   *Answer "YES" implies that supervisor is assured that no activities requiring risk assessment are involved in the work. If YES, briefly describe the activities below. The risk assessment form need not be filled out.*

Signatures: *Responsible supervisor:* _Bernd Müller_   *Student:* _Elin Aasgrav_

ID nr.	Activity/process	Responsible person	Existing documentation	Existing safety measures	Laws, regulations etc.	Comment
	Writing and CFD simulations on computer					

NTNU	Risk assessment	Prepared by	Number	Date	
		HSE section	HMSRV2603E	04.02.2011	
		Approved by		Replaces	
HSE/KS		The Rector		01.12.2006	

Unit: *(Department)*   **Date:**

Line manager:

Participants in the identification process (including their function)**:**

Short description of the main activity/main process: Master project for student xx. Project title.

Signatures: *Responsible supervisor:*   *Student:*

Activity from the identification process form	Potential undesirable incident/strain	Likelihood:	Consequence:			Risk Value (human)	Comments/status Suggested measures
		Likelihood (1-5)	Human (A-E)	Environment (A-E)	Economy/ material (A-E)		

Likelihood, e.g.:
1. *Minimal*
2. *Low*
3. *Medium*
4. *High*
5. *Very high*

Consequence, e.g.:
A. *Safe*
B. *Relatively safe*
C. *Dangerous*
D. *Critical*
E. *Very critical*

Risk value (each one to be estimated separately):
Human = Likelihood x Human Consequence
Environmental = Likelihood x Environmental consequence
Financial/material = Likelihood x Consequence for Economy/materiel

NTNU		Risk assessment	Prepared by	Number	Date	
			HSE section	HMSRV2603E	04.02.2011	
			Approved by		Replaces	
HSE/KS			The Rector		01.12.2006	

Potential undesirable incident/strain

Identify possible incidents and conditions that may lead to situations that pose a hazard to people, the environment and any materiel/equipment involved.

Criteria for the assessment of likelihood and consequence in relation to fieldwork

Each activity is assessed according to a worst-case scenario. Likelihood and consequence are to be assessed separately for each potential undesirable incident. Before starting on the quantification, the participants should agree what they understand by the assessment criteria:

Likelihood

Minimal 1	Low 2	Medium 3	High 4	Very high 5
Once every 50 years or less	Once every 10 years or less	Once a year or less	Once a month or less	Once a week

Consequence

Grading	Human	Environment	Financial/material
E Very critical	May produce fatality/ies	Very prolonged, non-reversible damage	Shutdown of work >1 year.
D Critical	Permanent injury, may produce serious serious health damage/sickness	Prolonged damage. Long recovery time.	Shutdown of work 0.5-1 year.
C Dangerous	Serious personal injury	Minor damage. Long recovery time	Shutdown of work < 1 month
B Relatively safe	Injury that requires medical treatment	Minor damage. Short recovery time	Shutdown of work < 1week
A Safe	Injury that requires first aid	Insignificant damage. Short recovery time	Shutdown of work < 1day

The unit makes its own decision as to whether opting to fill in or not consequences for economy/materiel, for example if the unit is going to use particularly valuable equipment. It is up to the individual unit to choose the assessment criteria for this column.

Risk = Likelihood x Consequence

Please calculate the risk value for "Human", "Environment" and, if chosen, "Economy/materiel", separately.

About the column "Comments/status, suggested preventative and corrective measures":

Measures can impact on both likelihood and consequences. Prioritise measures that can prevent the incident from occurring; in other words, likelihood-reducing measures are to be prioritised above greater emergency preparedness, i.e. consequence-reducing measures.

NTNU		Risk matrix	prepared by	Number	Date	
			HSE Section	HMSRV2604	8 March 2010	
			approved by	Page	Replaces	
HSE/KS			Rector	4 of 4	9 February 2010	

MATRIX FOR RISK ASSESSMENTS at NTNU

CONSEQUENCE	Extremely serious	E1	E2	E3	E4	E5
	Serious	D1	D2	D3	D4	D5
	Moderate	C1	C2	C3	C4	C5
	Minor	B1	B2	B3	B4	B5
	Not significant	A1	A2	A3	A4	A5
		Very low	Low	Medium	High	Very high
		LIKELIHOOD				

Principle for acceptance criteria. Explanation of the colours used in the risk matrix.

Colour		Description
Red		Unacceptable risk. Measures must be taken to reduce the risk.
Yellow		Assessment range. Measures must be considered.
Green		Acceptable risk Measures can be considered based on other considerations.